TÉCNICO LISBOA

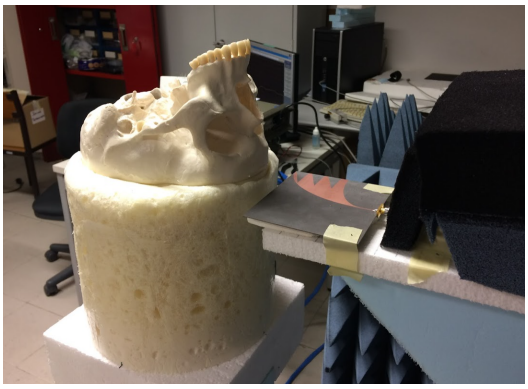

Antennas Design and Image Reconstruction for Microwave Imaging Systems

André Filipe Lourenço Martins

Thesis to obtain the Master of Science Degree in

Electrical and Computer Engineering

Supervisor(s): Prof. António Manuel Restani Graça Alves Moreira
Prof. Carlos António Cardoso Fernandes

Examination Committee

Chairperson: Prof. José Eduardo Charters Ribeiro da Cunha Sanguino
Supervisor: Prof. António Manuel Restani Graça Alves Moreira
Member of the Committee: Prof. Paulo Sérgio de Brito André

April 2018

To those who were always by my side.

Declaration:

I declare that this document is an original work of my own authorship and that it fulfills all the requirements of the Code of Conduct and Good Practices of the Universidade de Lisboa.

Acknowledgments

First of all, I would like to express my gratitude to Prof. António Topa, who inspired me in times of need and guided me through the Telecommunications area with his remarkable teaching skills. His kind words, friendliness and empathy were outstanding and will always remain with me.

Secondly, I would like to thank Mr. Carlos Brito and Mr. António Almeida for providing the technical expertise throughout this Thesis. Mr. Carlos Brito with his sympathy and great knowledge on antenna fabrication processes, who taught me in new fields I've never been in contact with and for making the "Palm Tree Vivaldi" atntenna a reality and as perfect as humanly possible. And Mr. António Almeida for all his patience and help in creating all the needed impeccable measurement set-ups.

I would also like to thank the host institution, *Instituto de Telecomunicações* (IT), Lisbon, for being my second home for the past year of hard work. Without IT providing its facilities, equipments and, most importantly, its people immense knowledge, this Thesis wouldn't be feasible.

I also must express my sincere gratitude to João Felício who was definitely one of my Supervisors throughout this work. Not only he provided outstanding words of advice, but also pushed me forward by exposing me to new concepts, new ideas and solutions to most of the problems I've faced during these months. And, above all, for all the friendliness and time spent talking with me, about anything that came to our minds.

To Prof. Carlos Fernandes and Prof. António Moreira. For all the friendly relation that we developed, for all the laughs, for all the meetings in which incentive words given, for all the scientific expertise and knowledge that was given to me, for challenging me constantly with this Master Thesis and for leading the way throughout these months. I will always be grateful to both of you.

To all my dear friends whom I've spent these wonderful years at Instituto Superior Técnico with. All those who were there for me in those hard days and nights of study, having fun in Lisbon or simply going around without destination. I can't express by words how you all mean the world to me and I'm certain that these friendships will remain strong until the end of days.

To Anaísa, my dear girlfriend. I can't thank you enough for all the hours spent by my side, cheering for me, for all the love and support, giving everything humanly possible to make these months of work definitely better. Your constant presence, your lovely smile and kind words will always be in my heart. This Master Thesis is also yours!

Finally, I would like to thank my caring parents and grandparents. Even with the distance and by spending so much time far away from them, their kind words of wisdom and support came to me everyday. You made this journey possible, you made it a unique experience, you made me who I am, and I can't ever thank you enough for all the sacrifices made in order for me to pursue this goal of my life. My most sincere words of gratitute for you!

Resumo

Esta Dissertação apresenta os passos para projectar uma antena ”Palm Tree Vivaldi” (PTVA ao longo do texto) útil para Sistemas de Imagiologia por Microondas e propõe um Algoritmo de Reconstrução de Imagem com técnicas de calibração, baseadas no algoritmo Delay and Sum (DAS), que tem por objectivo detectar hemorragias intracranianas.

A PTVA prototipada é uma estrutura pequena, compacta e fina ($110 \times 95 \times 0.83$ [mm^3]), oferecendo características Ultra Wideband (UWB) na banda de frequências de 1.61-3.02 GHz, diagrama de radição directivo e pequena distorção de impulso. A PTVA apresenta ressonadores de ranhura nos elementos radiantes, que são uma inovação com o objectivo de miniaturizar as antenas Vivaldi ao confinar o campo eléctrico, criando assim um aumento das correntes superficiais nos ressonadores, levando a um aumento do comprimento eléctrico da antena.

Uma descrição do algoritmo DAS é apresentada e ilustra as capacidades de reconstrução de imagem do DAS no ar. Implementado o algoritmo DAS, uma extensão do mesmo para um cenário mais complexo foi realizada, propondo técnicas de calibração, a implementação do Princípio de Fermat e de uma janela de integração para um modelo de uma cabeça humana com uma hemorragia.

Esta Dissertação é concluída através da realização de medidas com a PTVA prototipada e aplicando o DAS implementado com o objectivo de detectar uma anomalia de água, simulando uma hemorragia, no interior de um phantom de uma cabeça humana, com permitividade próxima daquela encontrada no cérebro humano.

Palavras-chave: Antena Vivaldi, Algoritmo Delay and Sum, Reconstrução de Imagem, Desenho de Antenas, Sistemas de Imagiologia por Microondas

Abstract

This Thesis presents the design steps of a ”Palm Tree Vivaldi” antenna (onwards PTVA) suitable for Microwave Imaging Systems and proposes an Image Reconstruction Algorithm with calibration techniques, based on the Delay and Sum (DAS) algorithm, which aims at detecting intracranial haemorrhages.
The prototyped PTVA is a small, compact and thin stucture ($110\times95\times0.83$ [mm^3]), offering Ultra Wideband (UWB) characteristics in the 1.61-3.02 GHz frequency band, directive radiation pattern and small reflected pulse distortion. The PTVA features edge slot resonators on its radiators, which are a novel feature used to miniaturize Vivaldi antennas dimensions by confining the electric field, thus creating an increase of the surface current distributions in the resonators, leading to an increased electric length of the antenna.
A description of the DAS algorithm is presented and it illustrates the DAS image reconstruction capabilities in the air. By implementing the DAS algorithm, its extention to a more complex scenario is performed, by proposing calibration techniques, the implementation of Fermat's Principle and an integration window for a human head model with an haemorrhage.
The Thesis is concluded by performing measurements with the prototyped PTVA and applying the implemented DAS algorithm aiming at detecting a water anomaly, emulating an haemorrhage, inside a human head phantom, with permittivity close to the one found in the human brain.

Palavras-chave: Vivaldi antenna, Delay and Sum Algorithm, Image Reconstruction, Antenna Design, Microwave Imaging Systems

Contents

List of Figures . . . .
List of Tables v
List of Acronyms vii

1 Introduction **1**
1.1 Introduction 1
1.2 Motivation 2
1.3 Objectives 2
1.4 Master Thesis Structure 2

2 State of the Art **5**
2.1 Antennas Design 5
2.2 Phantoms 7
2.3 Image Reconstruction Algorithms 7

3 Palm Tree Vivaldi Antenna Design **9**
3.1 Palm Tree Vivaldi Antenna Design Steps 9
3.1.1 Vivaldi Antenna Base Model 9
3.1.2 Palm Tree Vivaldi Antenna Model 17
3.2 Palm Tree Vivaldi Antenna Prototype and Testing 26

4 Image Reconstruction Algorithm **31**
4.1 Image Reconstruction Algorithm Development 31
4.1.1 Delay and Sum Algorithm 31
4.1.2 Delay and Sum Simulations in the Air 35
4.1.3 Delay and Sum Simulations with a Human Head Model 40
4.2 Image Reconstruction using a Human Head Phantom 53
4.2.1 Human Head Phantom and Measurement Set-Up 53
4.2.2 Image Reconstruction Algorithm Results 56

5 Conclusions and Future Work **61**
5.1 Conclusions 61
5.2 Future Work 62

Bibliography **65**

A Palm Tree Vivaldi Antenna Masks **69**

B Human Head Skull Model Permittivity Measurement **71**

C Human Head Liquid Phantom Permittivity Measurement **75**

List of Figures

3.1 Vivaldi antenna designed and prototyped in [14]. 9
3.2 Vivaldi antenna front and back curvatures. 11
3.3 Vivaldi antenna shifted front curvature and back curvature. 12
3.4 Vivaldi antenna front radiator. 12
3.5 Vivaldi antenna back radiator. 12
3.6 Vivaldi antenna front microstrip line and SMA connector view. 13
3.7 Vivaldi antenna back microstrip line, ground plane and SMA connector view. 13
3.8 Designed Vivaldi antenna. 14
3.9 Designed Vivaldi antenna S_{11} parameter. 14
3.10 Designed Vivaldi antenna far field radiation pattern. 15
3.11 LTIS in the time domain. 16
3.12 LTIS in the frequency domain. 16
3.13 Simulation setup for pulse distortion assessment. 16
3.14 Synthesized emitted pulse (red) and reflected received pulse (dotted blue). 17
3.15 Designed Palm Tree Vivaldi antenna resonators. 18
3.16 Modified Palm Tree Vivaldi antenna ground plane. 19
3.17 Designed Palm Tree Vivaldi antenna S_{11} parameter comparison with Base Vivaldi antenna model. 20
3.18 Designed Palm Tree Vivaldi antenna far field radiation pattern. 20
3.19 Synthesized emitted pulse (red) and reflected received pulse (dotted blue). 21
3.20 Palm Tree Vivaldi antenna front microstrip line and SMA connector view. 22
3.21 Palm Tree Vivaldi antenna front microstrip line, ground plane and SMA connector view. . . 22
3.22 Palm Tree Vivaldi antenna front radiator shape. 22
3.23 Palm Tree Vivaldi antenna back radiator shape. 22
3.24 Designed Palm Tree Vivaldi antenna. 23
3.25 Designed Palm Tree Vivaldi antenna S_{11}. 23
3.26 Designed Palm Tree Vivaldi antenna far field radiation pattern. 24
3.27 Designed Palm Tree Vivaldi antenna near electric field magnitude in the yz plane. 24
3.28 Designed Palm Tree Vivaldi antenna near electric field magnitude in the xy plane. 25
3.29 Designed Palm Tree Vivaldi antenna surface currents distribution magnitude. 25
3.30 Synthesized emitted pulse (red) and reflected received pulse (dotted blue). 26

3.31 Produced Palm Tree Vivaldi antenna front view. 27
3.32 Produced Palm Tree Vivaldi antenna back view. 27
3.33 Produced and simulated Palm Tree Vivaldi antennas' S_{11}. 27
3.34 S_{11} parameter measurement set-up with a copper plane. 28
3.35 Synthesized emitted pulse (red), reflected simulated received pulse (dotted cyan) and reflected measured received pulse (dotted blue). 29

4.1 Monostatic radar approach for the DAS algorithm. 32
4.2 Palm Tree Vivaldi antenna peak occurence time. 33
4.3 DAS detection illustration for 1 antenna. 33
4.4 Proposed circular Palm Tree Vivaldi antennas scanning array. 34
4.5 DAS detection illustration for 8 antennas. 34
4.6 CST Studio Suite simulation model. 35
4.7 Scanning grid, as seen in Matlab. 36
4.8 Reflected signals for each antenna position. 36
4.9 DAS detection as seen in Matlab, for the antenna in position 1. 37
4.10 DAS detection as seen in Matlab, for the antenna in position 5. 38
4.11 DAS image reconstruction for a copper target, in the air. 39
4.12 DAS image reconstruction for a copper target, in the air, with squared values of the amplitudes. 39
4.13 Human Head propagation model. 40
4.14 Simulation set-up, as seen in CST Studio Suite, with Human Head model and water anomaly. 41
4.15 Scanning grid, as seen in Matlab. 42
4.16 Reflected signals for each antenna. 42
4.17 Symmetries in the human skull, as seen in a real scale model. 43
4.18 Water anomaly reflected signal, received at the antenna in position 6. 44
4.19 Water anomaly reflected signal, received at the antenna in position 2. 45
4.20 Water anomaly modified reflected signal, received at the antenna in position 2. 45
4.21 Delimiting curve of the bone/brain dielectric boundary. 46
4.22 Human head propagation model, considering the Fermat's Principle. 48
4.23 Scanning grid, delimiting curve of bone/brain dielectric boundary and Fermat's Principle, as seen in Matlab. 48
4.24 DAS image reconstruction for a water anomaly, inside a human head model. 49
4.25 DAS image reconstruction for a water anomaly, inside a human head model, with squared values of the amplitudes. 49
4.26 DAS image reconstruction for a water anomaly, inside a human head model, applying the integration window. 50
4.27 DAS image reconstruction for a water anomaly, inside a human head model, applying the integration window, with squared values of the amplitude. 51

4.28 Simulation set-up, as seen in CST Studio Suite, with Human Head model and tilted water anomaly. . . . 51
4.29 DAS image reconstruction for a tilted water anomaly, inside a human head model. . . . 52
4.30 DAS image reconstruction for a tilted water anomaly, inside a human head model, with squared values of the amplitude. . . . 53
4.31 Real size human skull model. . . . 54
4.32 Plastic tube filled with tap water and holding structure. . . . 54
4.33 Position of the anomaly inside the open human head skull model. . . . 55
4.34 Reference line, position of the antenna 1.7 cm below it and maximum liquid phantom level. 55
4.35 Fabricated measurement set-up, with the PTVA and the human head phantom. . . . 56
4.36 Reflected signals for each antenna position. . . . 57
4.37 Delimiting curve of the air/bone dielectric boundary. . . . 57
4.38 DAS image reconstruction for the human head phantom, with faulty calibration. . . . 58
4.39 Antenna in position 6, with faulty calibration. . . . 58
4.40 Antenna in position 4, with correct haemorrhage detection. . . . 59
4.41 DAS image reconstruction for the human head phantom, using an alternative calibration method. . . . 59

A.1 Palm Tree Vivaldi antenna front layer mask. . . . 69
A.2 Palm Tree Vivaldi antenna back layer mask. . . . 70

B.1 Real size human skull model, made of PUR. . . . 71
B.2 Transmission set-up for permittivity measurement. . . . 72
B.3 PUR permittivity measurement, using two dipoles in transmission mode. . . . 73
B.4 Phase delay for skull model thickness of 4.94 mm. . . . 73
B.5 Phase delay for skull model thickness of 6.56 mm. . . . 74
B.6 Phase delay for skull model thickness of 5.20 mm. . . . 74

C.1 Resonating cavity setup in transmission mode. . . . 75
C.2 Resonating cavity simulation model, as seen in CST Studio Suite. . . . 76
C.3 Best-fit model for the S_{12} parameter unwrapped phase. . . . 77
C.4 Best-fit model for the S_{12} parameter magitude. . . . 77
C.5 Best-fit model for the S_{11} parameter unwrapped phase. . . . 78
C.6 Best-fit model for the S_{11} parameter magitude. . . . 78
C.7 Simulated permittivity for the designed Cole-Cole material. . . . 78

List of Tables

3.1 Vivaldi Antenna Parameters 10
3.2 Current path effect on lower frequency of operation 19
3.3 Palm Tree Vivaldi antenna parameters 21
3.4 Rogers RT/duroid 5880 substrate datasheet parameters 26

4.1 Image Reconstruction Algorithm without and with integration window running time 51

C.1 Cole-Cole Material parameters defined in CST Studio Suite. 76

List of Acronyms

CAD Computer-Aided Design

DAS Delay And Sum

DGBE Di-etyhlene Glycol Buthyl Ether

DMAS Delay Multiply And Sum

E-PUR Expanded Polyurethane

FCC Federal Communications Commission

ITU-R International Telecommunication Union - Radiocommunication

LTIS Linear and Time Invariant System

MRI Magnetic Ressonance Imaging

PET Positron Emission Tomography

PTVA Palm Tree Vivaldi Antenna

PUR Polyurethane

RADAR Radio Detection And Ranging

RF Radiofrequency

SAR Specific Absortion Rate

SI International System of Units

SIW Substrate Integrated Waveguide

SMA SubMiniature version A

SONAR Sound Navigation And Ranging

UWB Ultra Wideband

VNA Vector Network Analyzer

Chapter 1

Introduction

1.1 Introduction

The discovery of X-Rays, in 1895, by Wilhelm Röntgen, marks the beginning of the medical imaging systems era. This allowed the advent of a new set of non-intrusive tools, which provided doctors with the ability to be more accurate with their diagnosis. Since the XIX century, several medical imaging systems have been proposed and used worldwide. Their medical area of application, shape and size, cost, technology and physical principles vary widely.

X-Rays have been used in several medical radiography techniques, such as projection radiography, fluoroscopy and computed tomography, mostly because they are able to penetrate soft tissue, but not the bone. However, X-Rays are an ionizing radiation, and the techniques that use them for medical imaging operate at very high frequencies, thus making them perilous to patients and technicians, if safety measures are not taken into account.

Magnetic Ressonance Imaging (MRI) became widely used after the 1970s to obtain image of soft tissue, something that the X-Rays could not achieve. The MRI technique works by positioning antennas near the body surface, which detect radiofrequency signals emitted by the atoms of the human body, when exposed to an intense external magnetic field. While not exposing the patient to ionizing radiation, intense magnetic fields tend to interfere with body implantable devices or metallic prosthesis.

There are also techniques, such as the Positron Emission Tomography (PET), which detect gamma rays emitted by radionuclides inserted inside the human body. While the produced images offer very high resolutions, the PET technique is very expensive and the patient is exposed to a high ionizing radiation dose.

Microwave imaging systems are being proposed as a complementary diagnosis tool [1]. It is not expected that these systems provide better image resolution than the aforementioned ones, but rather show a clear sign of existence of an anomaly that can require more indepth examinations, without exposing the patient to harmful ionizing radiations or complex procedures.

1.2 Motivation

Microwave imaging systems are expected to be affordable, portable and simple to operate. These systems shall be useful in scenarios where a significant dielectric constrast exists, namely in the detection of tumors and haemorrhages. In routine check-up procedures and precocious diagnosis, some of the traditional imaging techniques pose harm or discomfort to patients. For instance, in breast cancer detection women are typically exposed to high doses of ionizing radiation for each mammography, but this procedure is also painful and uncomfortable. A microwave imaging system would allow to perform the examination without pressing the breasts and without using ionizing radiation, since low energy microwave frequencies are harmless to humans. The portable aspect of microwave imaging systems also allows that these systems are deployed in emergency vehicles. In an accident situation, where a traumatic brain injury occurs, intracranial haemorrhage may appear and, the sooner it is detected and treated, the greater the chances of minimizing the issue. Therefore, by equipping emergency vehicles with microwave imaging systems, an examination may be performed when the transportation from the accident location to the hospital is taking place. This way, it is possible to know beforehand if any action is needed towards an intracranial haemorrhage situation upon reaching the hospital or not.

1.3 Objectives

This Thesis aims at developing a microwave imaging system for intracranial haemorrhages. In order to accomplish this task, an antenna with the suitable characteristics will be designed and manufactered. This antenna will be tested using a human head phantom, which shall emulate the eletric properties of real tissues, namely bone, brain and blood. Finally, an image reconstruction algorithm will be developed and used to, with the acquired data from the antenna, display an image of the phantom where it should be clear the existence of an haemorrhage.

1.4 Master Thesis Structure

This document is organized in 5 Chapters. In this first introductory chapter, a brief contextualization of the Thesis focus is done. Its motivations and objectives are also clarified.
In Chapter 2, the literature review is adressed, focusing the the investigation on three sections, which represent the key aspects of a microwave imaging system: Antennas Design, Phantoms and Image Reconstruction Algorithms. The suitable antennas and their properties are reviewed, several approaches in the design of phantoms are investigated and the image reconstruction inverse problem is adressed.
Chapter 3 is divided into two sections. The first discusses the design process of the ”Palm Tree Vivaldi” antenna (PTVA) , being a walkthrough from the Base Vivaldi Model to the complex and miniaturized PTVA design. The Chapter is concluded with the prototyping and testing of the designed antenna. The fabrication process is discussed and the measured antenna performance is compared with the simulated one.

In Chapter 4 the development of the Image Reconstruction Algorithm is discussed. In its first section, the Delay and Sum algorithm [2] is described and conceptually explained. Simulations are performed to illustrate its capability to present images of a scanning environment. The algorithm is first tested in the air, then in a complex propagation medium, emulating a human head. The algorithm is detailed and all stages of the developed program are discussed in this section. The Chapter is concluded by testing the developed algorithm with experimental measurements, with the use of the prototyped antenna and the built phantom.

Chapter 5 provides the concluding remarks of the presented document. It also lays the ground for future work in this topic to be conducted.

Chapter 2

State of the Art

The core concept behind a microwave imaging system is a monostatic radar [3]. An antenna emits a signal at a close distance to a target, a human head or breasts for instance, and detects the reflected signals by its different dielectric components. By performing this scan at multiple positions around the target, a set of signals can be obtained and then processed by an imaging algorithm. An image can then be obtained, which highlights the situations where high dielectric contrasts are present, which can be used to detect tumors or hemorrhages. To develop such systems, several obstacles have to be overcomed. While having a simple concept, there are several propagation media, with different permittivity values, ϵ_r. These values depend on the frequency, for instance, at $f = 2.45$ GHz, values of 11.35, 48.83 and 58.18 have been used for bone, brain and blood, respectively, in [4]. The existence of different dielectric boundaries and media not only causes several reflections of the emitted signal, leading to pulse distortion, but also to attenuation in those media, thus making an anomaly detection a difficult process, since the maximum emitted power is also limited [5]. Therefore, developing a suitable antenna is needed in order to correctly detect the anomaly attenuated reflections. While, futurely, this technique is expected to be used in humans, the investigation conducted nowadays must be done using phantoms. A phantom is an object which emulates the electric properties of several tissues of the human body [6], and producing the mixtures needed to do so is also a challenge. Finally, an imaging algorithm developed for this task is not trivial, since it attempts to solve an inverse problem. These problems aim at determining the causal factors that originated a set of observations. In a microwave imaging system problem, the goal of the algorithm is to detect the anomaly which caused the measured reflected signals at the antenna. All these challenges have to be taken down in order to, eventually, produce a prototype that may be used to aid medical staff.

2.1 Antennas Design

Since the use of milimiter waves does not pose the dangers of ionizing radiations, their use is desired for medical applications. In particular, for a human head, the microwave spectrum band of 1-3 GHz is suggested, since it offers enough penetration into the tissue [3]. Ideally, the emitted signal should use most of this band, therefore providing the Ultra Wideband (UWB) characteristic, in order to improve signal

resolution [3]. UWB is a technology for short-ranged communications and is defined, for the International Telecommunication Union - Radiocommunication (ITU-R), as the characteristic of a device that has a -10 dB bandwidth of at least 500 MHz, or a -10 dB fractional bandwidth greater than 0.2 [7]. This is the definition of UWB followed throughout this work, since the Federal Communications Commission (FCC), also defines UWB as the electromagnetic spectrum frequencies from 3.1-10.6 GHz, which are available for unlincensed use [8]. As stated previously, a microwave imaging system is expected to be small, portable and cheap, therefore, the antennas must also possess these characteristcs. It is, however, a challenge to develop small antennas for the lower frequencies of the 1-3 GHz band due to the relation between operating frequency and the radiating element's size. While, for breast cancer detection an immersion medium for the scanning may be used to reduce the antenna's size [9], the same methods are not applicable for intracrianal tumor or hemorrhage detection. These antennas must also have a high fidelity factor, which measures the reflected signal distortion when compared to the emitted one [10]. Maintaining the pulse shape is fundamental to detect correcly the several reflections that occur in a complex propagation medium, such as the human head. Finally, these antennas should be able to illuminate a small area in the scanning region, in order to improve the accuracy of the performed measurements. By fulfilling these requirements, quasi-Yagi antennas are the most suitable ones to be developed, due to their easy fabrication process, low cost, compact and lightweight structure [11]. The suggestions presented in the literature vary from electromagnetic horns to monopoles, planar and bowtie antennas, Substrate Integrated Waveguide (SIW) printed antennas [11], dipoles [12] [13] and Vivaldi antennas [9] [14]. None of the available solutions can be depicted as the best antenna for a microwave imaging system, since all have strenghts and weaknesses that must be taken into consideration. Horns are the bulkiest of these antennas, while monopoles, planar and SIW printed antennas tend to create a cavity effect due to the proximity of the human body, thus introducing a lot of signal distortion and loss of power that is expected to be transmited inside the body. Finally, dipoles tend to be modified in such a way that impedance matching, front-to-back ration and -10 dB bandwidth are improved. This can be achieved by adding copper plate furls, stubs and parasitic elements [13] [15]. The designs described in the aforementioned literature achieve UWB in the sought microwave band, while also having a fidelity factor close to the unity (the fidelity factor ranges from 0 to 1). However, these dipoles' designs tend to be bulkier due to their thickness, which is something to avoid in a real world scenario. With that in mind, Vivaldi antennas are suggested as a thin antenna that aims at solving the issues raised with the previously discussed designs. Vivaldi antennas are characterised by having a curvilinear geometry from the feeding point to the aperture, on the other end [16]. These antennas are usually designed taking into account the lowest desired frequency of operation, which, in this case, results in a quite large antenna, around the desired wavelength [17]. There are, however, novel designs that allow Vivaldi antennas to be more compact, such as the removal of substrate parts [18], the folding of the metallic layers to the other face of the antenna [19] or even cutting the metallic layer following certain geometries [20]. These strategies aim at lengthening the electrical dimensions of the Vivaldi antenna, while maintaining, or even reducing, its physical size by changing the surface currents distribution behaviour. Taking these novel features into the Vivaldi antennas' designs, it is possible to attain the desired characteristics, namely

operating frequency and UWB in the sought band, compact structure and high fidelity factor.

2.2 Phantoms

Phantoms also represent a key role in this work, therefore, it is important to refer them in the State of the Art. Phantoms are objects that emulate the electric properties of living tissue and they are used to tune medical imaging devices, measure mobile phones Specific Absortion Rate (SAR), among other purposes. Depending on the complexity required, phantoms may be either simple models or more accurate 3D printed ones [6] filled with liquid, semisolid or solid mixtures. In order to determine the permittivities of human tissue, the Cole-Cole model, which is an extension to the simpler Debye Relaxation Model, is used [4], after which the different mixtures may be produced, using materials such as glucose, sodium chloridre, diacetin or di-etyhlene glycol buthyl ether (DGBE).

2.3 Image Reconstruction Algorithms

Finally, in order to present an image using the data collected by the antennas, after the scans on phantoms, an imaging algorithm has to be developed. Sound Navigation And Ranging (SONAR) and Radio Detection And Ranging (RADAR) techniques have widely used after the II World War, and its applications range from military purposes, to air and maritime navigation and meteorology. Altough these techniques are widely used, an algorithm applied to microwave imaging must be simpler and require less computational resources. So, algorithms such as the Delay And Sum (DAS) [2], Delay Multiply And Sum (DMAS) [21] and Kirchoff Migration [22] are preferred to when solving the microwave image reconstruction inverse problem. While the Kirchoff Migration algorithm operates in the frequency domain, the DAS and DMAS are time domain algorithms. The concept behind the DAS and DMAS is the summation of received signals, after a certain delay is introduced, so that they add constructively, resulting in signals with small amplitudes (such as the reflection of an anomaly, for instance) to be distinguishable from background noise and higher ampltidude signals. In order to implement these algorithms, a propagation model for the medium has to be developed [15], based on Fermat's Principle [1], which states that light travelling time has to be the minimum between a set of two points, taking into consideration the different media, their permittivities and antenna introduced delays. Aided by Fourier Analysis [1], it is possible to synthesize the reflected signals in the time domain after measuring the antenna's reflection coefficient, S_{11}, in the frequency domain, in the presence of a phantom with an anomaly. With the synthesized signals it is possible to use the algorithm and the designed propagation model to display an image of the scanned region, highlighting the situations where a noticeable dielectric contrast occurs.

Chapter 3

Palm Tree Vivaldi Antenna Design

This Chapter aims at describing all the steps followed throughout the design of the proposed ”Palm Tree Vivaldi” antenna [20]. CST Studio Suite simulations are performed throughout the Chapter, which is concluded by comparing the simulated results with the experimental ones, after the Palm Tree Vivaldi antenna production.

3.1 Palm Tree Vivaldi Antenna Design Steps

3.1.1 Vivaldi Antenna Base Model

The design of the proposed Vivaldi antenna, which is seen in figure 3.1 follows the guidelines present in [14]. The antenna's width and length were to be made equal, $w = l$, and were suggested to be

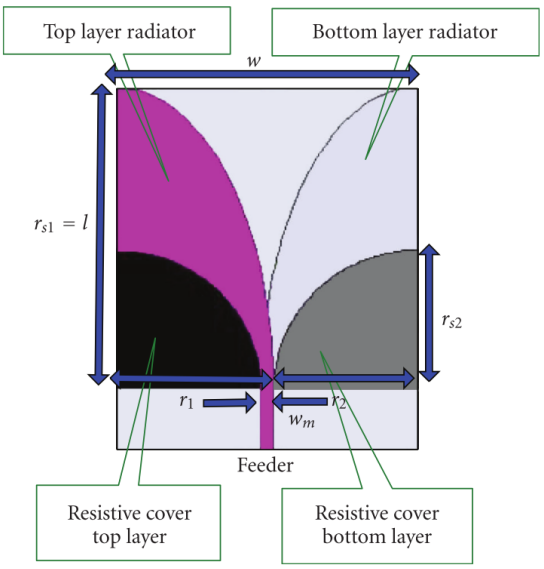

Figure 3.1: Vivaldi antenna designed and prototyped in [14].

calculated according to

$$w = l = \frac{c}{f_l}\sqrt{\frac{2}{\epsilon_r + 1}} \tag{3.1}$$

Table 3.1: Vivaldi Antenna Parameters

Fixed Parameters	Variable Parameters
h, h_{ant}, ϵ_r	w, l, w_m

with c the speed of light in vacuum, f_l the lowest operating frequency of the antenna and ϵ_r the substrate permittivity. This condition allows the antenna dimensions to be equal to its effective wavelenght. As discussed in the State of the Art, the 1-3 GHz frequency band is desired for microwave imaging in the head. Therefore, by keeping the f_l parameter constant, a value for ϵ_r had to be chosen from the datasheets of substrate providers, namely Rogers Corporation [23]. Since there is a dependency of the bandwidth with the substrate's permittivity and thickness [24] [25], which states that, for a given constant substrate thickness, the lower the permittivity, the greater the bandwidth. With this information taken into account, a Rogers RT5880 substrate, with the lowest permittivity available, $\epsilon_r = 2.2$ for a substrate thickness of $h = 0.75$ mm was chosen in order to maximize the available bandwitdh, since there are strategies to miniaturize the antenna physical dimensions while maintaining the operating frequency band. Due to a photolitographic process being used to print the copper metalization in the substrate, it was considered a height of $h_{ant} = 0.0035$ mm for the metallic layer. All parametrization for the Vivaldi antenna is condensed in Table 3.1. Since the dimensions suggested from expression 3.1 are quite large for the dimensions desired for an antenna that will be deployed in a microwave imaging scenario, it was considered that w, l and w_m are variable parameters of the antenna, that shall be optimized in order to attain a small and compact antenna that operates, with UWB, in the desired frequency band. Several experiments were conducted using CST Studio Suite to evaluate the condition imposed by expression 3.1, that $w = l$. Since the objective is to adapt the antenna's dimensions to the 1-3 GHz band, a design that didn't have a squared geometry was chosen. The radiators curvature was obtained from the intersection of quarter of ellipses defined according to expressions 3.2 to 3.5.

$$r_1 = \frac{w}{2} + \frac{w_m}{2} \tag{3.2}$$

$$r_2 = \frac{w}{2} - \frac{w_m}{2} \tag{3.3}$$

$$r_{s1} = l \tag{3.4}$$

$$r_{s2} = 0.5 r_2 \tag{3.5}$$

By taking the centers of the ellipses as the points of coordinates $(x, y) = (-w/2, 0)$ mm and $(x, y) = (w/2, 0)$ mm, it is possible to define the base Vivaldi antenna layout by plotting the aforementioned expressions.

The points that belong to the geometrical space generated between the two curves constitutes the copper metalization layers of a Vivaldi antenna, the radiators, as seen in figure 3.3. It should be noted that the microstrip line must also be designed so that it allows the connection from the radiators to an SMA connector.

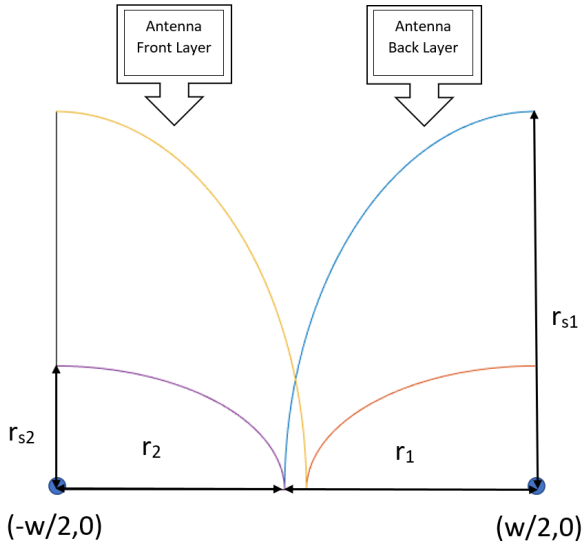

Figure 3.2: Vivaldi antenna front and back curvatures.

For a single microstrip line, expression 3.6 can be used to compute its width,

$$w_m = \frac{120\pi}{\sqrt{\epsilon_r}} \frac{h}{Z_0} \tag{3.6}$$

, with h being the thickness of the substrate, Z_0 the desired impedance and ϵ_r the substrate permittivity. However, it should be noted that in the situation that two microstrips are placed on top of eachother, in each face of the substrate, equation 3.6 must be seen as an estimation, and not a defining expression. The ground plane was designed using an elliptical transition from the microstrip line to the edge of the substrate layer, thus allowing to weld the SMA connector.

The proposed antenna from [14] was intended to work on the UWB band of the electromagnetic spectrum (FCC [8]), which falls ahead of the desired 1-3 GHz band for Microwave Imaging on the human head. Therefore, several modifications were performed on the first design. It was chosen to have the possibility of different microstrip widths on each face of the antenna, thus increasing the degrees of freedom in impedance matching for the connector inclusion. The possibility of creating mitered transitions [26] was also taken into account, allowing a smoother transition between the feeding point of the antenna and the radiators. In the original design, the microstrip lines were on top of eachother, thus overlapping on each face of the substrate. An important step was to turn them into two non completely overlapping microstrip lines. So, the top layer radiator curvatures are shifted by half the dimensions of the top microstrip width at the microstrip-radiator interface. This allows to obtain the desired nature of the microstrips, thus reducing antenna reflections, which is expected to improve the antenna's S_{11} parameter. Taking these modifications into account, an initial CST Studio Suite model was designed. Using expressions 3.2 to 3.5 to design all the ellipses, but shifting the front layer radiator ones by

$$\Delta s = \frac{w_m}{2} \tag{3.7}$$

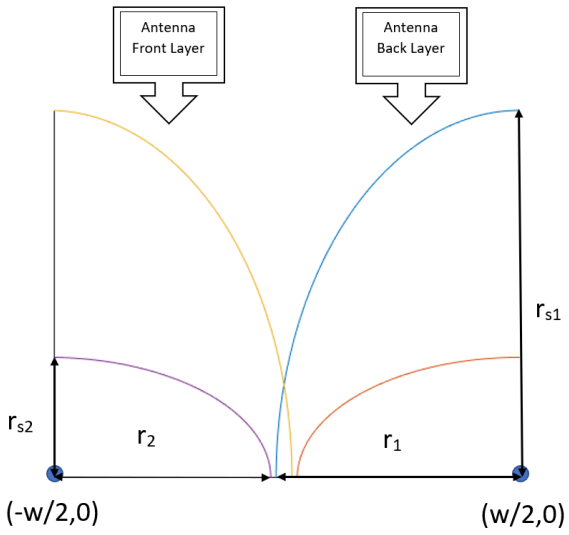

Figure 3.3: Vivaldi antenna shifted front curvature and back curvature.

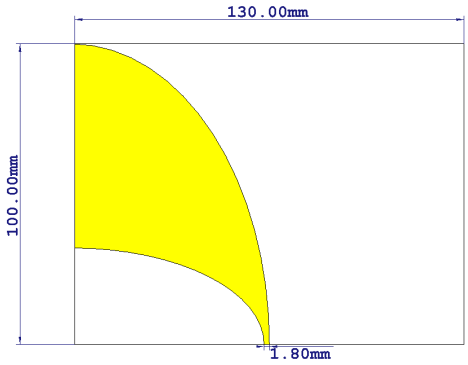

Figure 3.4: Vivaldi antenna front radiator.

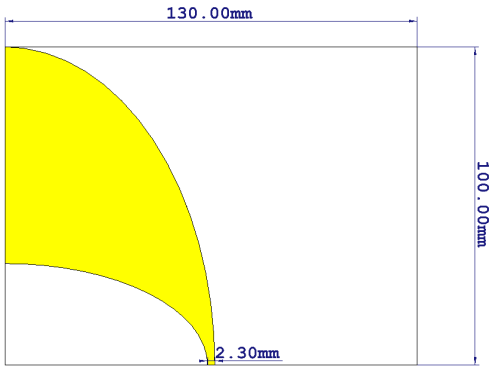

Figure 3.5: Vivaldi antenna back radiator.

the radiators were designed, on top of a 130 mm $\times$ 115 mm $\times$ 0.75 mm layer of Rogers RT5880 ($\epsilon_r = 2.2$) substrate. The radiators themselves occupy an area of 130 mm $\times$ 100 mm, with the remaining 15 mm being for the microstrip line conection to the feeding point. The thickness of the substrate is imposed by the manufacturer, which is roughly 30 mils (thousandth of an inch), that, converted to the International System of Units (SI) , is roughly 0.75 mm. Taking the suggested w_m value yielded by 3.1, by simulating the reference impedance, Z_0, of this particular design, it was obtained a combination of values for the front and back layers of the antenna. For the front layer, the microstrip line width, w_m is 1.8 mm and, for the back layer, is 2.3 mm. The radiators models, as seen in CST Studio Suite, are shown in figures 3.4 and 3.5.

The microstrip line was designed, as stated above, in such a way that there was no complete overlap betweeen the lines on both faces of the substrate. While, on the back side of the antenna, a straight microstrip line connects the radiator to the ground plane with $w_m = 2.3$ mm, centered at the coordinates $(x, y) = (0, 0)$ mm, on the front layer of the Vivaldi antenna, a mitered transition is used from the radiator to the feeding point. This microstrip line starts in the shifted front radiator, thus being centered in coordinates $(x, y) = (-\frac{3w_m}{2}, 0)$ mm, with $w_m = 1.8$ mm. Since the feeding point of the Vivaldi will be

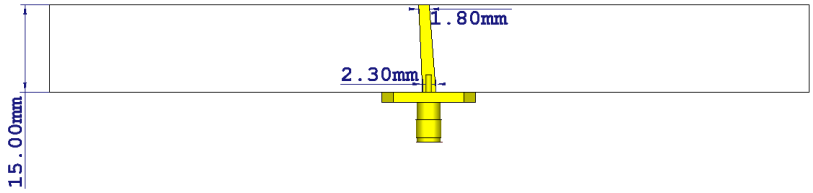

Figure 3.6: Vivaldi antenna front microstrip line and SMA connector view.

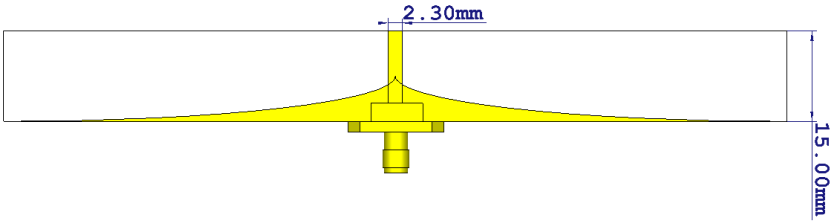

Figure 3.7: Vivaldi antenna back microstrip line, ground plane and SMA connector view.

centered in the coordinates $(x, y) = (0, -15)$ mm, the microstrip line transitions converges that point, while linearly increasing its width to $w_m = 2.3$ mm in order to guarantee the desired 50 Ω reference impedance. The ground plane also followed an elliptical design, with the curvature starting at the coordinates $(x, y) = (0, -7.5)$ mm, going to both vertices of the substrate. In order to start the simulations using CST Studio Suite, an SMA connector was also included in the design, with copper blocks simulating the weld deposits that will keep together the antenna and the connector, thus producing more realistic and conservative results. The SMA connector model represents a commercial connector that is available for purchase, with Teflon ($\epsilon_r = 2.1$) being used as dielectric. Figures 3.6 and 3.7 show the microstrip lines and the SMA connector welded to the Vivaldi antenna feeding point and ground plane.

The full view of the designed Vivaldi antenna is presented in figure 3.8, with this design having a total volume of 130 mm $\times$ 115 mm $\times$ 0.82 mm, considering a copper metalization height, on each layer, $h_{ant} = 0.035$ mm (recommended value according to [27]).

Using CST Studio Suite Time Domain Solver, with hexahedral meshing, for a -40 dB accuracy check, the S_{11} parameter was simulated. Since, in Microwave Imaging Systems, the antennas are radiating in the near-field zone of the antenna, neither the radiation pattern neither the gain are defining parameters to look at, due to their relevance being mostly on the farfield region. Because, at the highest operating frequency of 3.9 GHz, which corresponds to a minimum wavelength of 7.7 cm, according to 3.8,

$$\lambda = \frac{c}{f} \tag{3.8}$$

and that the farfield condition is satisfied for a given distance

$$r >> 2\lambda \tag{3.9}$$

it is clear that, for a Microwave Imaging System, the antennas are radiating in the near-field region. However, in order to also assess if the designed Vivaldi antenna is directive enough to illuminate a small

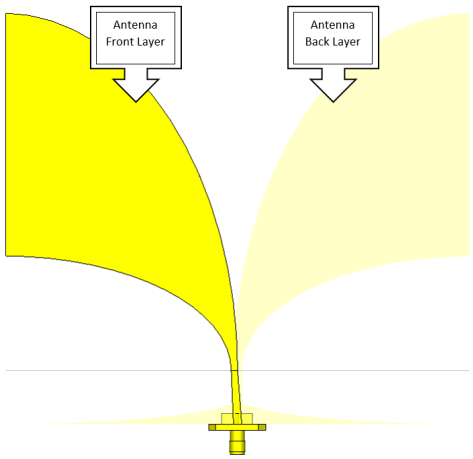

Figure 3.8: Designed Vivaldi antenna.

target area, the simulated farfield is also provided, for the central frequency of operation, since this is one of the desired characteristics of an antenna for Microwave Imaging Systems.

From figure 3.9 it is possible to confirm that the designed Vivaldi operates in most of the desired 1-3 GHz

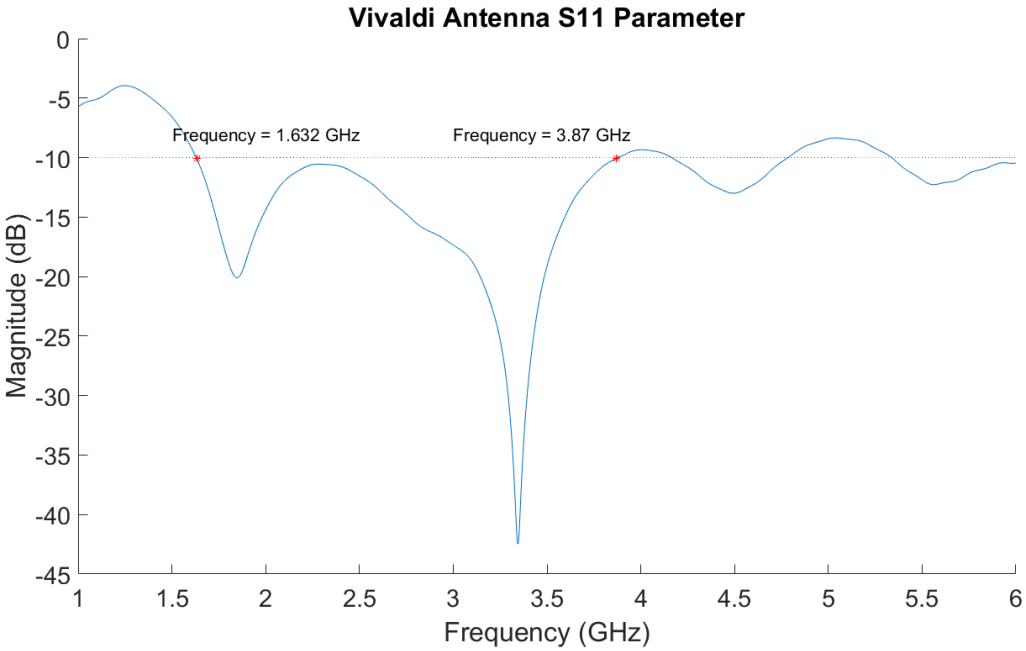

Figure 3.9: Designed Vivaldi antenna S_{11} parameter.

band. It is important to note that, for lower operating frequencies, the size of the aperture increases, which is undesired. With this design, a bandwidth of 2.23 GHz is obtained, granting this antenna the desired UWB characteristic, centered at frequency of 2.75 GHz, with the lowest frequency of operation being $f_L = 1.632$ GHz and the highest, $f_H = 3.87$ GHz The estimated reference impedance, with the SMA connector is 55.3 Ω. By observing the radiation pattern in figure 3.10, for the central frequency

of 2.75 GHz, it is clear that the designed Vivaldi antenna has a well defined radiation pattern, with its maximum gain (hence directivity) having a clear orientation. It is expected that, with this being taken into consideration, that the antenna achieves the capability to illuminate the area of interest in the desired scanning region.

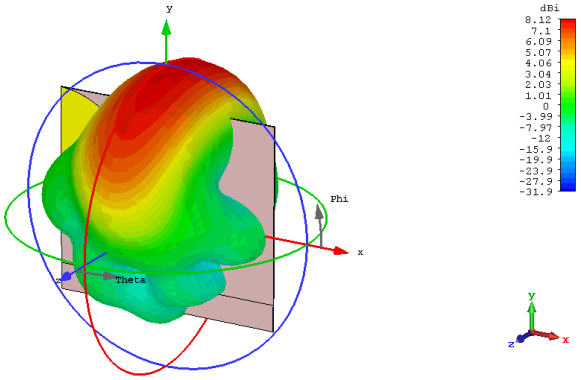

Figure 3.10: Designed Vivaldi antenna far field radiation pattern.

Finally, the reflected pulse distortion of the proposed antenna is also evaluated. In order to achieve this, a copper plane was placed 10 cm in front of the Vivaldi antenna. The S_{11} parameter of the antenna, in free space and with the metal plane present are measured. Then, according to the work of [28], it is possible to consider the S_{11} parameter as the transfer function, $H(f)$, of a Linear and Time Invariant System (LTIS). Its input can be synthesized in Matlab, with the output being the received signal at the antenna, after the reflection from the metal plane. It is important to calibrate the antenna with the metal plane S_{11} parameter by subtracting the free space S_{11} parameter. This process is schematized in figures 3.11 and 3.12.

In order to obtain the output of the LTIS in the time domain, it is necessary to synthesize a time domain input signal, for instance a gaussian shaped pulse, described by expression 3.10

$$u(t) = cos(2\pi f_c t)e^{-2\pi(t/\tau)^2} \tag{3.10}$$

which may be written, in the frequency domain, using the Fourier Transform,

$$U(f) = \int_{-\infty}^{+\infty} u(t)e^{-j2\pi ft}\, dt \tag{3.11}$$

thus allowing to obtain the output signal, $v(t)$, after computing

$$V(f) = U(f)H(f) \tag{3.12}$$

and, following expression 3.12, applying the Inverse Fourier Transform

$$v(t) = \int_{-\infty}^{+\infty} V(f)e^{j2\pi ft}\, df \tag{3.13}$$

The simulation setup, in CST Studio Suite, is shown in figure 3.13. Applying the aforementioned process

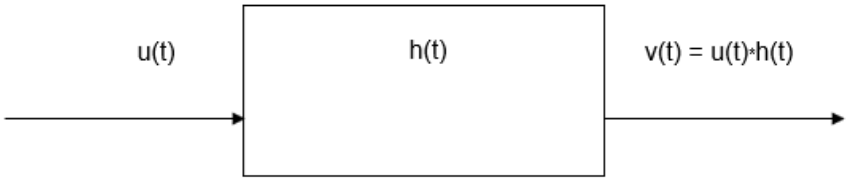

Figure 3.11: LTIS in the time domain.

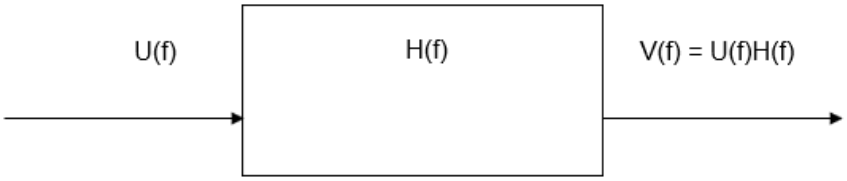

Figure 3.12: LTIS in the frequency domain.

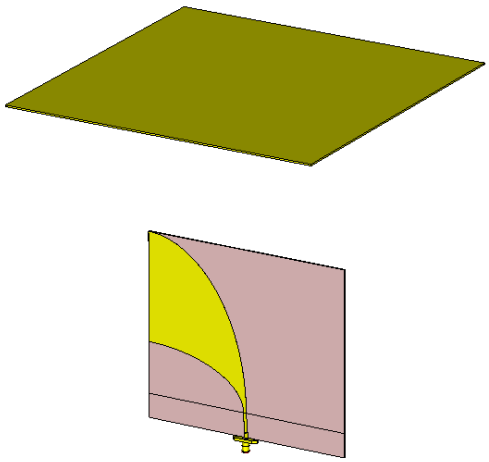

Figure 3.13: Simulation setup for pulse distortion assessment.

and, using expressions 3.11 to 3.13, it is possible to plot the input signal, synthesized using expression 3.10, and the reflected signal from the copper plane. From figure 3.14, it is possible to confirm that the designed Vivaldi antenna also introduces some pulse distortion on the received signals, altough the signal shape and its maximum peak are clearly detected. It is important to note that the reflected signal is normalized in respect to its maximum amplitude value. The reflected signal is delayed, relative to the instant $t = 0$ ns by the 20 cm travelled in the air and by the propagation from the feeding point along the antenna.

Concluding this section of the text, the proposed and designed Vivaldi antenna fulfills the main defining points that are required for a Microwave Imaging System. The operating frequency band is used, the antenna exhibits UWB properties, is capable of illuminating a focused region due to its directivity and introduces small signal distortion. However, the dimensions for this antenna to be implemented in a prototype of a device could be reduced. In order to also accomplish this requirement, in section 3.1.2, a

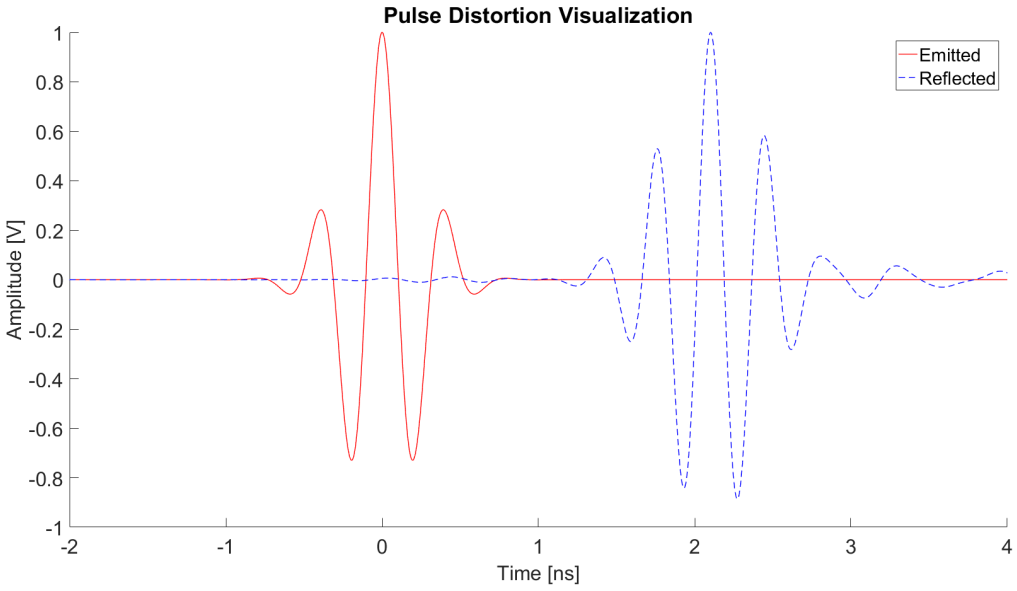

Figure 3.14: Synthesized emitted pulse (red) and reflected received pulse (dotted blue).

strategy that allows to miniaturize the Vivaldi antenna is explored.

3.1.2 Palm Tree Vivaldi Antenna Model

In order to comply the requirements for an antenna for a Microwave Imaging System, a logical step is to miniaturize the dimensions of the antenna. An interesting design is to modify the radiators in such a way that the electrical wavelength is increased, thus allowing to reduce their physical dimensions. Following the works presented in [20], it was decided to include resonator edges to the original design. According to the literature, including rectangular shaped edge slot resonators degraded the lower frequency of operation in comparision with the base Vivaldi antenna, while triangular or elliptical shapes improved performance for the lower frequencies [20]. This behaviour is typical for printed circuits, since it is preferred to use mitered and smooth transitions. Depending on the radiator's size, complexity in the cuts design and electrical length desired, the number and orientation of the edge slots may be defined.
In this design, three equal triangle edge slots were introduced in each radiator. The coordinates of the first triangle vertices, for the front radiator, are as follows

$$(x_1, y_1) = (-\frac{w}{2}, l) \tag{3.14}$$

$$(x_2, y_2) = (-\frac{w}{2}, 0.5 \times \frac{w - w_m}{2} + \frac{l}{2}) \tag{3.15}$$

$$(x_3, y_3) = (-\frac{w}{4}, 0.5 \times \frac{w - w_m}{2} + \frac{l}{2}) \tag{3.16}$$

with w_m being the mininum microstrip line width used in both the front and back layer, thus having the value of $w_m = 1.8$ mm. These can be seen in figure 3.15.
The presented edge slot resonator was then translated, in CST Studio Suite, in respect to the yy axis by

expression 3.17

$$\Delta d = -0.3 \times \frac{w - w_m}{2} \tag{3.17}$$

with the newly added resonator also being translated by the same distance, in respect to the second edge slot. This creates a thin distance of $d_{sp} = 1.28$ mm between each edge slot, computed by first determining the distance between the vertix in coordinates (x_1, y_1) and the coordinates of the same vertix on the second resonator, using expression 3.18

$$\Delta d_1 = l - \Delta d \tag{3.18}$$

and then subtracting the distance between it and the vertix in coordinates (x_2, y_2), according to expression 3.19

$$\Delta d_{sp} = \Delta d_1 - (0.5 \times \frac{w - w_m}{2} + \frac{l}{2}) \tag{3.19}$$

hence resulting in the aforementioned value. This procedure is illustrated in figure 3.15, using the front radiator as the example. In order to introduce the resonators on the back one, the only modification is to take the positive values for the xx coordinates. The dimensions of the antenna, at this point, are kept the same as the ones described in section 3.1.

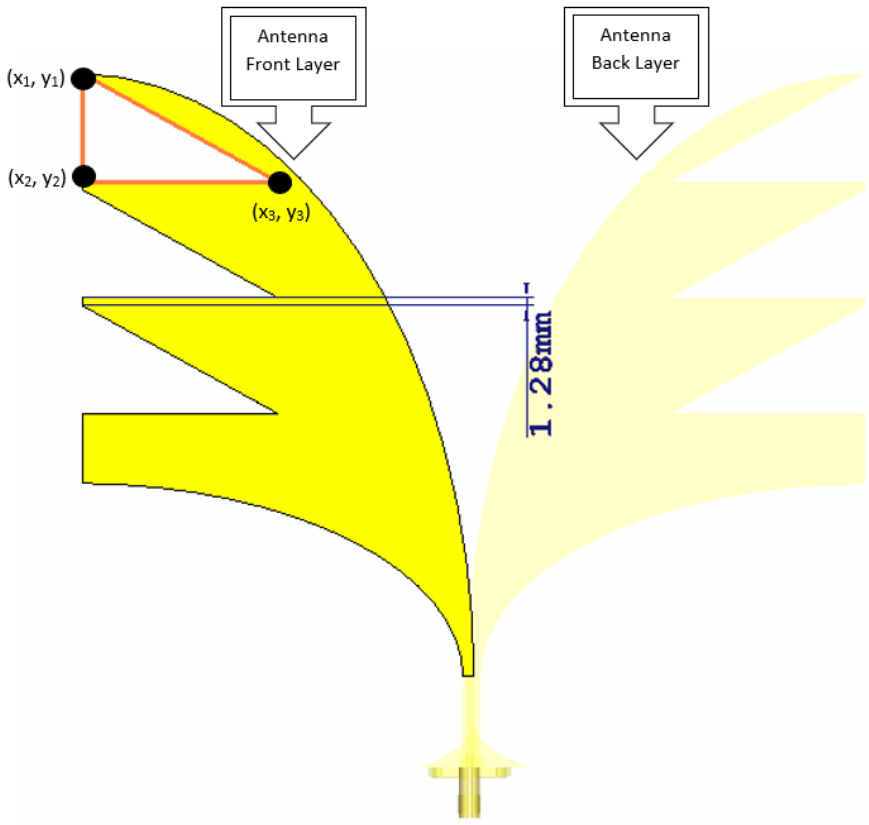

Figure 3.15: Designed Palm Tree Vivaldi antenna resonators.

Table 3.2: Current path effect on lower frequency of operation

	Base Vivaldi Model	Palm Tree Vivaldi
Current Path [mm]	67.94	222.93
f_L [GHz]	1.632	1.400

The last change performed on the base model of the Vivaldi antenna is in the ground plane. In order to make the antenna production easier, the ground plane had to be made smaller, when compared to the designed one from figure 3.7. Since the ground plane doesn't have a significant impact on the relevant parameters, it can be modeled in order to match the dimensions of the connector. The designed microstrip transmission line transition and the modified ground plane are presented in figure 3.16.

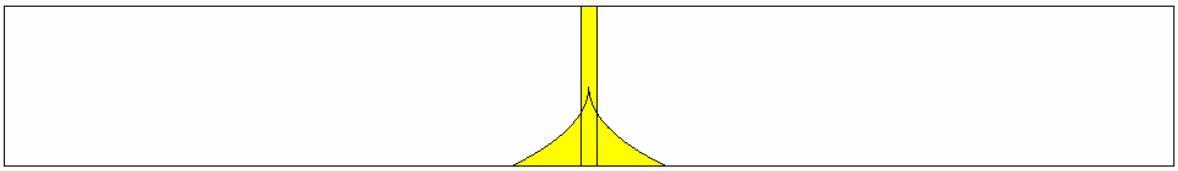

Figure 3.16: Modified Palm Tree Vivaldi antenna ground plane.

In order to assess the changes that were introduced, the Palm Tree Vivaldi S_{11} parameter was simulated. For a reference impedance of 49.5 Ω, figure 3.17 illustrates the changes in relation to the design of section 3.1. As expected, since the resonators enlarge the electrical dimensions of the antenna, the lower frequency of operation deviates from $f_L = 1.632$ GHz to $f_L = 1.4$ GHz. The higher frequency of operation is also affected by roughly the same deviation, therefore, keeping the antenna bandwidth roughly the same, in 2.2 GHz. The resonators also smooth the S_{11} parameter curvature, eliminating the 3.4 GHz ressonance, which, while not undesirable, is an adaptation value that isn't needed. However, the S_{11} parameter is, on average, lower with the Palm Tree Vivaldi antenna design rather than the Base Vivaldi model. By observing Table 3.2, which accounts the dimensions of the modified radiator path for the surface currents, it is possible to see that, by adding the three resonators, this path increases by

$$\Delta p = 222.93 - 67.94 = 154.99 \text{ [mm]} \tag{3.20}$$

while the lower frequency of operation, f_L, decreases by

$$\Delta f_L = 1.632 - 1.400 = 0.232 \text{ [GHz]} \tag{3.21}$$

therefore, by computing the frequency variation with the path dimensions, denoted as α, results in

$$\alpha = \frac{\Delta p}{\Delta f_L} = 1.497 \times 10^{-3} \text{ [GHz/mm]} \tag{3.22}$$

According to expression 3.22, it is made clear that it is possible to adjust the lower and upper frequencies of the operating band, while keeping the bandwidth and physical dimensions of the antenna constant. It is also important to assess if the changes made to the antenna affect the radiation patter.

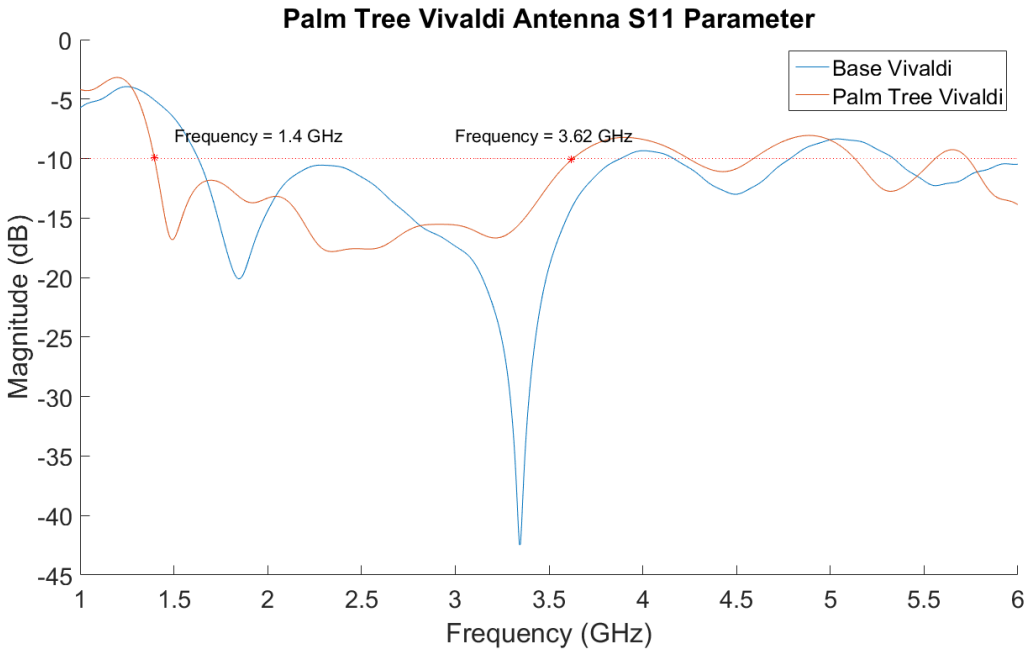

Figure 3.17: Designed Palm Tree Vivaldi antenna S_{11} parameter comparison with Base Vivaldi antenna model.

Therefore, using CST Studio Suite, the farfield behaviour of the Palm Tree Vivaldi was also simulated for the central frequency of the operating band, $f = 2.5$ GHz, with its plot being shown in figure 3.18. The radiation pattern is unaltered, with the directive characteristics of this antenna being kept the same, therefore allowing the illumination of a small area while scanning a target.

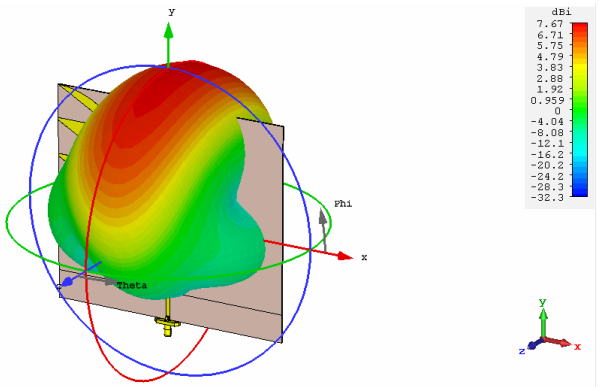

Figure 3.18: Designed Palm Tree Vivaldi antenna far field radiation pattern.

Using the same simulation setup that was introduced in figure 3.13 for the Vivaldi antenna base model, the S_{11} parameter was measured for free space and with a copper plane, placed at 10 cm from the Palm Tree Vivaldi antenna. Then, following the aforementioned process, summarized in figures 3.11 and 3.12 and expressions 3.10 to 3.13, the signal distortion is evaluated, at the central frequency of operation of the antenna, $f = 2.5$ GHz. The corresponding plot is presented in figure 3.19. Like in the base model design, there is some signal distortion, with the shape and peak detection still being very clear. The introduction of the resonator edges didn't modify the signal distortion of the designed antenna, therefore creating a degree of freedom that can be explored in order to miniaturize the Palm Tree Vivaldi antenna.

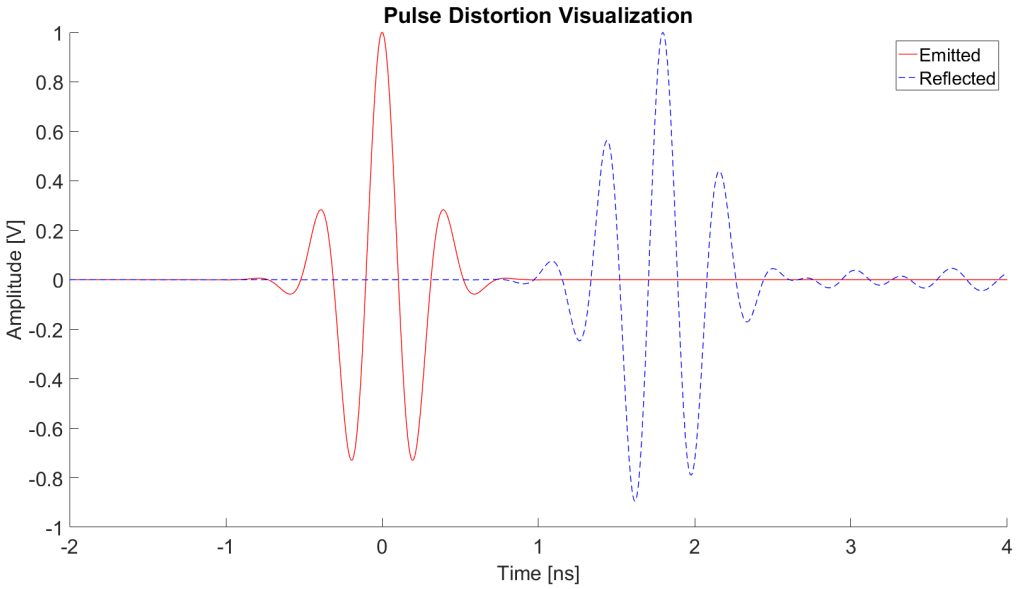

Figure 3.19: Synthesized emitted pulse (red) and reflected received pulse (dotted blue).

Table 3.3: Palm Tree Vivaldi antenna parameters

Antenna Parameters	
Substate thickness	$h = 0.75$ mm
Copper metalization height	$h_{ant} = 0.035$ mm
Substrate permitivity	$\epsilon_r = 2.2$
Width	$w = 110$ mm
Length	$l = 95$ mm
Microstrip Line Width	$w_{m_{top1}} = 1$ mm
	$w_{m_{top2}} = 1.5$ mm
	$w_{m_{back}} = 1.5$ mm
Connector gap	$gap = 0.5$ mm

Being free to reduce the Palm Tree Vivaldi antenna dimensions, a model was produced that changed its width to 115 mm and it's length to 95 mm, while also adjusting the microstrip lines widths in order to match the impedance at 50 Ω. Reducing the dimensions even further would require aditional geometries for the resonators, as the S_{11} parameter, in the lower frequency of operation, would degrade substantially. No aditional reductions to the Palm Tree Vivaldi antenna were performed, however, since at this dimensions a compact and thin enough structure was already achieved. At this point of the work, it was already made clear the way to follow if aditional size reductions were needed.

The final model for the Palm Tree Vivaldi antenna is now presented, with the desired compact nature of the structure, its UWB characteristic in the interest frequency band, directive behaviour and small pulse distortion. The Palm Tree Vivaldi model that was defined above is the one to be produced, with all dimensions and parameters being described in Table 3.3. The connector gap parameter is just a tiny removal of 0.5 mm of microstrip line near the connector feeding point. It was done in order to make the welding process easier and also to aid the impedance matching. The two values for the front layer microstrip width, $w_{m_{top1}}$ and $w_{m_{top2}}$, represent the widths at the start of the line and at the end, in the connector feeding point, as seen in figures 3.20 and 3.21. The front and back radiators occupy and

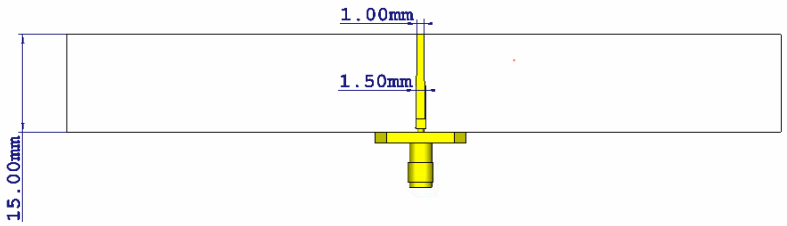

Figure 3.20: Palm Tree Vivaldi antenna front microstrip line and SMA connector view.

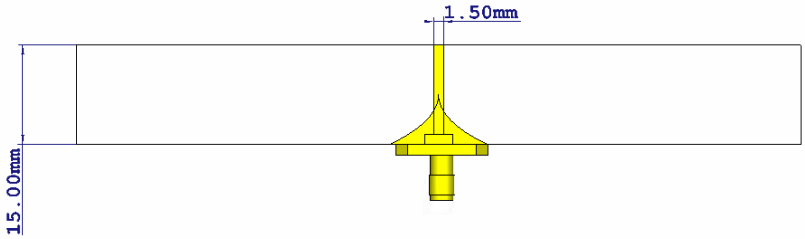

Figure 3.21: Palm Tree Vivaldi antenna front microstrip line, ground plane and SMA connector view.

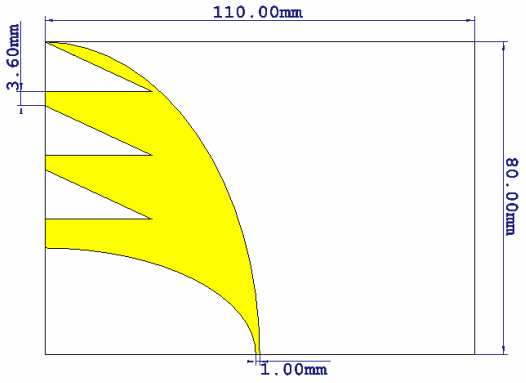

Figure 3.22: Palm Tree Vivaldi antenna front radiator shape.

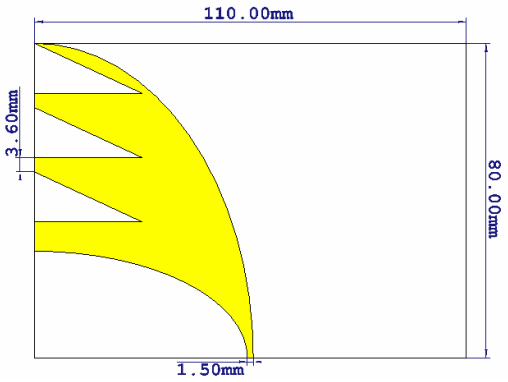

Figure 3.23: Palm Tree Vivaldi antenna back radiator shape.

area of 115 mm $\times$ 80 mm and feature the resonator edge slots described above. The coordinates of the first triangle that constitutes the resonator are also described by expressions 3.14, 3.15 and 3.16. Likewise, the translations are also determined by expression 3.17, in which the value for w_m is also the minimum microstrip width value, hence $w_m = 1$ mm. The spacing between the resonators is, with these dimensions, again computed with expresions 3.18 and 3.19, yielding a value of $d_{sp} = 3.60$ mm. All this information is summarized in figures 3.22 and 3.23. The Palm Tree Vivaldi antenna model that will be used to produce the antenna is, finally, shown in figure 3.24.

The assessment of the miniaturization of the Palm Tree Vivaldi antenna began by evaluating the reference impedance, which was kept at the 49.5 Ω obtained with the previous dimensions. The S_{11} parameter was simulated, using CST Studio Suite, and, as seen in figure 3.25, the desired UWB characteristic is kept, with the lowest frequency of operation, $f_L = 1.581$ GHz, and the highest, $f_H = 2.89$ GHz, granting a bandiwdth of 1.31 GHz, centered at 2.24 GHz. While the simulated bandwidth is smaller than

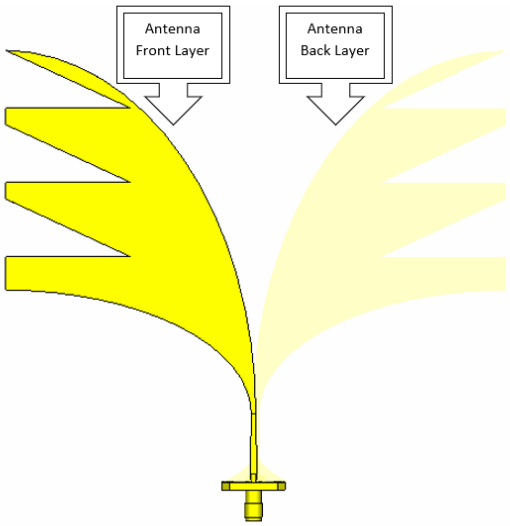

Figure 3.24: Designed Palm Tree Vivaldi antenna.

the ones obtained on the previous designs (around 2.2 GHz), it is important to notice that most of this reduction occurs outside the desired 1-3 GHz frequency band that grants the best trade-off between resolution and penetration in a Microwave Imaging System. Therefore, the reduction on the Palm Tree Vivaldi antenna's bandwitdh after its miniaturization is not problematic, but rather a small price to pay to have the antenna structure becoming more compact, while keeping the sought UWB behaviour.

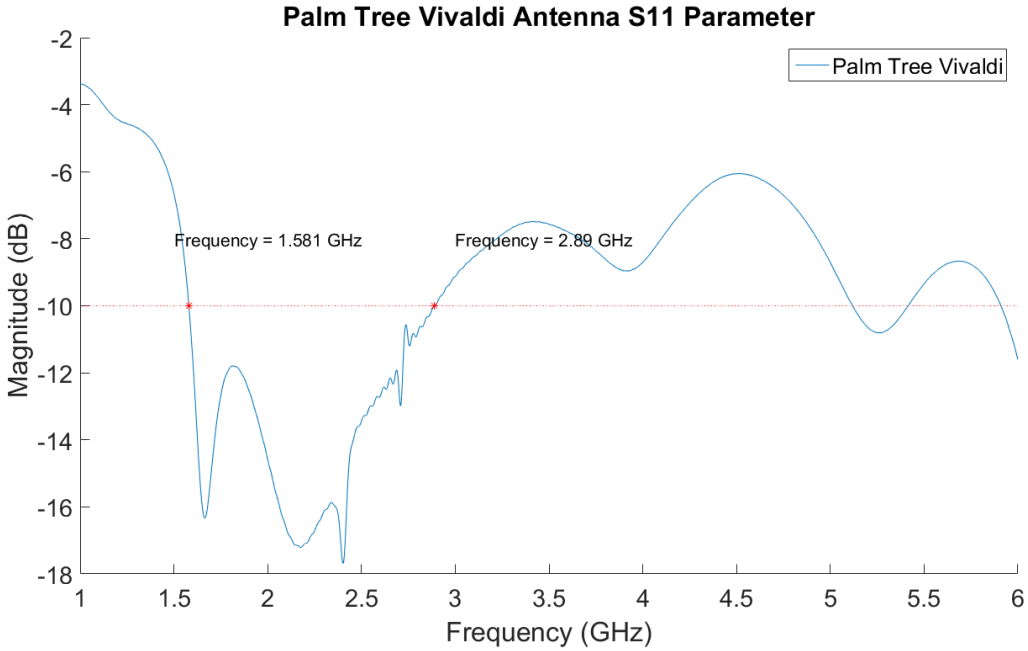

Figure 3.25: Designed Palm Tree Vivaldi antenna S_{11}.

Based on the previous experiments, it is expected that the Palm Tree Vivaldi antenna's radiation pattern is unchanged, thus leading to a desirable directive behaviour in order to promote a small illumination of the scanning target. The absolute view of the radiation pattern is seen in figure 3.26, for the central

frequency of operation.

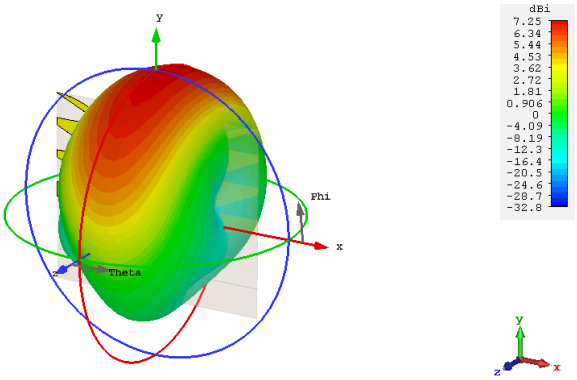

Figure 3.26: Designed Palm Tree Vivaldi antenna far field radiation pattern.

Since this is the model that shall be produced, it is important to also analyse the electric field behaviour and the surface currents distribution. As it has been described throughout the text, the Palm Tree Vivaldi antenna was designed in xy plane. Therefore, with the design of figure 3.24 and the radiation pattern of figure 3.26, it is clear that propagation occurs on the yy plane. The electric field was simulated, at $f =$ 2.24 GHz, and, in the yz plane, it is possible to see its constant decay as the the distance from the connector, in which the field has its maximum, increases in figure 3.27. The effect of the resonator edges on

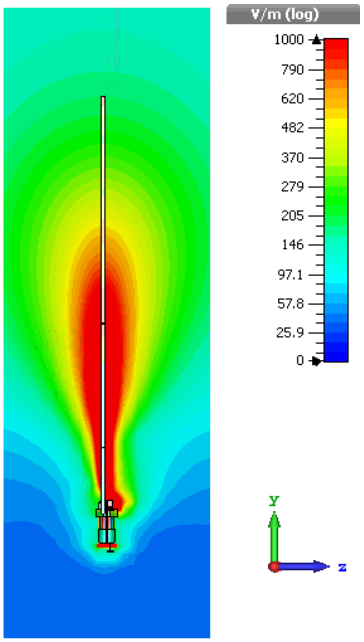

Figure 3.27: Designed Palm Tree Vivaldi antenna near electric field magnitude in the yz plane.

the electric field was also observed. According to the investigation presented in [20], the resonators act as a mean to confine the electric field. By confining the electric field near the edge slot resonators, as seen in figure 3.28, more intense surface currents are excited the resonator paths, therefore increasing the electric length of the antenna. The surface currents distribution can be seen in figure 3.29.

Finally, like previously done for the two aforementioned designs, the pulse distortion of the Palm Tree Vivaldi antenna was assessed. The same setup that was previously used, as seen in figure 3.13, is

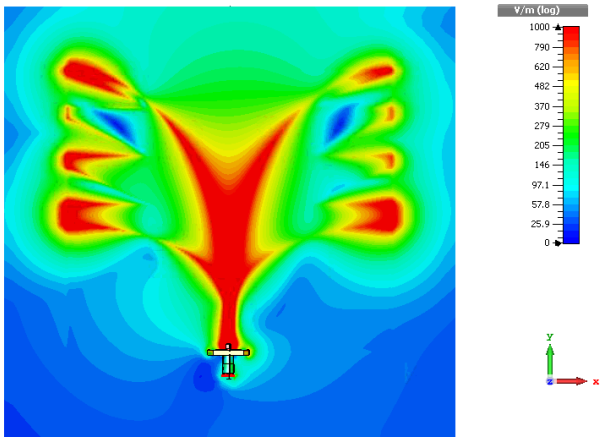

Figure 3.28: Designed Palm Tree Vivaldi antenna near electric field magnitude in the xy plane.

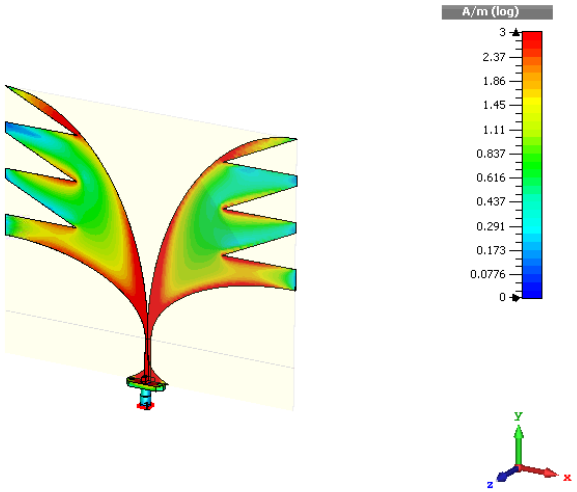

Figure 3.29: Designed Palm Tree Vivaldi antenna surface currents distribution magnitude.

applied, with the copper metal plane placed at 10 cm of the antenna. The received reflected pulse is barely afected, as seen in figure 3.30, therefore validating this parameter of the antenna.

At this stage of the text, the designed Palm Tree Vivaldi fulfills all the requirements needed for a Microwave Imaging System. Summarizing, the proposed design is a compact and thin structure, with its dimensions compiled in Table 3.3. This design illustrates that it's possible to miniaturize the dimensions of a Vivaldi antenna by adding edge slot resonators and, due to the electric field confining which leads to stronger surface currents in the resonator paths, the electrical length of the antenna is increased. By modifying the resonators' dimensions and geometries it is possible to adjust the desired bandwidth and its limits of operation, which fall in most of the desired 1-3 GHz band for intracranial Microwave Medical Imaging.

In section 3.2, the Palm Tree Vivaldi antenna production is discussed and the measured S_{11} parameter and pulse distortion are compared to the ones simulated in the present section of the text.

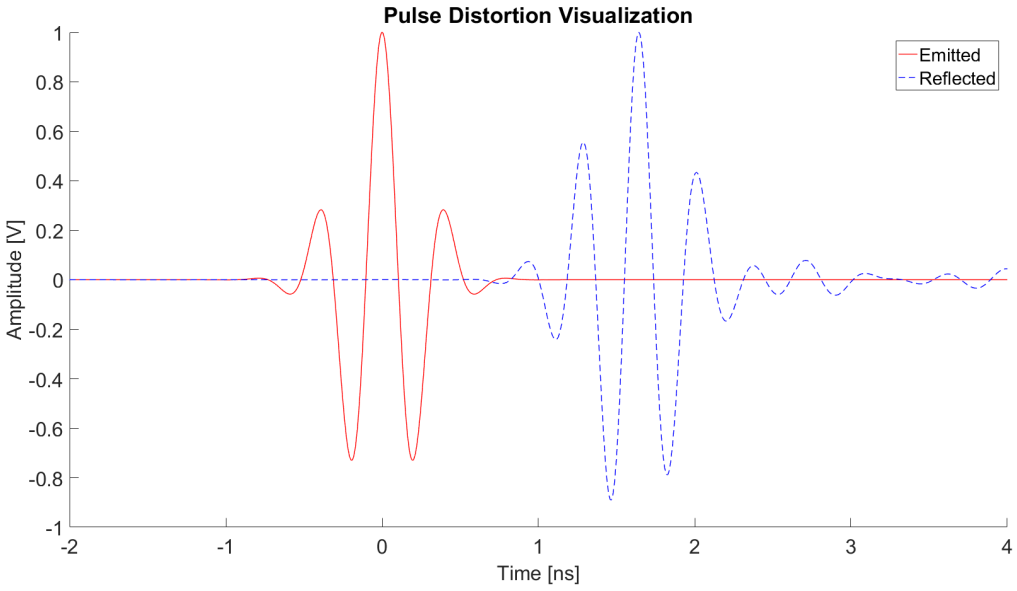

Figure 3.30: Synthesized emitted pulse (red) and reflected received pulse (dotted blue).

Table 3.4: Rogers RT/duroid 5880 substrate datasheet parameters

Substrate Properties	
Permittivity	ϵ_r = 2.20 $\pm$ 0.02
Dielectric Thickness	h = 0.79 mm
Cladding	h_{ant} = 0.0175 μm

3.2 Palm Tree Vivaldi Antenna Prototype and Testing

The production of printed circuits requires that the CST Studio Suite copper layers, both front and back ones, are exported to a Computer-Aided Design (CAD) software. In Appendix A, the Palm Tree Vivaldi antenna masks are presented, in which the front copper layers of the design are presented in black. The black rectangles and circle sections are placed in order to align both layers of the antenna. The black lines are meant to help the technician perform an accurate cut of the antenna's substrate. The substrate used for the antenna production, a Rogers RT/duroid 5880[27], has the properties compiled in Table 3.4. The substrate and both layers, printed on a highly transparent film material, are then exposed to ultraviolet rays, in which the copper metalization will be deposited on top of the substrate faces. At the end of the process, the SMA connector was welded to the feeding point of the antenna and the ground plane, as seen in figure 3.24.

The produced Palm Tree Vivaldi antenna is presented in figures 3.31 and 3.32, already welded to the SMA connector, also seen in the pictures. In order to evaluate if the produced antenna is behaving like the simulations presented in the previous section of the text, a free space measurement for the S_{11} parameter was performed in the Radiofrequency (RF) Laboratory of *Instituto de Telecomunicações*. A Vector Network Analyzer (VNA), a device in which RF signals' amplitude and phase can be measured, was used to perform this measurement. After calibrating the device and coaxial cable with a 50 Ω matched load in order to set the correct reference level for the S_{11} parameter, a frequency sweep ranging from 0.5 GHz to 6 GHz was done, yielding a total of 1101 samples. The S_{11} parameter of the Palm Tree

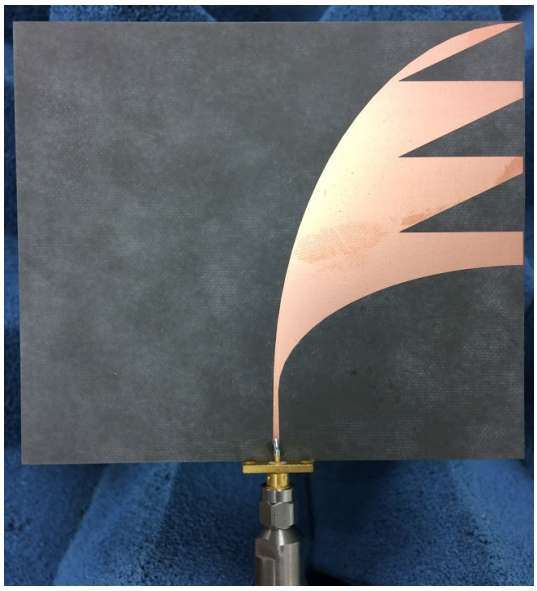

Figure 3.31: Produced Palm Tree Vivaldi antenna front view.

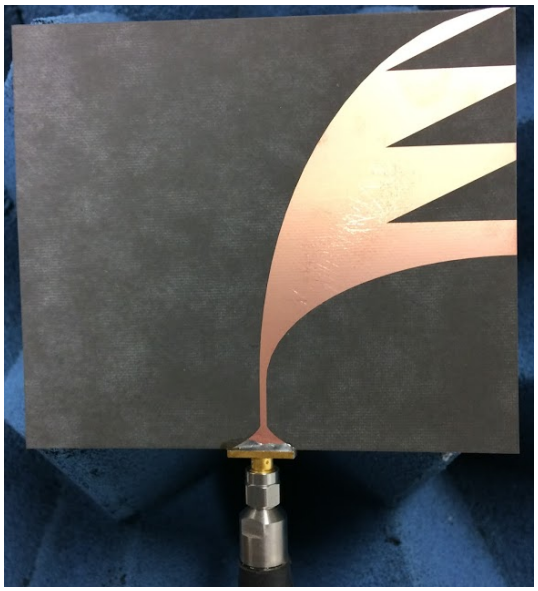

Figure 3.32: Produced Palm Tree Vivaldi antenna back view.

Vivaldi antenna was then plotted, in respect to the simulation present in figure 3.25, and can be seen in figure 3.33. The measured S_{11} parameter accurately matches the one obtained on CST Studio

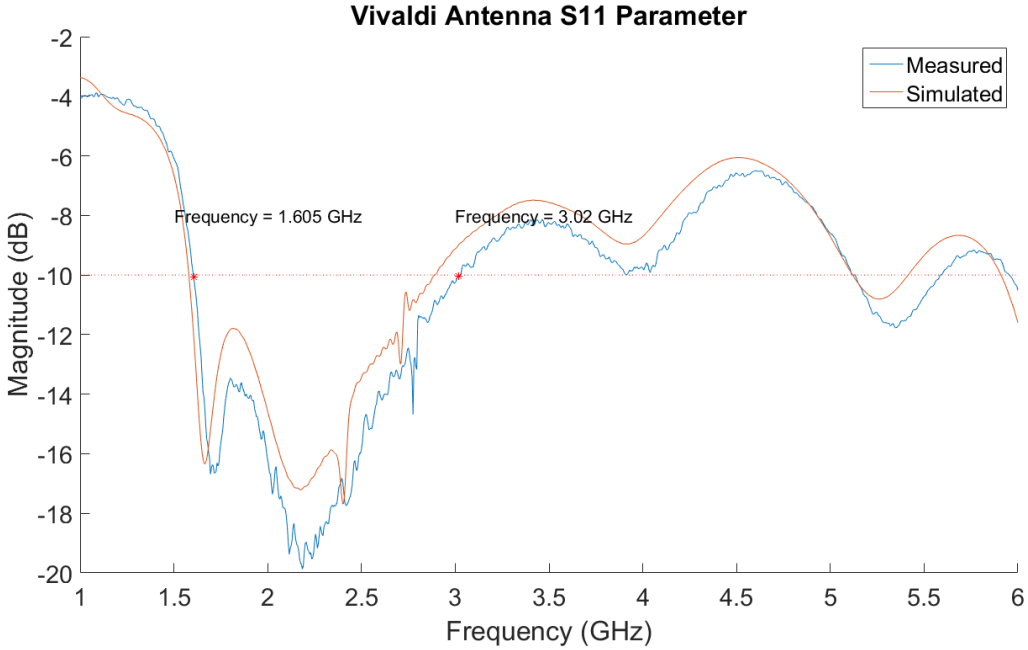

Figure 3.33: Produced and simulated Palm Tree Vivaldi antennas' S_{11}.

Suite and, while sharing approximately the same lower frequency of operation ($f_L = 1.602$ GHz in the produced antenna, 1.581 GHz in the simulated one), the bandwidth is increased due to the measured higher frequency of operation which is 3.02 GHz, opposed to the simulated 2.89 GHz. This increase may be explained by the additional thickness of substrate, which is known to increase bandwidth [25]. The produced Palm Tree Vivaldi antenna has a bandwidth of 1.415 GHz, centered at $f = 2.31$ GHz. With this information, the pulse distortion of the antenna was evaluated, by executing the measurement

Figure 3.34: S_{11} parameter measurement set-up with a copper plane.

set-up that was simulated and described in section 3.1. A large copper plane was placed, on the floor, with the Palm Tree Vivaldi antenna placed vertically above it, at a distance of 10 cm, as seen in figure 3.34. A wood support was used to keep the antenna at a constant height above the plane, while it was hold by a tripod. Radiation-absorvent material was used to avoid reflections from the metal cabinet that was near the set-up. The coaxial cable was connected to the VNA and, after its calibration, the S_{11} parameter was measured. The S_{11} parameter for this situation was measured and the aforementioned process was replicated, by applying the equations 3.10 to 3.13. The measured reflected signal is plotted in figure 3.35, with the simulated pulse also present for comparison. The measured reflected signal (dotted blue) is slighty in advance in relation to the simulated one (dotted cyan), although the antenna still introduces some signal distortion, keeping the peak and shape clearly detectable as it is intended.

The prototyping of the Palm Tree Vivaldi antenna concludes Chapter 3. Summarizing, in this Chapter, a base model for the Vivaldi antenna was defined, with its geometry being parametrized and properties defined. Given the requirements needed for a microwave imaging system, the base model of the Vivaldi antenna was re-shaped, namely in the feeding structure and dimensions, in order to reach the desired frequency band of operation and required bandwidth. The introduction of the resonators allowed the obtention of the Palm Tree design in which the antenna could be miniaturized, while also preserving its bandwidth. Using this strategy, the lowest frequency of operation of the antenna also shifted towards the desired 1 GHz. The resonators effect on the miniaturized Palm Tree Vivaldi antenna was studied, namely the electric fields confinement in the resonators, and the final design was obtained. This design was then prototyped and the produced antenna behaves as expected from the simulations, with a slight

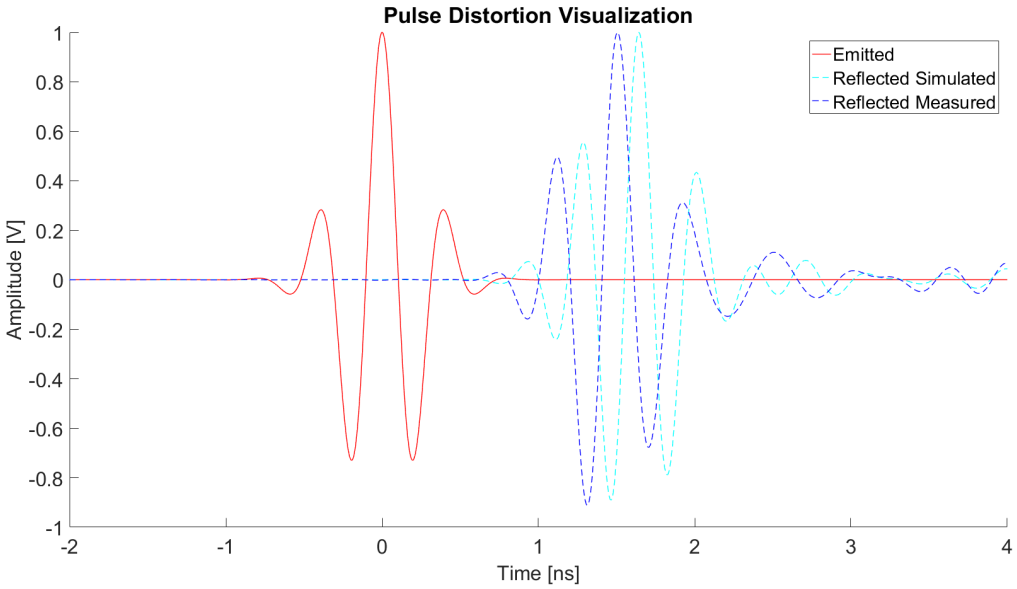

Figure 3.35: Synthesized emitted pulse (red), reflected simulated received pulse (dotted cyan) and reflected measured received pulse (dotted blue).

performance increase.

Chapter 4

Image Reconstruction Algorithm

In the present Chapter of the text, the developed image reconstuction algorithm is presented and the assumptions made are explained. The algorithm is divided in 4 steps, which are fully detailed throughout the Chapter. Later, the algorithm is tested in scenarios with different complexities, based on CST Studio Suite simulations. Finally, the results obtained with a measurement set-up are presented and discussed.

4.1 Image Reconstruction Algorithm Development

There are several techniques that aim at solving the image reconstruction inverse problem present in Microwave Imaging Systems. The Delay And Sum (DAS) is the chosen algorithm to be applied and developed in this Thesis. It is a time domain algorithm, which operates on the reflected signals from a scanning target [2]. Due to its nature, it is a simple and intuitive algorithm to be understood and developed.

4.1.1 Delay and Sum Algorithm

The DAS algorithm uses a monostatic radar approach [3], in which the signal is emitted and, should a target exist, is reflected back to the same antenna. This can be illustrated in figure 4.1. Since the DAS is a time domain algorithm, it is crucial to compute the delay between the emitted and reflected pulse. In this example, considering that the target (marked in yellow) and the antenna are fixed, the distance between both is the same, so

$$d_1 = d_2 \tag{4.1}$$

in which d_1 is the distance travelled by the emitted pulse and d_2 is the distance travelled by the reflected signal. The total travelling time can be computed by taking into account the propagation medium permittivity, ϵ_r, as seen in expression 4.2

$$t = \frac{(d_1 + d_2) \times \sqrt{\epsilon_r}}{c} \tag{4.2}$$

In order to accurately detect the reflected impulse, expression 4.2 must be modified by adding an equivalent distance, d_{ant}, which accounts for the propagation delay between the antenna's feeding point and a reference point, considered to be on the center of the substrate edge further away from the feeding point (green mark on the antenna, figure 4.1). So, by rearranging the previous equation, including the

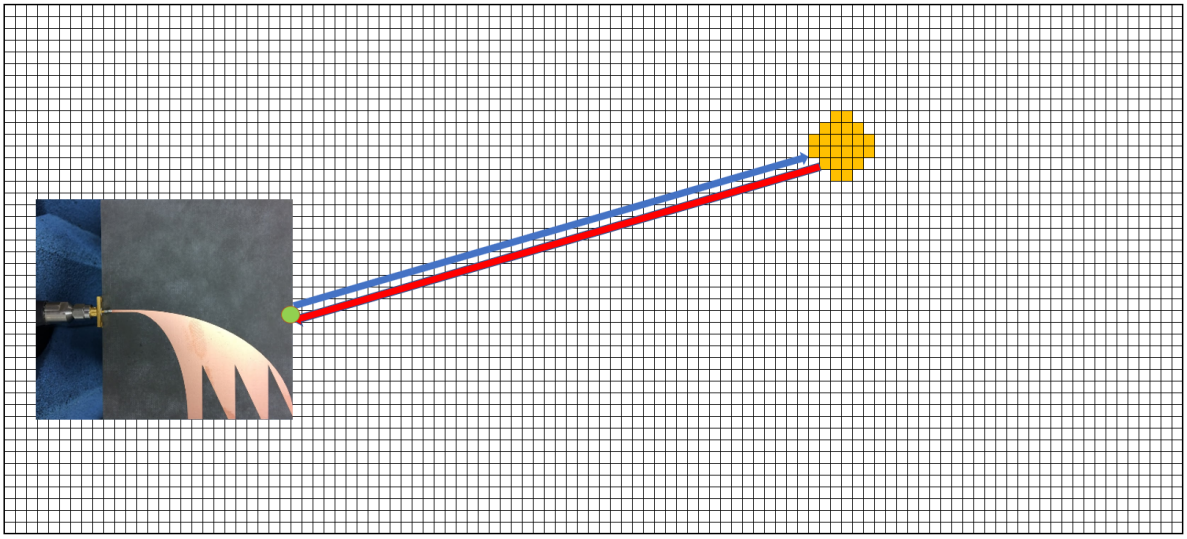

Figure 4.1: Monostatic radar approach for the DAS algorithm.

d_{ant} term, expression 4.3 is obtained in order to provide the total propagation time of a signal emitted from the antenna travelling to a target, and back to antenna.

$$t = \frac{(d_1 + d_2) \times \sqrt{\epsilon_r} + d_{ant}}{c} \tag{4.3}$$

Using the S_{11} parameter measurements with the copper plane, placed at 10 cm away from the antenna, as seen in section 3.2, the reflected signal is received at $t = 1.5042$ ns. This value is obtained using a Matlab peak detection function which returns the peak value and its occurence index, therefore allowing to obtain the time of occurence, as seen in figure 4.2. Knowing this time instant, it is possible to modify expression 4.3 to obtain the d_{ant} value,

$$d_{ant} = ct - (d_1 + d_2)\sqrt{\epsilon_r} \tag{4.4}$$

yielding $d_{ant} = 0.25126$ m, considering $\epsilon_r = 1$, since the measurements were performed in the air. Being able to accurately detect the peak ocurrence times is crucial for the DAS algorithm. The DAS algorithm has an iterative procedure, in which the distances from the antenna reference point, (x, y), (marked in green in figure 4.1), are computed for every point in the grid, (a_i, b_j), by expression 4.5

$$d = \sqrt{(x - a_i)^2 + (y - b_j)^2} \tag{4.5}$$

and, since $d_1 = d_2$ and knowing d_{ant}, the total propagation time to every point in the grid can be computed using expression 4.3. With this information on the propagation time, the signal delays are

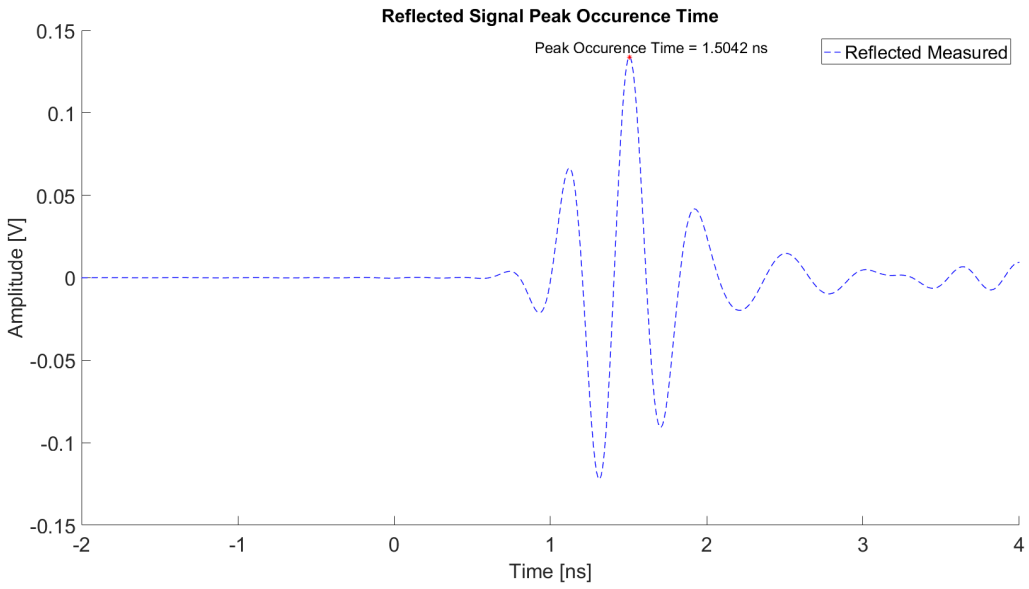

Figure 4.2: Palm Tree Vivaldi antenna peak occurence time.

computed and the amplitude for each time instant can be stored in each (a_i, b_j) point of the grid. All the (a_i, b_j) points that are at the same distance of the target form a circunference that shares the amplitude value of the peak, while the other points are expected to have smaller amplitude values. Therefore, by colour mapping the amplitude values of the grid, it is expected that a region where the the detection of a reflective target occurs is present. This assumption is illustrated in figure 4.3.

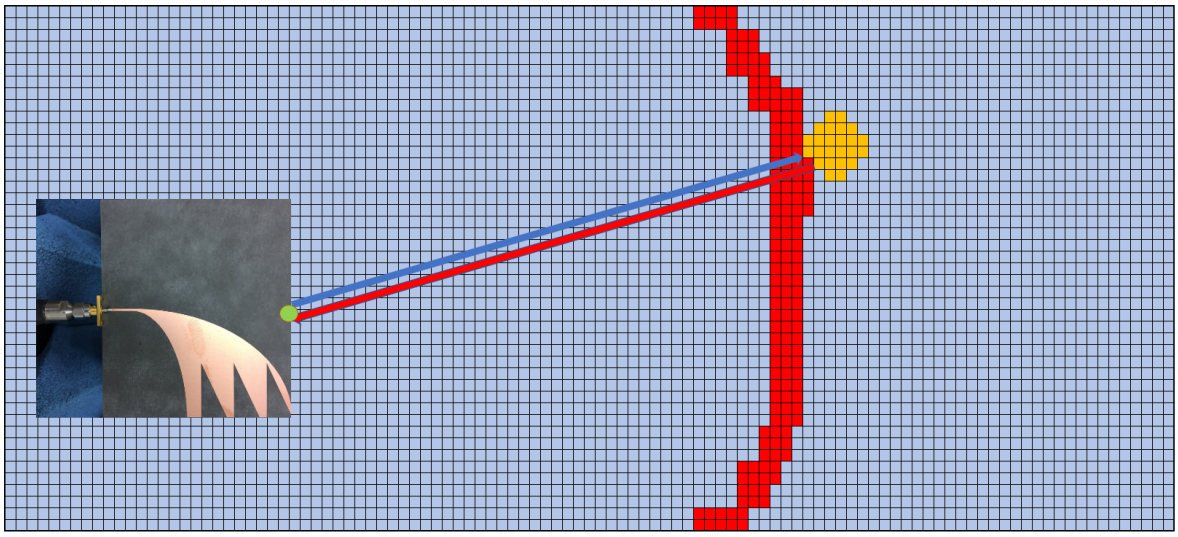

Figure 4.3: DAS detection illustration for 1 antenna.

The approach discussed above allows to detect a target by analyzing its reflection peak occurence time, however it creates a circumference around the antenna where it may be localized. Therefore, in order to make an accurate detection, more antennas are used in the scanning process. In this Thesis, due to the antenna and human head dimensions, a total of 8 antennas are considered for scans. Their disposition forms a circular scanning array, as illustrated in figure 4.4. With the proposed scanning array,

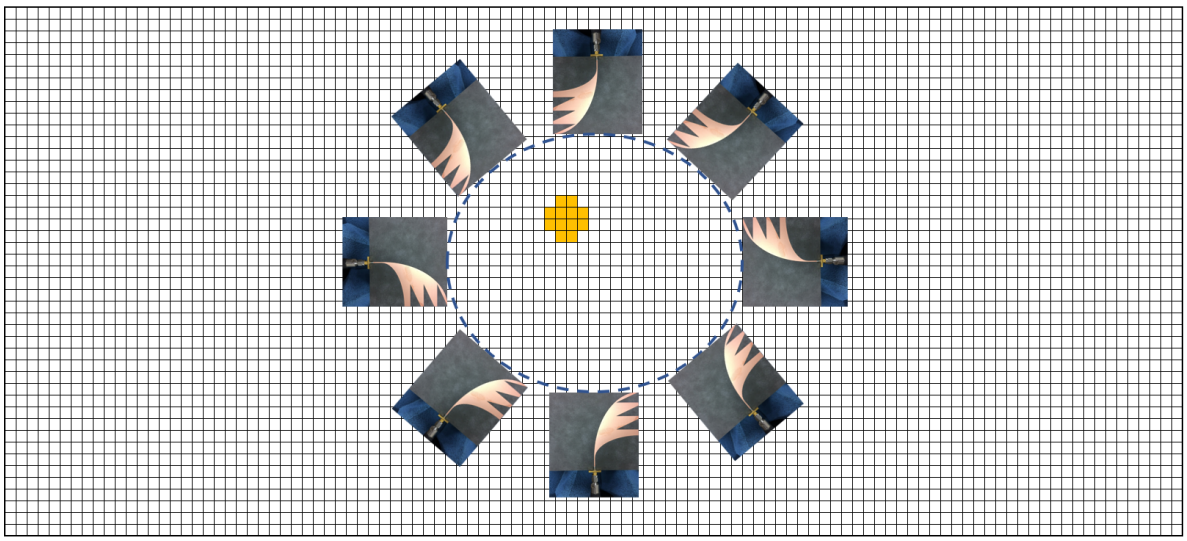

Figure 4.4: Proposed circular Palm Tree Vivaldi antennas scanning array.

it is expected that all antennas detect the target individually, each creating a circumference with its radius equal to the computed distance which yields the peak occurrence time. Then, proceding as discussed above, for each antenna there is an amplitude value assigned to each (a_i, b_j) point on the grid. Then, the amplitude values are summed at every (a_i, b_j) point, for the 8 antennas, resulting in a matrix that can be colour mapped. While, individually, the circumferences for each antenna appear, like in figure 4.3, the sum results in a small region of the grid having clearly a greater amplitude value than the others, which is the region where the circumferences intersect. The other zones will have different amplitude values, depending on the number of circumferences that intersect there and the peaks' amplitudes themselves, which is seen in figure 4.5. This concludes the DAS procedure, in which a grid is colour mapped with an example, in which a target is marked as a blue circle, using the scanning array in figure 4.4.

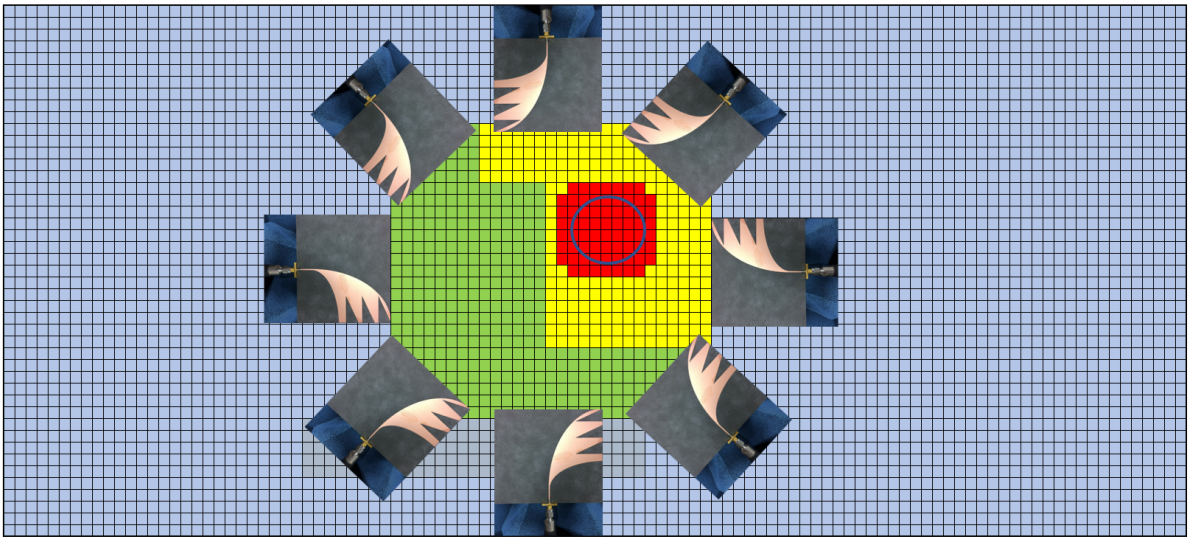

Figure 4.5: DAS detection illustration for 8 antennas.

4.1.2 Delay and Sum Simulations in the Air

In order to demonstrate the DAS algorithm, a simulation set-up was produced in CST Studio Suite. The Hexahedral TLM mode, with an accuracy of -50 dB was used. Due to limitations with the waveguide port definition in this meshing mode, which only allows axis symmetries thus limiting the set-up to 4 antennas, a different approach was used. Only 1 antenna was placed in the simulation environment, and the target was rotated in intervals of

$$\Delta\theta = \frac{360^\circ}{N} = 45^\circ \tag{4.6}$$

with N = 8 being the number of antennas used in the simulation. Using this scheme, only one antenna is present and all the targets are considered for meshing purposes, but only one is considered for simulation. This way, simulating a rotating target is equivalent to simulating a fixed target, but a moving antenna with a negative $\Delta\theta$ angle. The simulation model, as seen in CST Studio Suite, is present in figure 4.6. A copper ellipse target was placed, at coordinates $(x, y) = (-30, -20)$ mm, with radius along

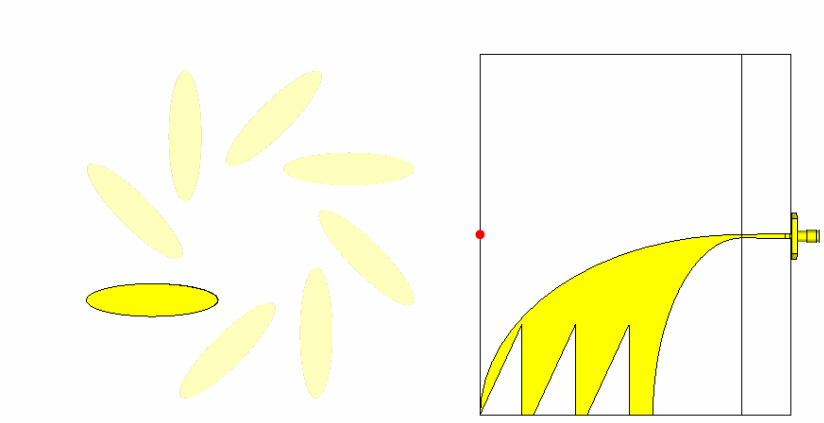

Figure 4.6: CST Studio Suite simulation model.

the xx axis equal to 20 mm and along the yy axis equal to 5 mm. In this situation $\Delta\theta = 360^\circ = 0^\circ$ and, by creating a rotated copy of the target around the origin, every 45°, a simulated rotation of the antenna is made for the negative angle of the rotation. The S_{11} parameter was measured in free space for calibration purposes, followed by a measure of the S_{11} parameter for all the 8 positions of the anomaly, in the frequency range of 1-6 GHz. The antenna was placed 7 cm away from the origin, along the xx axis, with its reference point having the coordinates $(x, y) = (70, 0)$ mm. The targets are 1 cm high, with the antenna being placed in plane that equals half the target's height. Copper was the material chosen for the targets since, by being a metal, allows maximum reflection of an incident planar wave.

In Matlab, a grid was defined as the scanning region. Since the antennas form a circular array with radius of 7 cm, the grid was defined from -10 to 10 cm, in the xx and yy dimensions. The antennas are located at the circle marks and are numbered. The location of the target and the origin are also present, in a dashed red line and in a blue cross, respectively. The scanning grid is shown in figure 4.7. The S1P files produced by CST Studio Suite were then imported to Matlab and the 8 reflected signals

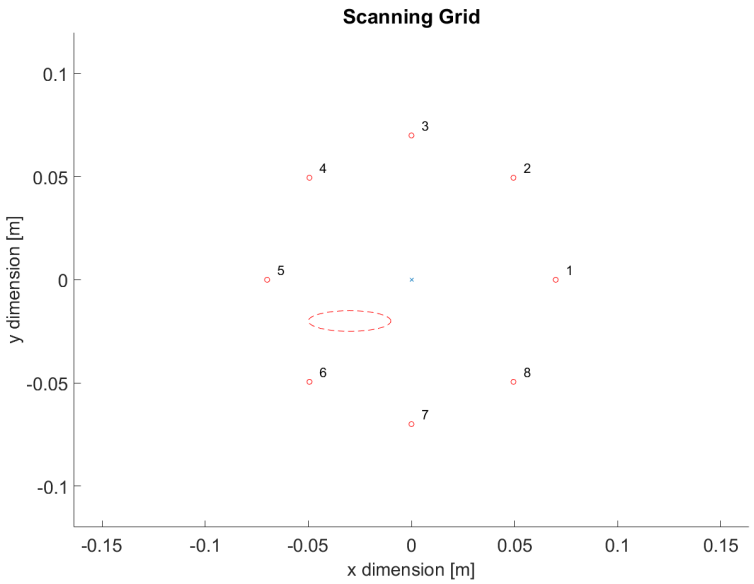

Figure 4.7: Scanning grid, as seen in Matlab.

were synthesized, with the process described in section 3.1.1. They can be seen in figure 4.8. Having

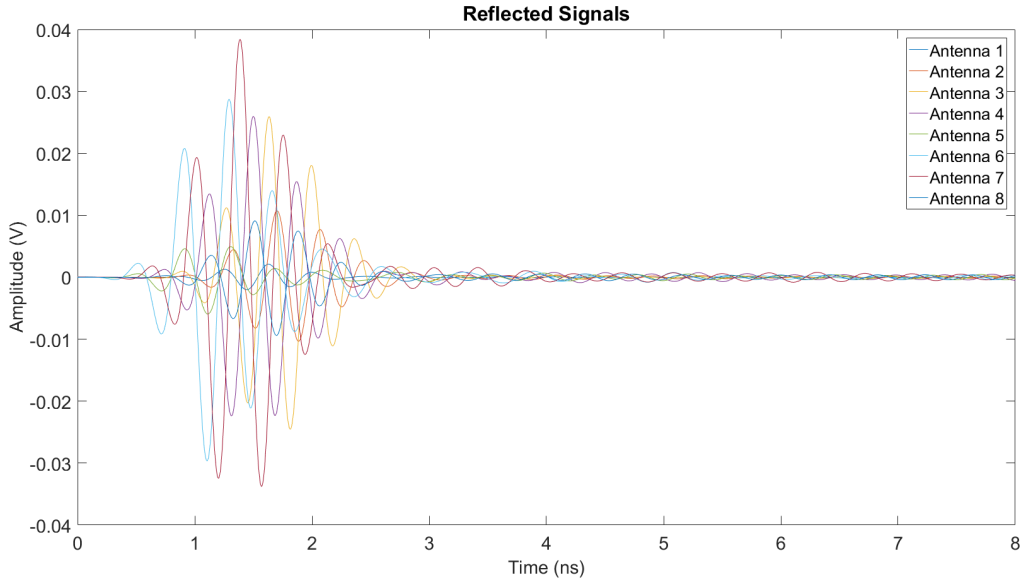

Figure 4.8: Reflected signals for each antenna position.

all the reflected signals, the DAS procedure was then coded. The coordinates of the 8 antennas are known, as well as the coordinates of each entry of the scanning grid. The scanning grid consists of two linearly spaced vectors (for the xx and yy dimensions), with 100 values, between -0.1 and 0.1 m. The euclidean distance from each antenna to every point of the grid is computed, using expression 4.5, and the total propagation time is computed using expression 4.3. A query to the time values vector is performed, yielding the closest value to the one that was computed, allowing to get an amplitude value for the corresponding point in the grid. The process is then repeated for all the points in the scanning grid and, after that, for every antenna. Finally, the scanning grid is colour mapped into a pixelized image.

This process is described, in pseudocode, below:

while *Antenna position* $\leq$ *number of antennas* **do**

  while *Not all scanning grid positions are considered for one antenna* **do**

    Compute euclidean distance to each grid position;

    Compute total propagation time;

    Get amplitude value for the computed propagation time;

  end

  Sum with the previously obtained amplitude values;

end

Colour map the summed grids into a pixelized image;

Applying this procedure allows to obtain, for each antenna, images that confirm the assumption made earlier in the text, and shown in figure 4.3. Below, in figures 4.9 and 4.10, it is seen the colour mapping, developed in Matlab, for the antennas in position 1 and 5. These two images clearly show the circumferences with radius equal to the distance determined by the the peak occurence time in the reflected signals present in figure 4.8. Depending on the propagation distance, the amplitudes obtained for the peak also vary, obviously being higher the closer the target is to the antenna, as the signal is attenuated with an increasing travelling distance. The final colour mapping is computed on top of the

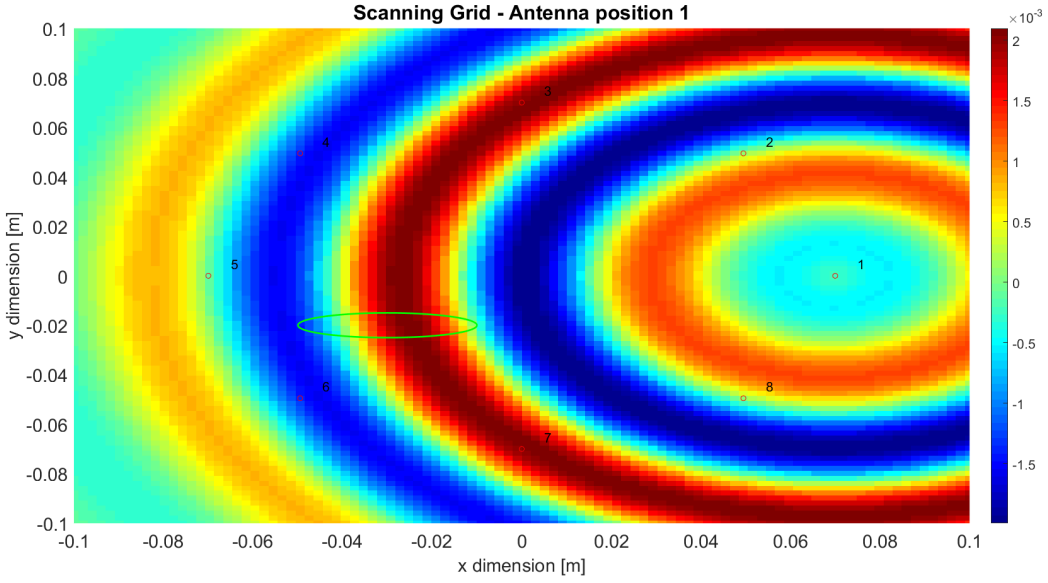

Figure 4.9: DAS detection as seen in Matlab, for the antenna in position 1.

summed grids, a process we can generalize with expression 4.7,

$$I(x,y) = \sum_{pos=1}^{N} g(pos) \tag{4.7}$$

with $I(x,y)$ the image produced with the sum of the grids, $g(pos)$, for all the N antennas. The grid,

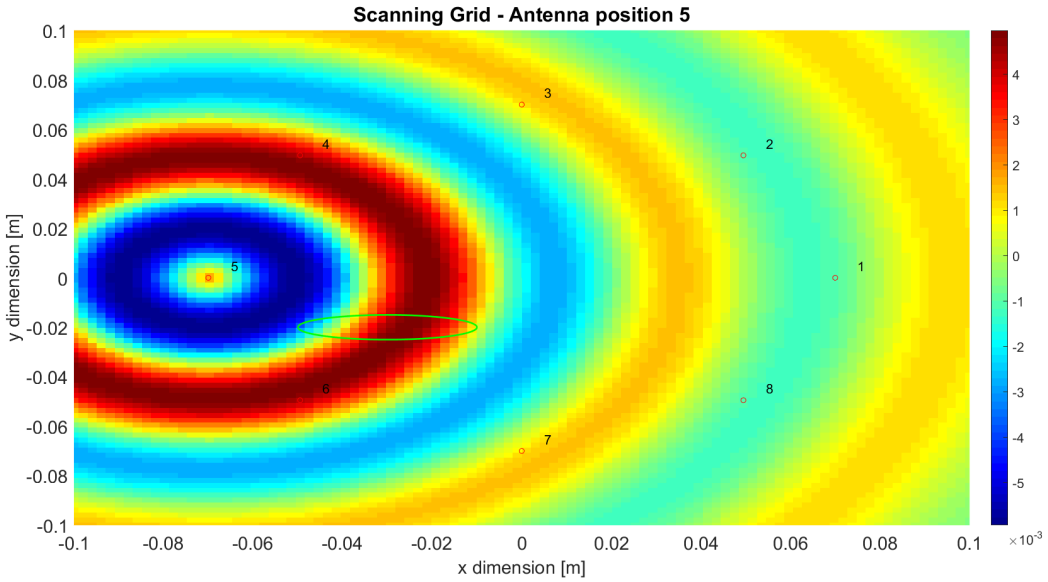

Figure 4.10: DAS detection as seen in Matlab, for the antenna in position 5.

$g(pos)$, is defined as

$$g(pos) = \begin{bmatrix} a_1b_1 & a_1b_2 & ... & a_1b_j \\ a_2b_1 & ... & ... & ... \\ ... & ... & ... & a_{i-1}b_j \\ a_ib_1 & ... & a_ib_{j-1} & a_ib_j \end{bmatrix}$$

with each (a_i, b_j) pair denoting the amplitude value obtained for those coordinates in the euclidean space. Its value in the $g(pos)$ matrix is obtained by computing expression 4.8,

$$a_ib_j = y_r(t) \tag{4.8}$$

$y_r(t)$ being the reflected signal for the antenna in analysis, and t obtained with expression 4.9,

$$t = \frac{d_{ant} + 2\sqrt{(x-a_i)^2 + (y-b_j)^2}}{c} \tag{4.9}$$

with the permittivity, ϵ_r, being 1 in the air, therefore being omitted in the expression. Following this procedure, it is possible to reconstruct the scanning area with the target being clearly highlighted. Due to the nature of microwaves in this frequency range, the resolution of the produced images is sacrificed. Therefore, it is not expected that the shape or exact dimensions of the target are determined, but rather if an anomaly is present in the scanning region or not. Below, in figure 4.11, the reconstructed image, obtained using Matlab, is presented. It is clear that the target is well located, as seen by the red and orange colours, representing the higher values of signal amplitude. The negative components of the signal were chopped and replaced with zeros. This post processing artifact is used in order to remove ghosts and other incorrect target detections. It is still clear, in this image, that the peak amplitude circumferences are still present, namely by the green colours that are visible. Clearly, they all intersect in

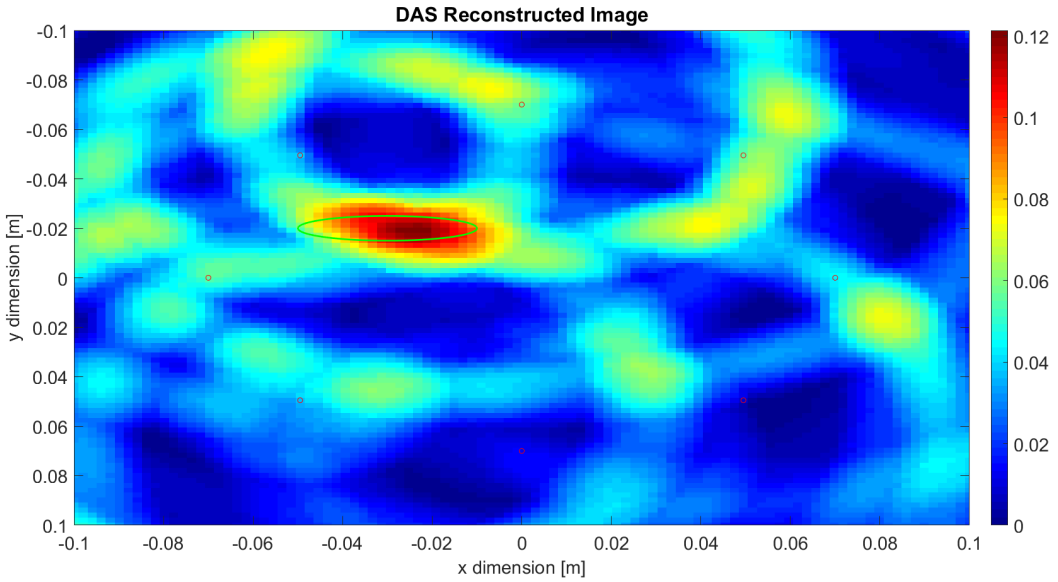

Figure 4.11: DAS image reconstruction for a copper target, in the air.

the target region, thus creating the higher sum of amplitudes leading to the red and orange colours. Another way of presenting the reconstructed image is by, instead of simply showing the summed amplitudes, colour mapping the squared value of the summed amplitudes. At the cost of focusing the detection around the center of the target, thus leading to a loss in the visualization of the dimensions of the object, this form of representation allows to make a more clear highlight of the target detection. The DAS reconstructed image, using this approach, is seen in figure 4.12. It is clear that squared value

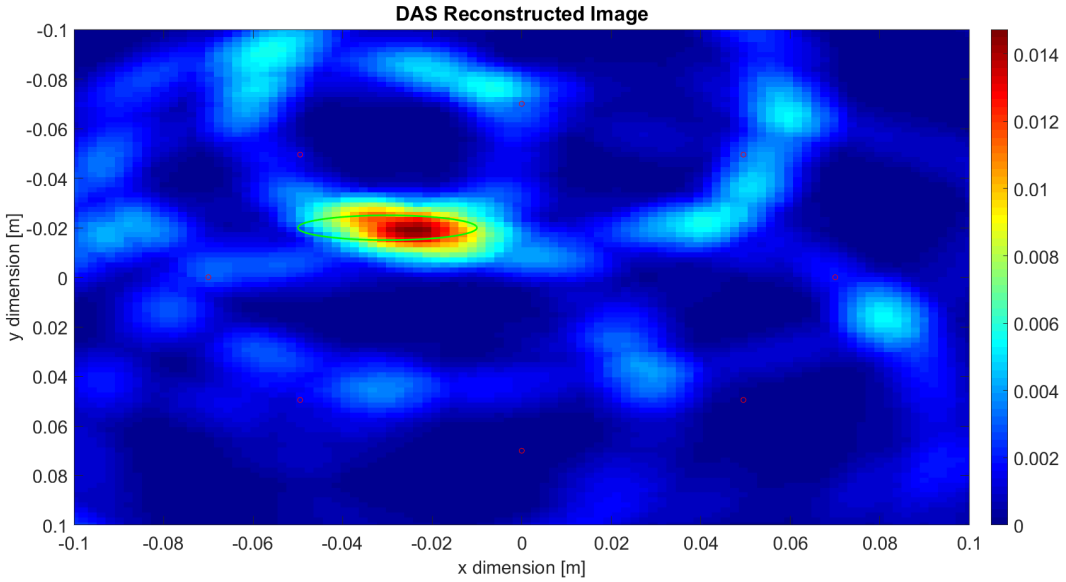

Figure 4.12: DAS image reconstruction for a copper target, in the air, with squared values of the amplitudes.

of the summed amplitudes provides greater clarity in correctly detecting the existence of a target and highlighting its shape and approximate dimensions.

This concludes the demonstration of the DAS algorithm in the air, working as a monostatic radar where the detections from different antennas are used to show the target location in a 2D plane, instead of simply providing information on the distance the target is from the antenna. In section 4.1.3, the DAS algorithm is modified to account a more complex propagation medium, in which the antennas must detect an anomaly inside a human head model.

4.1.3 Delay and Sum Simulations with a Human Head Model

The previous section showed that the DAS algorithm can be used to provide an image of a scanning area using a known disposition of the antennas. In this section, the developed algorithm is further improved in order to account a more complex propagation medium. In fact, while previously the propagation time was computed using a simple expression, three different propagation media must be considered in a human head scan. The antenna radiates in the air, $\epsilon_r = 1$, but a dielectric boundary exists between the air and the skin/bone. Due to its thickness, averaging 6.32 mm in adult humans [29], and higher permittivity, $\epsilon_r = 11$, only the bone is considered for the first boundary. Then, the signal has to propagate through the brain, which is considered uniform, as a simplifying approximation, with permittivity $\epsilon_r = 49$. The propagation model for this situation is illustrated in figure 4.13. The rational behind the DAS

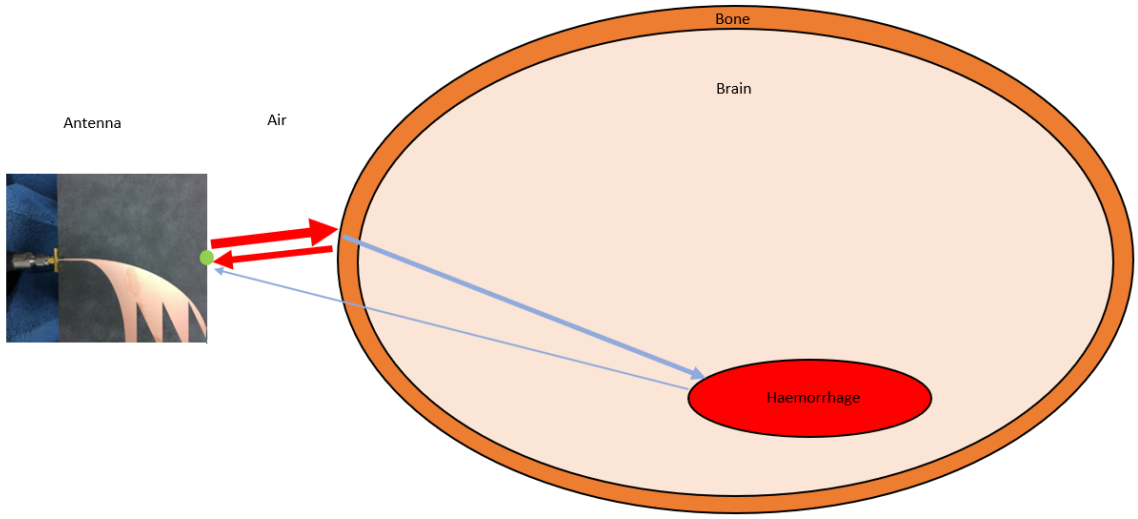

Figure 4.13: Human Head propagation model.

algorithm in this situation is that there is a strong reflection in the first dielectric boundary, between the air and the bone. When this reflection occurs between two dielectric media, there is also a portion of the incident wave that is transmitted inside the second dielectric, but greatly attenuated. This transmitted wave will then be reflected by another dielectric boundary, in this case the brain/haemorrhage boundary, where a great dielectric contrast is present. This reflection, with amplitude values several orders of magnitude below the reflection seen in the air/bone interface, is crucial to reconstruct an image of the inside of a human head. Recovering this signal is main difficulty of the image reconstruction step

in microwave imaging. In the first place, a CST Studio Suite was developed, in order to detect a water anomaly inside two dielectrics, with an elliptical shape, with permittivites $\epsilon_r = 11$ and $\epsilon_r = 49$, simulating bone and brain, respectively. The simulated CST Studio model can be seen in figure 4.14. The model

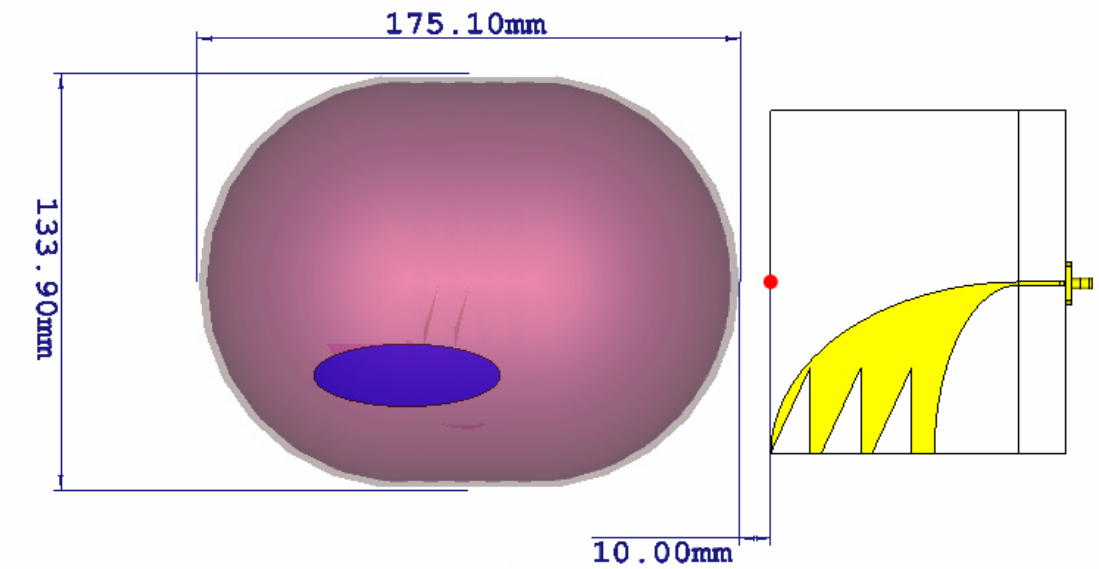

Figure 4.14: Simulation set-up, as seen in CST Studio Suite, with Human Head model and water anomaly.

was, like previously discussed in the beginning of the previous section, rotated 8 times, $45°$ per rotation, in order to simulate the presence of 8 antennas. The chosen dimensions for the model are typical for an adult human, with 6.32 mm being the considered bone thickness. The model for the bone consisted of a carved shape, with the brain model shape inside. The bone was simulated with permittivity $\epsilon_r = 11$ and loss tangent, $tan(\delta) = 0.256$. The brain was simulated with permittivity $\epsilon_r = 49$ and loss tangent $tan(\delta) = 0.271$. The antenna, on its closest point to the head, was placed 1 cm away from the model. The anomaly consisted of a water elliptical cilinder, placed at coordinates $(x, y) = (-20, -30)$ mm, with radius in the xx dimension of 30 mm and in the yy dimension 10 mm. Since water has a permittivity of around $\epsilon_r = 81$ (the blood has permittivity $\epsilon_r = 58$), this was the material chosen to be used in the produced phantom, therefore it was also used in the simulations. It was simulated with a conductivity of $\sigma = 1.59$ S/m. The CST Studio Suite Hexahedral TLM mode was used in the Time Domain Solver to obtain the S_{11} parameters, in free space for calibration purposes, and with the head model present, like in the previous section.

The S1P files produced by CST Studio Suite were imported to Matlab to initialize the image reconstruction process. These files contain a number of frequency samples, each corresponding to a certain S_{11} value. Like in the previous section, a scanning grid was defined. With the antennas disposed, once again, in a circular array, with radius 9.7 cm, it is possible to illustrate the scanning scheme in figure 4.15. Using the aforementioned process to synthesize the reflected signals for each of the 8 antennas, it is possible to illustrate them, in figure 4.16. As described above, all signals have strong reflections coming from the air/bone dielectric boundary, hence all reflected signals having a similar pulse shape and peak occurence time, as predicted on the propagation model from figure 4.13. The reflected signals

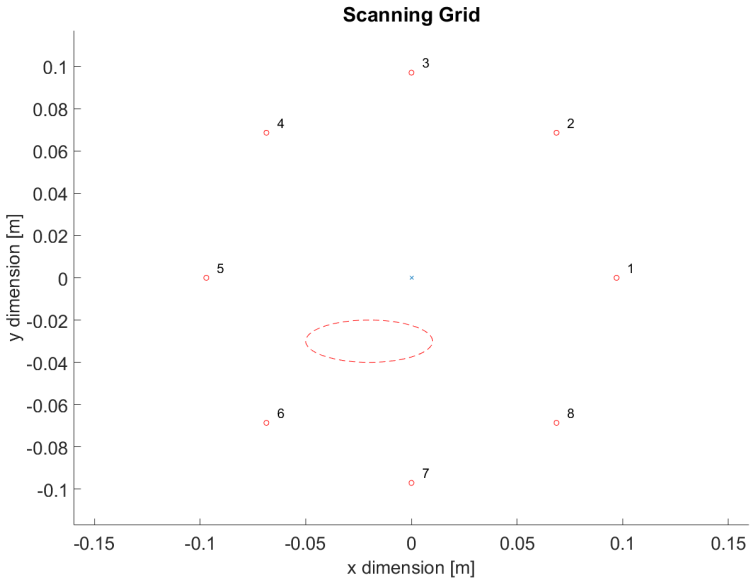

Figure 4.15: Scanning grid, as seen in Matlab.

coming from the anomaly are several orders of magnitude weaker than these reflections, thus requiring an artifact removal technique to be used in order to recover the correct anomaly reflected pulse. In order

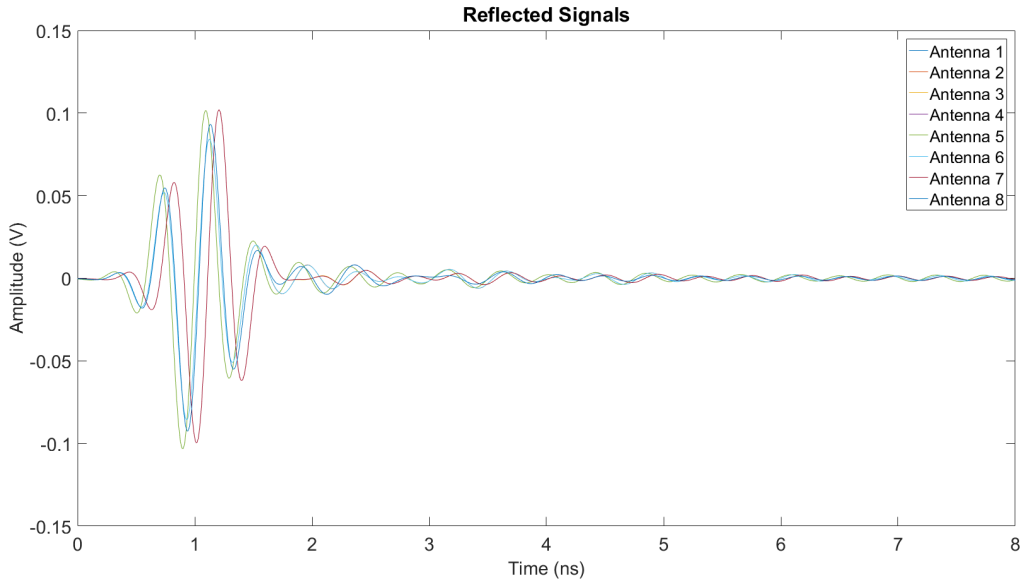

Figure 4.16: Reflected signals for each antenna.

to recover the anomaly reflection, the first step is the artifact removal of the air/bone reflection. This process is the calibration of the reflections, taking advantage of the symmetries in the human skull. In fact, the use of 8 antennas allows to mark pairs of positions that are approximately symmetric to eachother, in relation to the defined axis, as seen in figure 4.17. The circles that have the same colour are symmetric to eachother, and shall be used in the calibrations. The calibration method used in this work uses the signals that are further away from the anomaly. While sharing roughly the same reflection from the air/bone dielectric boundary, the reflection from the anomaly is expected to be much more detectable the closer

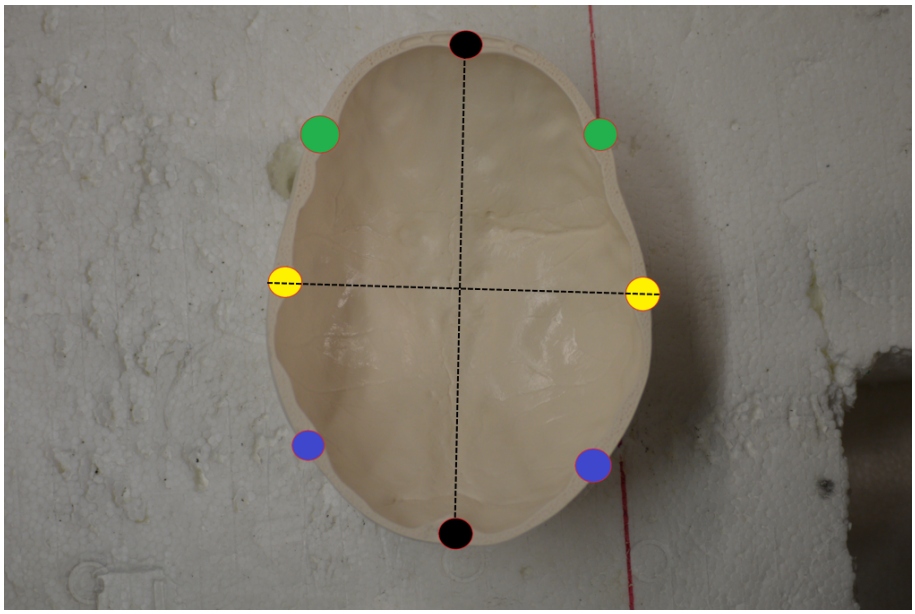

Figure 4.17: Symmetries in the human skull, as seen in a real scale model.

the antenna is from the anomaly. In order to do this, the following instructions were coded in Matlab:

Define furthest antennas from the anomaly;

Define calibration signals for every reflected signals;

while *Antenna position* $\leq$ *number of antennas* **do**

  Detect peak occurrence time;

  Align reflected signal to its calibration signal;

  Subtract the reflected signal to its aligned calibration signal;

end

Obtain calibrated reflected signals for all antennas;

After this process, the signals for each antenna position are subtracted in relation to its symmetric signal. For instance, the signals that share the same colour, in figure 4.17, are taken into account for this calibration and are subtracted to each other. The same symmetry approach was used to the developed model from figure 4.14. As seen in the scanning grid, from figure 4.15, the antenna in position 6 is expected to provide the reflection from the anomaly with the highest amplitude, with the antenna in position 2 providing a signal with roughly the same reflection from the air/bone interface, but not from the anomaly. Therefore, the anomaly reflection signal from antenna in position 6 is obtained by subtracting the calibrated signal from antenna in position 6 to the one from antenna in position 2. This results in the signal from figure 4.18. By performing a peak analysis on both reflections, it is clear that, while the air/bone reflection occurs, for antenna in position 6, at $t = 1.125$ ns, for a peak amplitude of 0.084 V, the anomaly reflection occurs at $t = 1.904$ ns, for a peak amplitude value of 1.799×10^{-4} V. In order to measure the the magnitude of the reflections from both interfaces, the aforementioned values can be used in expression 4.10,

$$\Delta peak = 20log\frac{Air/Bone}{Brain/Anomaly} \tag{4.10}$$

which concludes that the reflection peak amplitude from the anomaly is 53.38 dB below the peak from

the air/bone interface, thus making these signals very hard to detect, as expected.

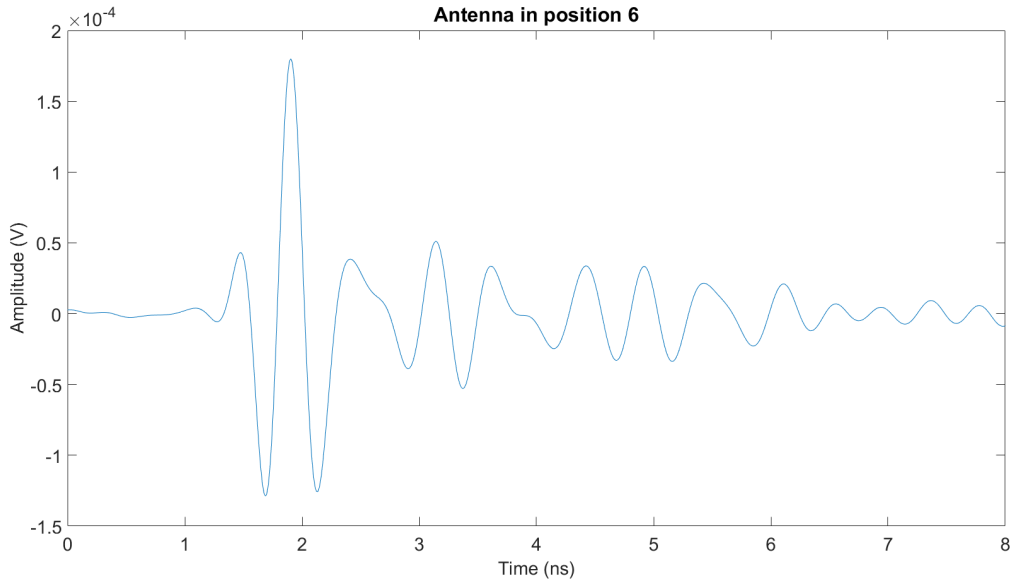

Figure 4.18: Water anomaly reflected signal, received at the antenna in position 6.

Generalizing, the calibration process may be described mathematically, for each antenna as,

$$u_{cal}(t) = y_r^*(t - \Delta t) \tag{4.11}$$

$$y_{cal}(t) = y_r(t) - u_{cal}(t) \tag{4.12}$$

with expression 4.11 denoting the alignement of the reflected signals further away from the anomaly (y_r^* in the notation) and expression 4.12 referring to the subtraction of the reflected signals from the air/bone boundary (figure 4.8) with the calibration signals. Finally, the subtractions of the symmetric signals can be described by expression 4.13,

$$y_i(t) = \begin{cases} y_i(t) - y_{i+N/2}(t) & i \leq N/2 \\ y_i(t) - y_{i-N/2}(t) & otherwise \end{cases} \tag{4.13}$$

for N an even number of antennas in the scanning array.

This process of detecting the anomaly reflections produces signals that are in phase opposition according to the conditions of expression 4.13, as seen in figure 4.19. In order to eliminate this behaviour, a peak amplitude comparison is performed between the two considered signals. The signal with the maximum peak amplitude is considered to be the closest to the anomaly, while the other signal is modified in order to not produce ghost images. The peak occurrence time is obtained for the closest antenna to the anomaly, and the other signal amplitude values are replaced with zeros until the peak occurence time, t_p with the impulse width, τ, according to expression 4.14. The modified signal is shown in figure 4.20.

$$y^*(t) = \begin{cases} 0 & t \leq t_p + \tau \\ y^*(t) & t > t_p + \tau \end{cases} \tag{4.14}$$

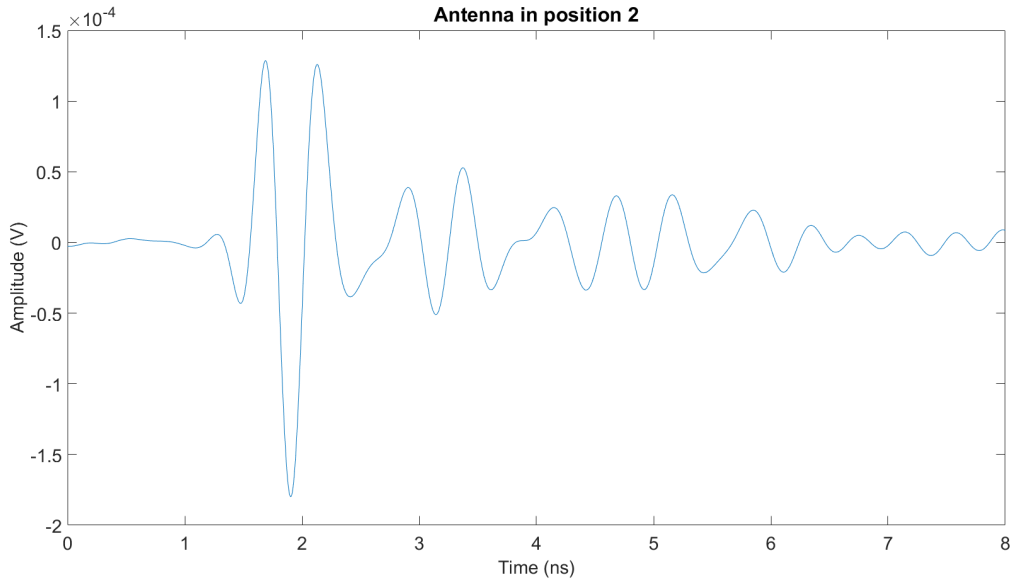

Figure 4.19: Water anomaly reflected signal, received at the antenna in position 2.

With the anomaly being detected on the 8 antennas, the image reconstruction may take place. However,

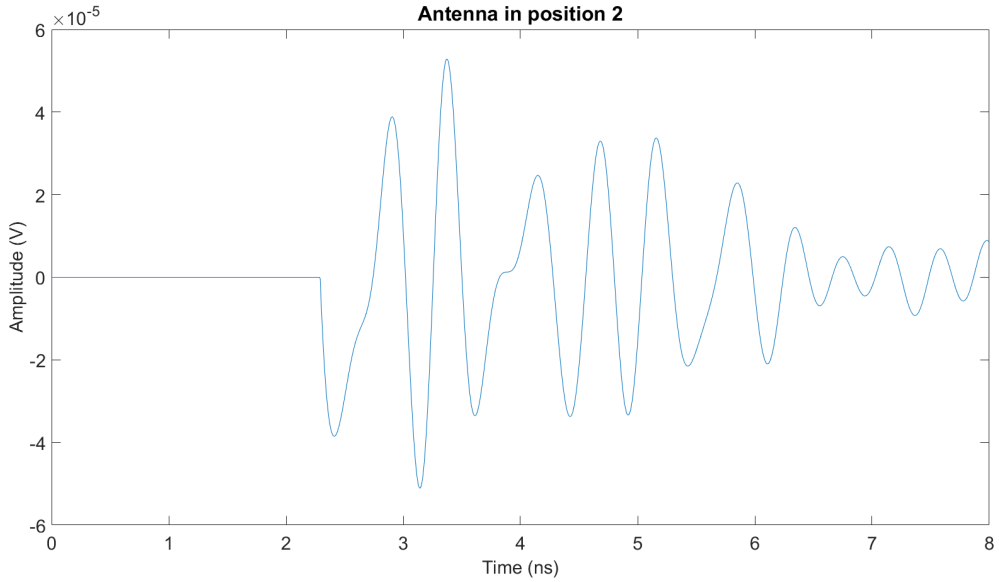

Figure 4.20: Water anomaly modified reflected signal, received at the antenna in position 2.

since there are several media in this scenario, it is also crucial to clearly define the different zones in which the propagation occurs, according to the model from figure 4.13. Since the air/bone interface is easily detected by the reflections from figure 4.8, the peak occurrence time allows to determine how far this this dielectric boundary is from the antenna. In fact, by rearranging equation 4.2, it is possible to determine a circumference of radius, using expression 4.15,

$$r = \frac{ct_p - d_{ant}}{2} \tag{4.15}$$

which illustrates at which distance the reflection occurs. By computing the distance from all points of that circumference to the origin of the scanning grid, in which the human head model is centered, the coordinates which yield the mininum distance are taken. By performing this approach to all the N antennas, it is possible to use the Matlab cubic spline interpolation method [30] to determine the curve that defines the shape of the human head model. Taking into account the average bone thickness, which the CST Studio Suite model has, the obtained curve distances to the origin are shrank and the curve now represents the delimiting zone of the bone/brain dielectric boundary, as seen in figure 4.21. By inspecting

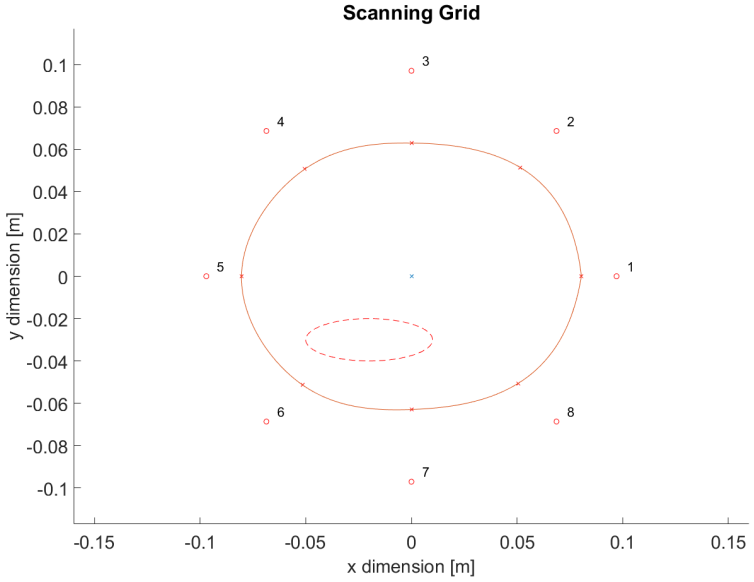

Figure 4.21: Delimiting curve of the bone/brain dielectric boundary.

if each point in the scanning grid is either inside or outside the delimiting curve, a boolean value is assigned to each position, which will be used to assign a permittivity value to each point, thus allowing to evaluate if the signal is propagating in the brain or in the air. This was implemented in Matlab according to

while *Not all scanning grid positions are considered* **do**
  Get coordinates in the scanning grid for each position;
  if *Is inside the delimiting curve* **then**
    Assign permittivity value as $\epsilon_r = 49$;
  else
    Assign permittivity value as $\epsilon_r = 1$;
  end
end

The use of the spline function provides a new degree of freedom, since it allows the implemention of the Fermat's Principle in the algorithm. As described before, the Fermat's Principle states that, between two points, light's travelling time between them is the minimum. This is the physical principle which explains the refraction and difraction phenomena that are expected to occur in a complex propagation media such as this one. In order to implement the Fermat's Principle, some approximations had to be made. First, the propagation time in the air is an exact measure of the air/skin dielectric boundary

reflection. A reading of the peak occurrence time for all signals is made, and that value is defined as the propagation time in the air, t_{air}. Since it is not pratical to have values for the bone thickness in all points of the skull, its average thickness is considered throughout the process, $h_{bone} = 6.32$ mm. Since the delimitation of the zones only separates the air and brain, a constant propagation time is defined for the bone propagation medium, t_{bone}, defined by expression 4.16,

$$t_{bone} = \frac{2h_{bone}\sqrt{\epsilon_r}}{c} \tag{4.16}$$

leaving the propagation inside the brain to be accounted. Since the propagation time must be the minimum between the antenna and the anomaly through the three different media, by knowing their permittivities it is possible to assume that the optimal way to minimize the propagation time is to minimize the distance between the bone/brain dielectric boundary and the head interior. While, in the air/bone interface a single point was considered as the reflection cause, in the bone/brain boundary a plane wave approach is used for the transmission in this media transition, as seen in figures 4.22 and 4.23. This leads to a multitude of propagation paths that are possible, with the one which produces the mininum distance to the considered point in the grid being chosen. Considering (a_i, b_j) the coordinates of the points in the scanning grid and (α_i, β_j) the points that are considered for the plane wave in the boundary, it is possible to write expression 4.17,

$$d_{brain} = d_{min} = min\sqrt{(\alpha_i - a_i)^2 + (\beta_j - b_j)^2} \tag{4.17}$$

for all i and j considered, which introduces Fermat's Principle to the algorithm. The propagation time may then be computed using expression 4.18,

$$t_{brain} = \frac{2d_{brain}\sqrt{\epsilon_r}}{c} \tag{4.18}$$

thus allowing to write equation 4.19,

$$t = t_{air} + t_{bone} + t_{brain} \tag{4.19}$$

This approach concludes the inclusion of the Fermat's Principle in the DAS algorithm, allowing the image reconstruction from the reflected signals to take place. Using the reflected signals seen in figure 4.16 and following the methodology described throughtout this section, the reconstructed images using the DAS algorithm may now be presented. First, in figure 4.24, it is possible to clearly see the two zones previously mentioned. The DAS algorithm was implemented in such a way that only the points of the scanning grid inside the head zone are considered for the distance calculations, therefore reducing computation time. This zone is characterized by the darkest of blue colours, meaning zero summed signal amplitudes. Inside the delimiting zone, marked in yellow, the DAS procedure is applied as described earlier in this section. This image simply has the summed amplitudes of the signals. Due to Fermat's Principle being applied, the circumferences seen in the air are no longer occurring, but instead appear

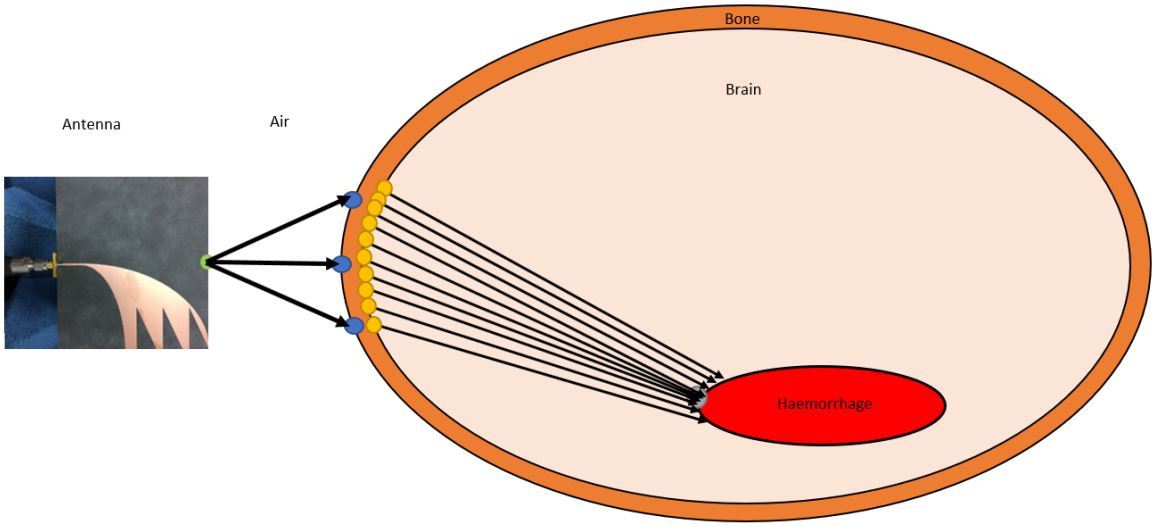

Figure 4.22: Human head propagation model, considering the Fermat's Principle.

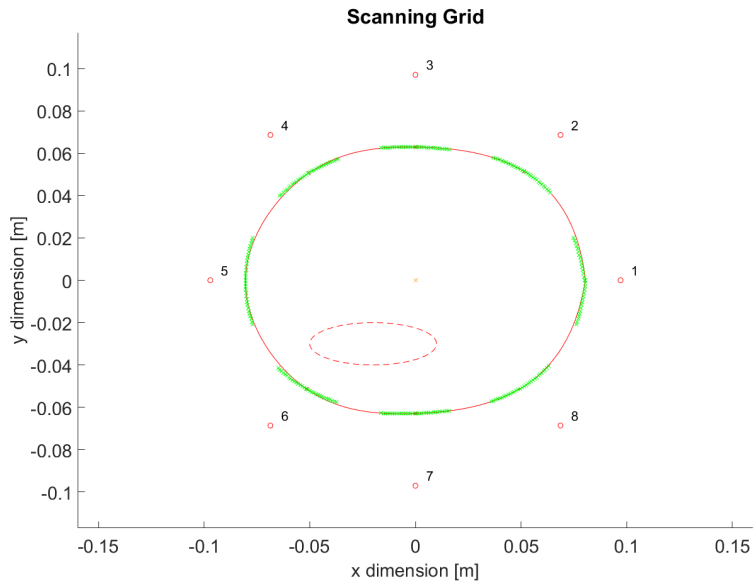

Figure 4.23: Scanning grid, delimiting curve of bone/brain dielectric boundary and Fermat's Principle, as seen in Matlab.

as curves that overlap eachother. The darker red colours clearly show the detection, but due to the signal amplitudes being so low and the approximations made, there is a loss of resolution on the detection. On figure 4.25, the amplitude values are squared, resulting in a more clear image of the detection. The anomaly is highlighted in relation to the curves overlapping, as seen before. There is a noticeable improvement on the clarity of the detection, with the edges of anomaly being detected by the darker red spots, also seen in the interior of the green mark that shows the limits of the anomaly. In order to make the image reconstruction a more robust process, it was assessed the adition of an integration window around the peak occurence time. Instead of simply computing it and getting its amplitude value for the

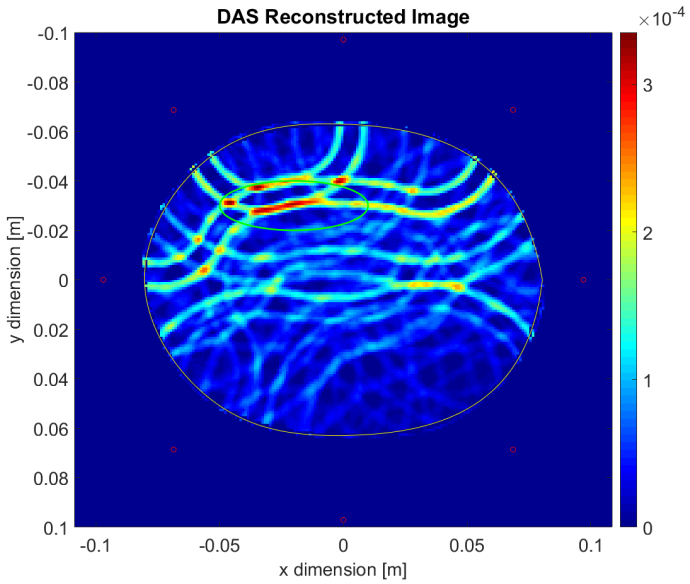

Figure 4.24: DAS image reconstruction for a water anomaly, inside a human head model.

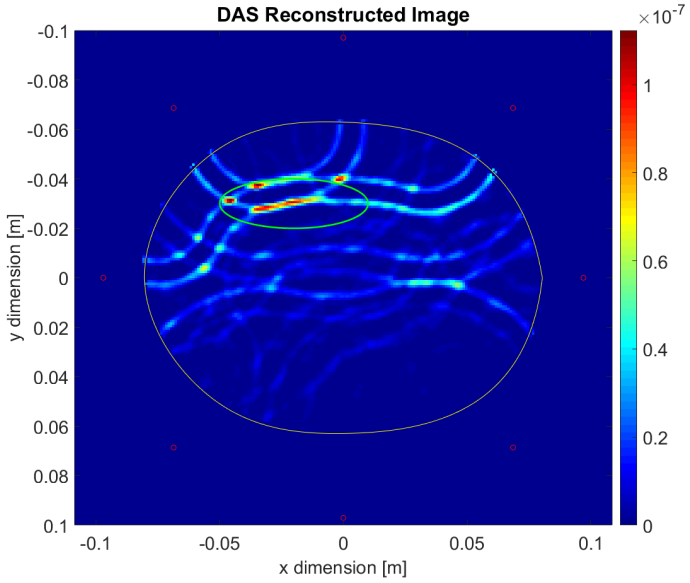

Figure 4.25: DAS image reconstruction for a water anomaly, inside a human head model, with squared values of the amplitudes.

considered time value, a time interval is considered to both sides of the computed peak time. Then, an integration of the signal is performed on the considered time interval. If t_p is the peak occurence time and $a_i b_j$ the amplitude value for each position of the scanning grid, expression 4.20 can be written

$$a_i b_j = \int_{t_p-\Delta t}^{t_p+\Delta t} y(t)dt \tag{4.20}$$

with Δt being the integration window width. Since there is a spatial relation with time, it is possible to also define the spatial distance that is being evaluated with the integration window, seen with equation

4.21

$$\Delta d = \frac{c\Delta t}{\sqrt{\epsilon_r}} \tag{4.21}$$

which extends the scanning distance from the evaluated point in the scanning grid to a radius of Δd around it.

The integration was introduced to the DAS algorithm, which considered $\Delta t = 0.1$ ns, corresponding to, according to expression 4.21, $\Delta d = 4.3$ mm. Therefore, for a certain point in the scanning grid, there is also a spatial scan centered at that point, with radius 4.3 mm around it. Applying the integration window, it is possible to display the resulting images, in figures 4.26 and 4.27. As expected, the integration

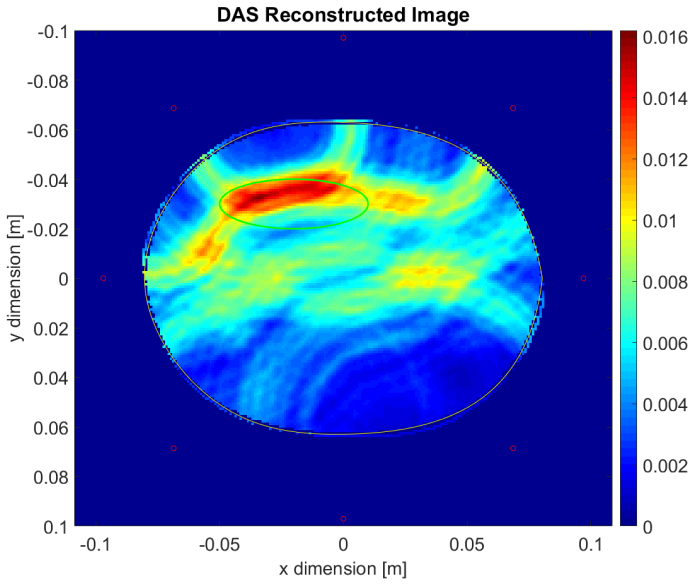

Figure 4.26: DAS image reconstruction for a water anomaly, inside a human head model, applying the integration window.

windows considers more amplitude values for each position of the scanning grid, therefore increasing the amplitude values seen in the colour bar. In fact, considering the highest values of amplitudes seen in the colour bars, the use of the integration window, with $\Delta t = 0.1$ ns, provides an increase of 34.53 dB in the displayed amplitudes, thus allowing a more clear image of the anomaly to be displayed. Considering, again, the squared values of the integrated signal amplitudes, the expected focusing and highlighting of the image occurs, with an improvement of the same magnitude when compared to the previous squared amplitude values displayed image. In fact, for situations with complex propagation media and very low amplitude signals, the benefits of using a time integration window are evident. In a matter of the developed code complexity and performance, the program running time in order to display both images without and with the integration window (figures 4.24, 4.25, 4.26 and 4.27, respectively) are shown in Table 4.1. As expected, the introduction of the integration window increases the computation time of the developed program, although an increase of 71.2 seconds is tolerable in the situations that a microwave imaging system is expected to be deployed. In fact, the running times comply with the expectations that theses systems provide a quick diagnosis in an emergency situation. These results were obtained in a machine with an Intel Core i7-2670QM Processor clocked at 2.7 GHz, 6 GB RAM

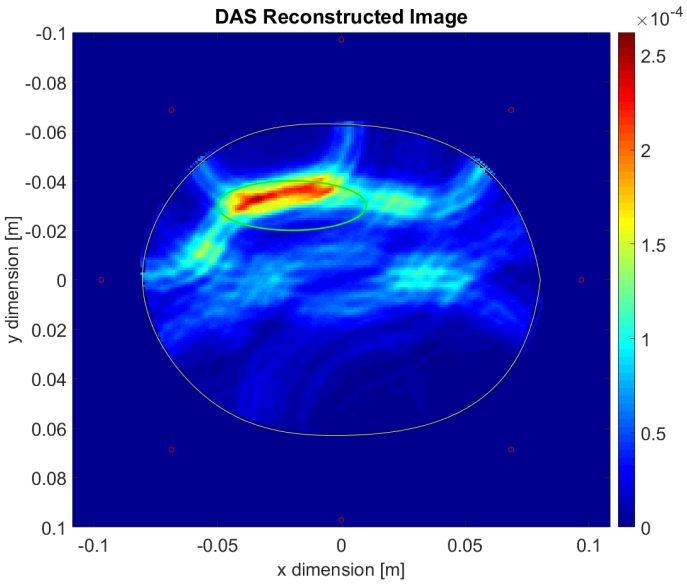

Figure 4.27: DAS image reconstruction for a water anomaly, inside a human head model, applying the integration window, with squared values of the amplitude.

Table 4.1: Image Reconstruction Algorithm without and with integration window running time

Algorithms Running Time [s]	
DAS without Integration Window	115.76
DAS with Integration Window	186.96

and running Matlab R2016a in Windows 10 Pro. The simulation work in CST Studio Suite is terminated

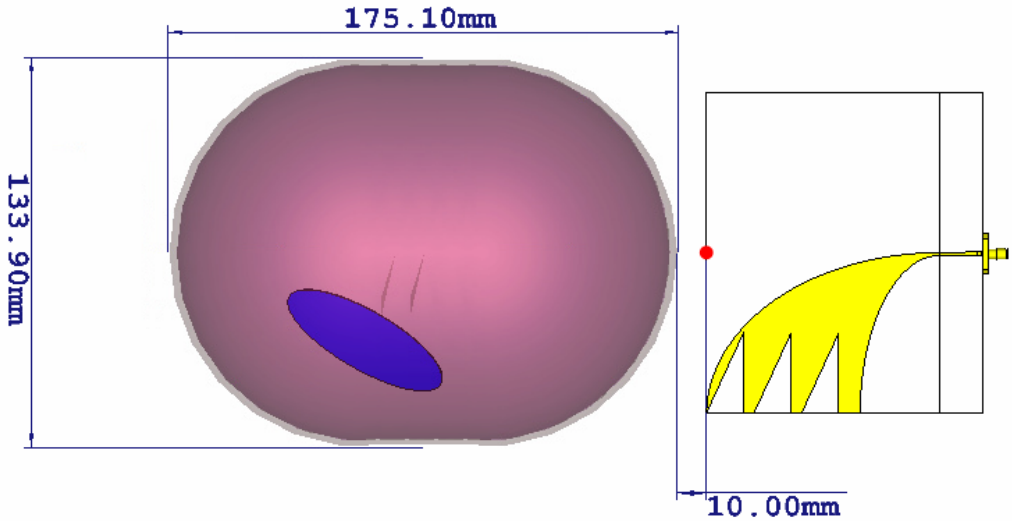

Figure 4.28: Simulation set-up, as seen in CST Studio Suite, with Human Head model and tilted water anomaly.

by evaluating a different position of the anomaly. Its position in the previous simulations provides a simpler scenario in which the air/bone and brain/anomaly dielectric boundaries have the same shape

and orientation, thus making the detection easier and, consequently, providing an image that resembles not only the dimensions and location, but also the shape of the detected object. A model, with the same water anomaly emulating an haemorrhage, but with its orientation tilted 30° was simulated. The CST Studio Suite model is seen in figure 4.28. Using the developed program, it is also possible to detect the existence of the anomaly, although some information on its shape, location and dimensions is lost. This can be seen in figures 4.29 and 4.30. The same integration window was used, meaning $\Delta t = 0.1$ ns. As said previously, the detection occurs, although the results have to be interpreted and discussed to assess their validity. Since there is now a region of the anomaly closer to the antennas, resulting in a reflection from it having higher amplitude values due to the attenuation inside the brain, this will produce the darker red colours closer to the bone/brain dielectric boundary, leaving the others to fall into the yellowish colours, meaning a lower value of the summed amplitudes. Due to the orientation of the anomaly, the detection curves are oriented according to the 30° tilt, which is a clear sign of a correct detection. However, a clear follow up on the target orientation is lost, therefore focusing the detection on the dieletric boundary closer to the antennas. A possible solution to solve this issue is to place more antennas in the scanning array. For instance, the use of 16 antennas, angularly spaced by 22.5°, could lead to a more clear reception of the anomaly's reflections, thus allowing for a better follow up on the target shape and dimensions, thus allowing more darker red colours to appear in areas closer to the center of the emulated haemorrhage. Despite the difficulties in providing a clear

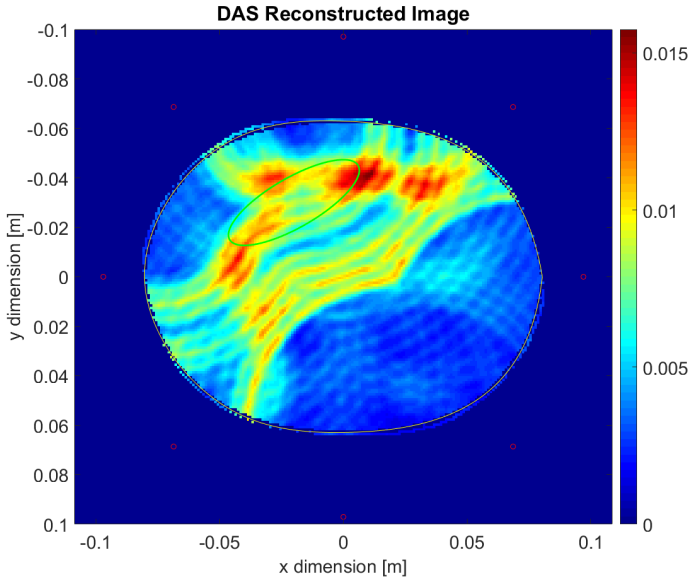

Figure 4.29: DAS image reconstruction for a tilted water anomaly, inside a human head model.

image like in the previous situations, there is still a strong evidence of detection which, in a binary case of detection, proves to be helpful in an emergency situation and indicates the need to perform more accurate diagnosis exams. These demonstrations of the DAS algorithm detections working in a complex propagation medium, with three different accountable permittivities, allow to emulate the measurement scenario. It consists of a simple homogeneous phantom, for which will be used a real size human skull plastic model, a liquid mixture with controlled permittivity, to be made equal to $\epsilon_r = 49$ and a thin and

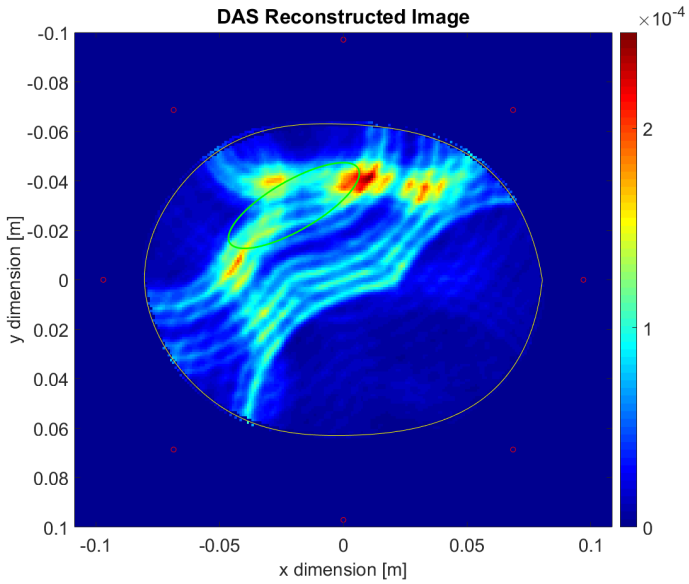

Figure 4.30: DAS image reconstruction for a tilted water anomaly, inside a human head model, with squared values of the amplitude.

small plastic tube with tap water are going to be used in the measurements. A complete description of the measurement set-up, phantom production, measurement methodology and procedure and, finally, the reconstructed images using the experimental data will be presented in the following section.

4.2 Image Reconstruction using a Human Head Phantom

4.2.1 Human Head Phantom and Measurement Set-Up

With the Image Reconstruction Algorithm developed, as seen in the previous section, the measurements with a Human Head Phantom were conducted. A real size human head skull model was used, as seen in figure 4.31, as the liquid phantom container. The skull model was made of polyurethane, with its permittivity being unknown, altough being given in a certain range [31]. In Appendix B, its permittivity measurement process is described, and the value $\epsilon_r = 2.75$ was considered in this experiment. The liquid phantom was produced by mixing distilled water, Sigma Aldrich Triton X-100 [32] and sodium cholidre. From the works of [33], the mixture contained 68% distilled water, 32% Triton X-100 and 4.4 g/L of sodium chloridre. A volume of 1.5 L of liquid phantom was produced, with its permittivity being measured using the procedure described in Appendix C. The obtained value for phantom permittivity is $\epsilon_r = 45.45$, which is approximately the considered permittivity throughout the simulations, $\epsilon_r = 49$. In order to emulate an haemorrhage, a plastic tube, filled with tap water ($\epsilon_r = 80$, at 2.45 GHz), was glued using Araldite [34] to a holding structure made of thin plastic tubes, in order for it to be inserted inside the skull. The developed structure emulating the haemorrhage is seen in figure 4.32. The anomaly was placed in a position close to the one seen in the simulations, held by a rubber lid made to fit an opening in the skull model. This position was kept during the measurements, with the plastic tube being always in the same place, as seen in figure 4.33. This figure also shows the real dimensions of the skull model.

Figure 4.31: Real size human skull model.

Figure 4.32: Plastic tube filled with tap water and holding structure.

The anomaly was totally immerse in the liquid phantom which filled the human skull model above the line which is seen as the separation of the two parts of the model, by the orange dashed line. The dividing line is called the reference line, and the plastic tube was placed 1.7 cm below this line, with the PTVA also being positioned 1.7 cm below the reference line, as seen in figure 4.34. These measurements follow the simulation process described in the previous section and, since only one PTVA was prototyped, the antenna was used in a fixed position, held to a styrofoam and radiation absorving structure to avoid undesired reflections or interference on the measurements. This implies that the human head phantom will have to be rotated in front of the PTVA, using an azimuth positioner. In order to keep the human head phantom on the same position during the measurements, an Expanded Polyurethane (E-PUR)

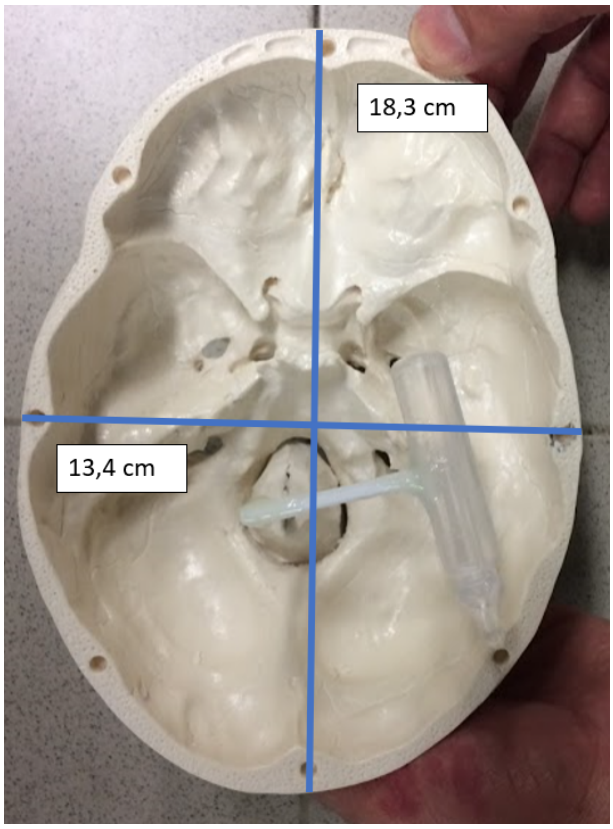

Figure 4.33: Position of the anomaly inside the open human head skull model.

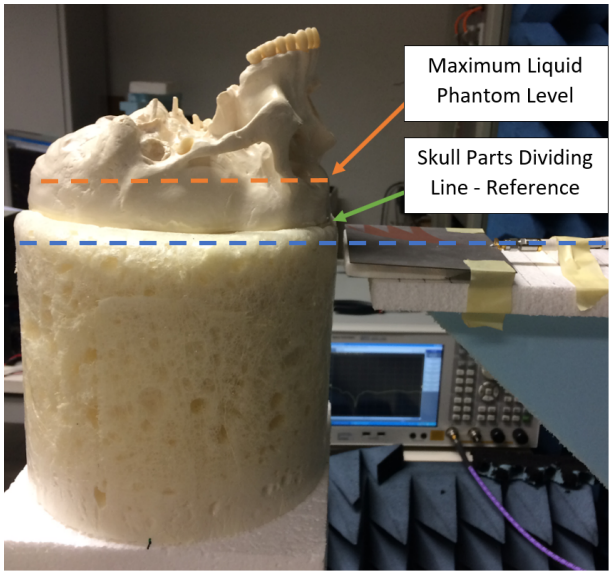

Figure 4.34: Reference line, position of the antenna 1.7 cm below it and maximum liquid phantom level.

foam was used to create a lightweight and non interfering mould. This E-PUR foam has, like styrofoam, permittivity close to the air, thus not interfering with the conducted measurements. The fabricated E-PUR foam mould and the complete measurement set-up is seen in figure 4.35.

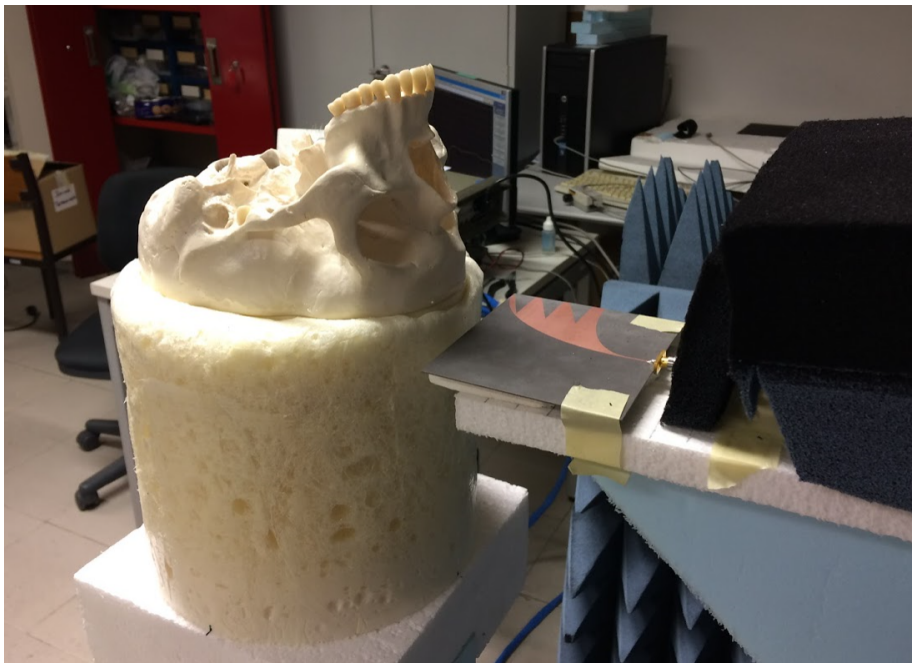

Figure 4.35: Fabricated measurement set-up, with the PTVA and the human head phantom.

4.2.2 Image Reconstruction Algorithm Results

Using a VNA, at the RF Laboratory of *Instituto de Telecomunicações*, the S_{11} parameter was measured in free space, for calibration, and in intervals of 45°, like previously done in the simulation, with the PTVA being placed 1 cm away from phantom in its closest point to it. The measurements were perfomed with and without the tap water tube, meaning that measurements were conducted with and without the haemorrhage emulating structure. This allows to obtain a benchmarking image of the detection. By subtrating the S_{11} parameter with the anomaly inside the phantom and the S_{11} parameter without the anomaly, the effects of the existence of both skull model and liquid phantom are negleted, leaving only the signal reflections originating from the anomaly. As seen previously, the reflections from the air/bone dielectric boundary are clearly identified and are shown in figure 4.36. Comparing with figure 4.8, the reflected signal amplitudes and, consequently, pulse shapes, are differ from eachother noticeably. Unlike the simulation model designed previously, the use of a real size human skull model introduces different slopes around it, contributing to the aforementioned differences. Applying the spline cubic interpolation method, the mapping of the delimiting curve was complete and the dimensions obtained are accurate with the fabricated measurement set-up. In figure 4.37, the delimiting curve of the air/bone interface is shown. The reconstructed distance computed from antenna in positions 1 and 5 is 18.42 cm, which is a 0.12 cm from the 18.3 cm measured dimension. From antennas in positions 3 and 7, the distance using the spline cubic interpolation is 14.7 cm, which is 1.3 cm more than the measured 13.4 cm. The position of the plastic tube is also seen in this image. The produced image using the DAS algorithm is shown in figure 4.38. It is clear that the produced image, using the calibrations referred in the previous section, cannot locate the haemorrhage. Contrary to the simulations, the calibration process did not reveal as effective as seen before. Due to the human skull model not having the same slopes in

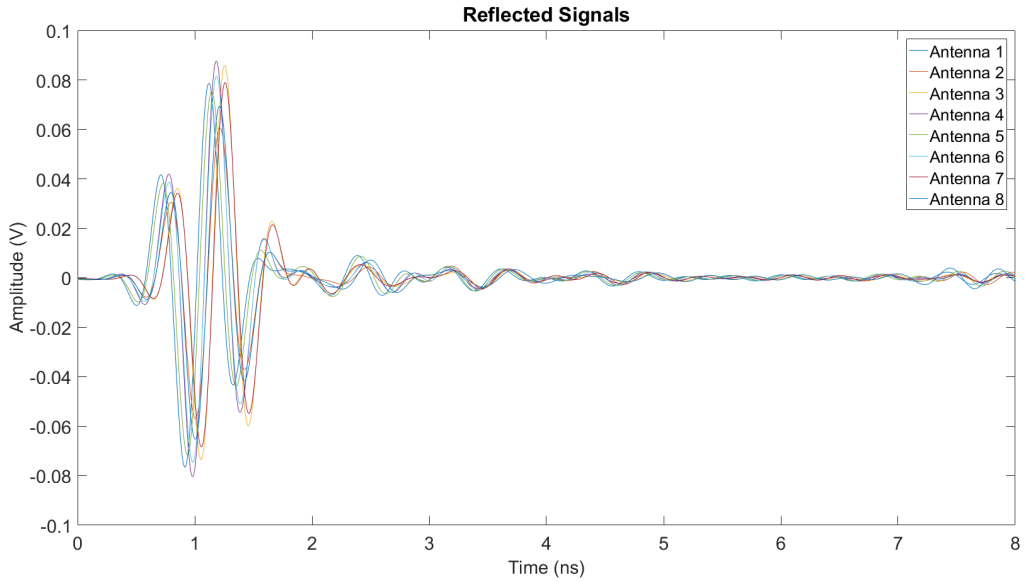

Figure 4.36: Reflected signals for each antenna position.

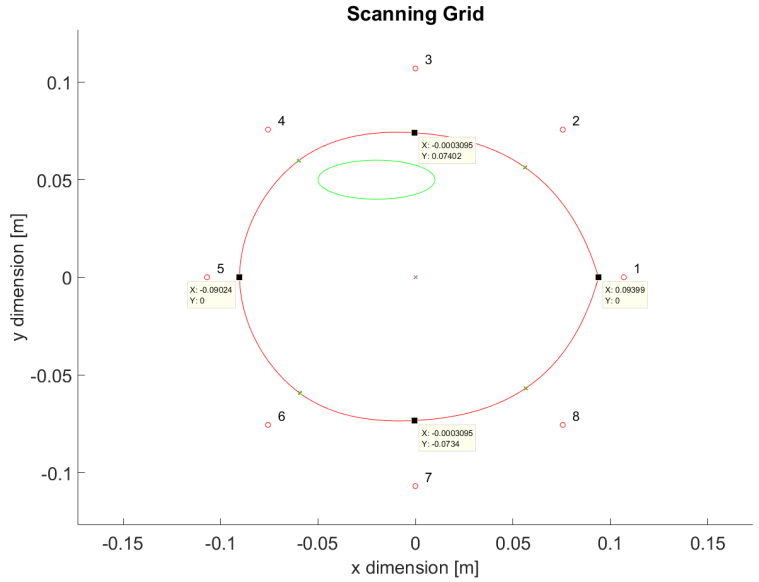

Figure 4.37: Delimiting curve of the air/bone dielectric boundary.

all faces, leading to the the air/bone dielectric boundary reflections presenting different pulse shapes, these interface reflections are not removed completely. For instance, in figure 4.39, it is seen that the calibration process described in the previous section did not work as intended. The automatic removal of the air/bone interface did not happen completely, which left the pulse shape present in the time instant of the air/bone reflection, therefore outshining all other signal reflections. The same issue happened, with less magnitude, in all the other antennas, with the reflection from the air/bone dielectric boundary being present in all signals used to produce the DAS reconstructed image. With the current State of the Art, this is a known issue and ongoing topic of investigation. Several techniques of artifact removal are being developed and investigated, namely entropy based algorithms [35], which are expected to solve

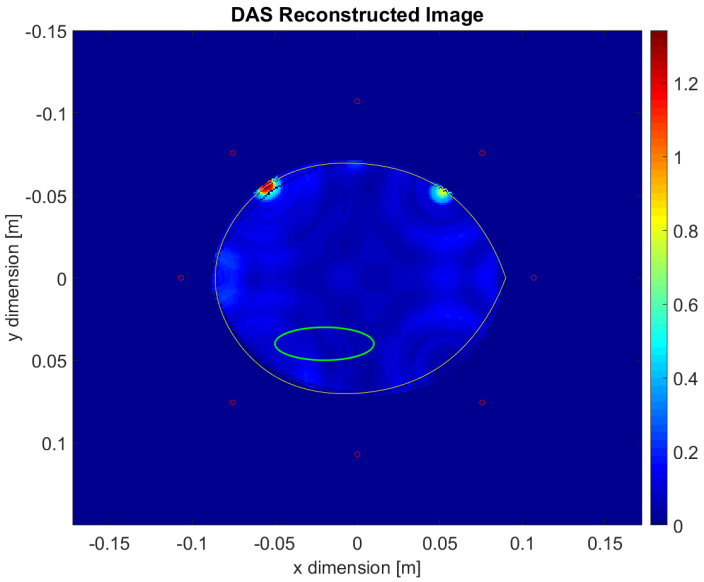

Figure 4.38: DAS image reconstruction for the human head phantom, with faulty calibration.

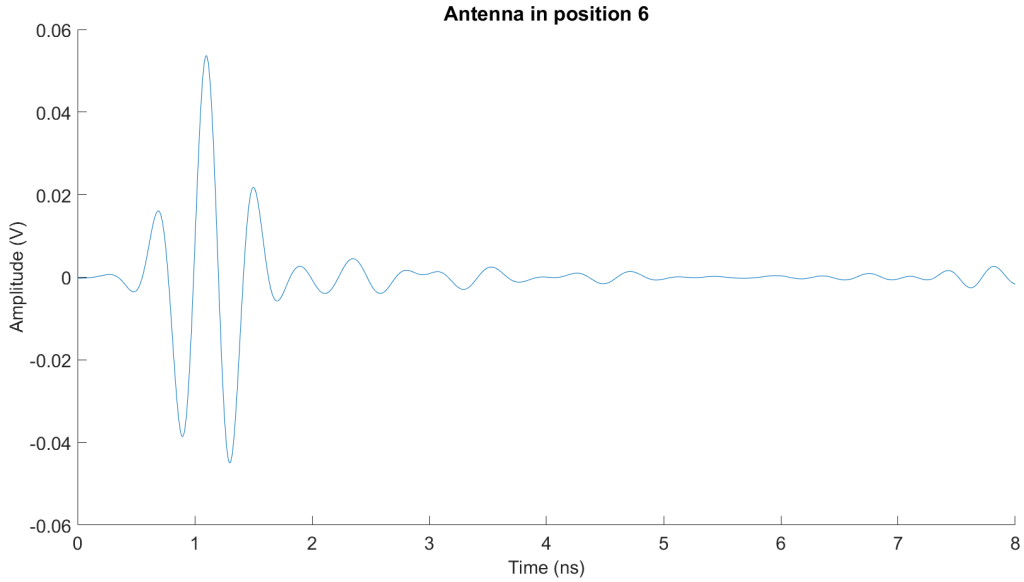

Figure 4.39: Antenna in position 6, with faulty calibration.

these difficulties. Knowing a priori the difficulties when facing real scenario measurements, as stated before, a measurement was made without the haemorrhage emulating plastic tube, using a different procedure, which consists in measuring the S_{11} parameter with the anomaly inside the phantom, and then removing it, repeating the measurements. Using this sort of calibration allows the complete removal of the air/bone dielectric boundary, therefore solving the faced calibration problems. By synthesizing the reflected signals following this approach, the only signal response detected is the reflection from the haemorrhage. For instance, the antenna in position 4 accurately detects the reflection from the plastic water tube. All the antennas contribute for the detection, allowing the DAS algorithm to display an image as intented, as seen in figure 4.41. The displayed image correctly shows the haemorrhage emulating

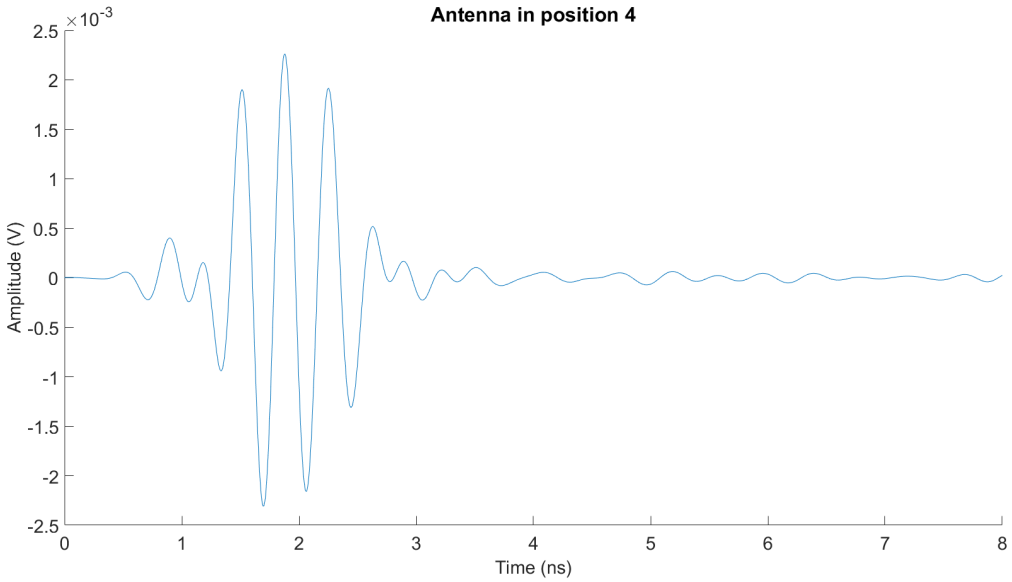

Figure 4.40: Antenna in position 4, with correct haemorrhage detection.

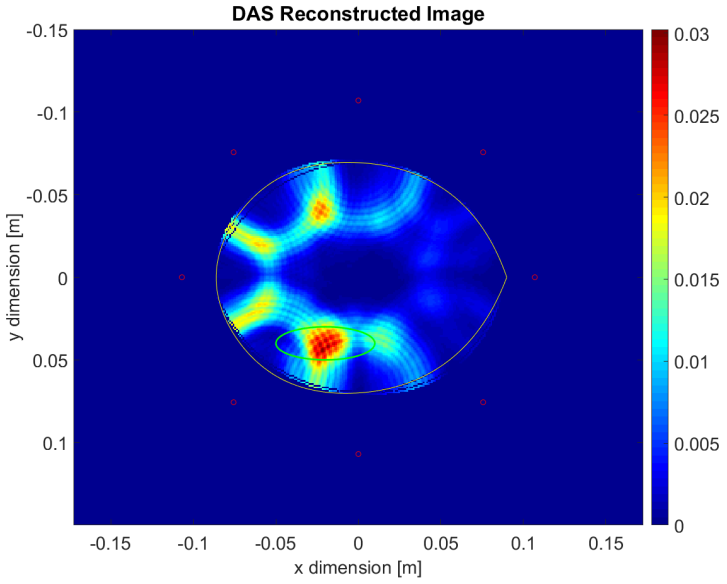

Figure 4.41: DAS image reconstruction for the human head phantom, using an alternative calibration method.

structure existence, as seen by the darker red colours inside the green line, denoting its real position. The appearance of symmetric "ghost" detections in respect to the $y = 0$ m axis may be explained due to certain limitations in the DAS procedure, which considers a 2D scanning scenario, while the measurements were performed on a 3D environment. A possible path, which complies with Fermat's Principle, may exist due to multiple reflections phenomena at the air/liquid phantom dielectric boundary, which creates this sense of symmetry around the axis. While, in the simulations, all the volume was filled with liquid, with the anomaly existing in the middle of it, in this situation that is not the case.

These measurements, while not successful in providing a detection of the anomaly using the automatic calibrations designed for the simulation model in CST Studio Suite, made possible to detect the haemor-

rhage emulating structure using a different calibration approach. This calibration, while not being feasible in a real world scenario, allowed to overcome the air/bone dielectric boundary and made possible for the DAS to reconstructed an image of the inside of the human head phantom. The produced image, while showing some “ghost” detections due to the aforementioned hypothesis, show the location of the supposed haemorrhage, as intended.

These final remarks conclude Chapter 4 and the conducted work in this Master Thesis.

Chapter 5

Conclusions and Future Work

5.1 Conclusions

This Chapter provides the final remarks of the whole Thesis. In the first part of the text, following the literature review which provided the foundaments and knowledge to carry this task, the ”Palm Tree Vivaldi” antenna was prototyped. Starting with the requirements desired for an antenna suitable for a microwave imaging system, a basic antipodal Vivaldi antenna and novel features in Vivaldi antennas, the PTVA was designed. By adjusting the Base Vivaldi antenna dimensions and feeding structure, most of the desired frequency band of operation was achieved, with the antenna exhibiting a directive radiation pattern and small pulse distortion. The introduction of the edge slot resonators in the Vivaldi antenna (now called PTVA) radiators allowed to confine the electric field, thus increasing the surface current distribution in these locations, leading to an increase of the electric lenght of the antenna. This increase allowed the PTVA operating frequency band lower limit to decrease, therefore occupying more of the sought 1-3 GHz frequency band. Not only this was achieved, but also the electric lenght increase of the antenna allows its miniaturization, since it is possible to maintain the performance with the introduction of the resonators and reduce the antenna's size. With this in mind, the designed PTVA antenna exhibits the desired UWB characteristic in the band of 1.58-2.89 GHz band, low pulse distortion and directive properties. This is achieved in a miniaturized design, in a compact and thin structure. The PTVA was then prototyped, with the fabricated antenna showing the same S_{11} behaviour as the simulations, achieving UWB in the 1.61-3.02 GHz, occupying most of the 1-3 GHz band, and preserving the desired properties observed in the simulations. The antenna was successfully prototyped and tested, and fulfils the requirements needed for a Microwave Imaging System. Following the antenna design chapter of this dissertation, the imaging algorithm is adressed. After a conceptual illustration of the Delay and Sum algorithm, simulations using CST Studio Suite are conducted, using the designed PTVA model. After a successful demonstration of the DAS reconstructing a scanning environment composed of a metal target in the air, a propagation model for the human head is proposed and designed in CST Studio Suite. By simulating the developed model, calibration strategies are proposed to overcome the air/bone dielectric boundary and detect the signal reflected from a water anomaly, which emulates an haemorrhage. Following the proposed calibration description, Fermat's Principle was taken into account

in the DAS algorithm propagation times computation. Finally, after correctly detecting the anomaly, an integration window was implemented to further improve its highlight, improving image resolution. All this was achieved with the DAS algorithm running in an acceptable computation time. With the simulations results being positive, it was decided to build a phantom and perform measurements with the prototyped PTVA. Using a polyurethane human skull model as container, producing a liquid phantom and fabricating a water anomaly, which emulates an haemorrhage, measurements were perfomed in laboratory. Not only the S_{11} parameter measurements, required for the image reconstruction process, were conducted, but also measurements to determine solid and liquid materials permittivity accurately. While, using the proposed calibration methods, the anomaly could not be detected, the use of different calibration method allowed to perform its detection. This calibration consisted in measuring the S_{11} parameter with the anomaly and then subtracting the S_{11} parameter without it. The described procedure made the removal of the air/bone reflections possible and allowed to demonstrate the DAS detection capabilities, highlighting the haemorrhage emulating structure in its location.

5.2 Future Work

Following this Thesis, several topics are left open for future reasearch work. For instance, the aditional miniaturization of Vivaldi antennas, while keeping the working band in the 1-3 GHz interval, is desired. The effect of different edge slot resonator shapes and orientations on the electric lenght increase of the antenna and its miniaturization possibilities is crucial to have smaller antennas deployed in a real world scenario. Moreover, aditional miniaturization strategies are suggested to be researched.

The biggest challenge in microwave image reconstruction is, undoubtedly, the artifact removal calibrations. In this work, the proposed calibration failed when accounting laboratory measurements, and investigation on overcoming the biggest reflections from the first dielectric boundary are suggested to take place. In fact, calibration techniques or signal processing methods investigation is suggested in order to solve the hardest challenge in microwave imaging systems. The extension of the DAS algorithm to a 3D scanning environment is also a path of investigation, since it should allow more accurate propagation times estimations, due to more paths to the anomalies being considered. Further improvements on the existing algorithms, either in the time or frequency domain, are also suggested, aiming at improving image resolution and accuracy.

Bibliography

[1] A. Mobashsher, A. Mahmoud, and A. M.Abbosh, "Portable Wideband Microwave Imaging System for Intracranial Hemorrhage Detection Using Improved Back-Projection Algorithm with Model of Effective Head Permittivity," *Sci. Rep. 6*, no. 20459, 2016.

[2] K. E. Thomenius, "Evolution of Ultrasound Beamformers," *Proc. of the IEEE Int. Ultrasounds Symp.*, pp. 1615–1622, September 1996.

[3] B. J. Mohammed, A. M. Abbosh, S. Mustafa, and D. Ireland, "Microwave System for Head Imaging," *IEEE Trans. Instrum. Meas.*, vol. 63, pp. 117–124, January 2014.

[4] P. S. Hall and Y. Hao, *Antennas and Propagation for Body-Centric Wireless Communications*, ch. 2. Electromagnetic Properties and Modeling of the Human Body, pp. 11–20. Artech House, 2006.

[5] Federal Communications Commission, "Specific Absorption Rate SAR for Cellular Telephones." `https://www.fcc.gov/general/specific-absorption-rate-sar-cellular-telephones`, accessed 13-10-2017.

[6] A. T. Mobashsher and A. M. Abbosh, "Three-Dimensional Human Head Phantom with Realistic Electrical Properties and Anatomy," *IEEE Antennas Wireless Propag. Lett.*, vol. 13, pp. 1401–1404, 2014.

[7] International Telecommunication Union - Radiocommunication, "Recommendation ITU-R SM.1755 - Characteristics of Ultra-Wideband Technology." `https://www.itu.int/dms_pubrec/itu-r/rec/sm/R-REC-SM.1755-0-200605-I!!PDF-E.pdf`, acessed 31-05-2017.

[8] Federal Communications Commission, "Revision of Part 15 of the Commission's Rules Regarding Ultra-Wideband Transmission Systems." `https://apps.fcc.gov/edocs_public/attachmatch/FCC-02-48A1.pdf`, accessed 31-05-2017.

[9] J. Bourqui, M. Okoniewski, and E. C. Fear, "Balanced Antipodal Vivaldi Antenna with Dielectric Director for Near-Field Microwave Imaging," *IEEE Trans. Antennas Propag.*, vol. 58, no. 7, pp. 2318–2326, 2010.

[10] E. C. Fear, J. Bourqui, M. A. Campbell, and T. Williams, "Antenna evaluation for ultra-wideband microwave imaging," *Int. J. Antennas Propag.*, vol. 2010, 2010.

[11] S. Lin, S. Yang, A. E. Fathy, and A. Elsherbini, “Development of a Novel UWB Vivaldi Antenna Array using SIW Technology,” *Progress In Electromagnetic Research*, vol. 90, pp. 369–34, 2009.

[12] A. T. Mobashsher and A. M. Abbosh, “Slot-Loaded Folded Dipole Antenna with Wideband and Unidirectional Performance for L-Band Applications,” *IEEE Antennas Wireless Propag. Lett*, vol. 13, pp. 798–801, 2014.

[13] A. T. Mobashsher and A. M. Abbosh, “Compact 3-D Slot-Loaded Folded Dipole Antenna with Unidirectional Radiation and Low Impulse Distortion for Head Imaging Applications,” *IEEE Trans. Antennas Propag.*, vol. 64, pp. 3245–3250, July 2016.

[14] A. M. Abbosh, “Directive Antenna for Ultrawideband Medical Imaging Systems,” *Int. J. of Antennas and Propag.*, 2008.

[15] A. T. Mobashsher, A. M. Abbosh, and Y. Wang, “Microwave System to Detect Traumatic Brain Injuries Using Compact Unidirectional Antenna and Wideband Transceiver with Verification on Realistic Head Phantom,” *IEEE Trans. Microw. Theory Tech.*, vol. 62, pp. 1862–1836, September 2014.

[16] N. Hamzah and K. A. Othman, “Designing Vivaldi Antenna with Various Sizes using CST Software,” *Proc. of the World Congr. on Eng.*, vol. 2, July 2011.

[17] Y.-W. Wang, G.-M. Wang, and B.-F. Zong, “Directivity Improvement of Vivaldi Antenna Using Double-Slot Structure,” *IEEE Antennas Wireless Propag. Lett.*, vol. 12, pp. 1380–1383, 2013.

[18] J. Kowalewski, U. Dey, T. Mahler, and T. Zwick, “Vivaldi Antenna with Improved Directivity for Medical Applications,” *German Microwave Conference*, pp. 123–128, March 2015.

[19] K. Kikuta and A. Hirose, “Compact Folded-Fin Tapered Slot Antenna for UWB Applications,” *IEEE Antennas Wireless Propag. Lett.*, vol. 14, pp. 1192–1195, 2014.

[20] A. M. D. Oliveira, M. B. Perotoni, S. T. Kofuji, and J. F. Justo, “A Palm Tree Antipodal Vivaldi Antenna With Exponential Slot Edge for Improved Radiation Pattern,” *IEEE Antennas Wireless Propag. Lett.*, vol. 14, pp. 1334–1337, 2015.

[21] G. Matrone, A. S. Savoia, G. Caliano, and G. Magenes, “The Delay Multiply and Sum Beamforming Algorithm in Ultrasound B-Mode Medical Imaging,” *IEEE Trans. Med. Imag.*, vol. 34, pp. 940–949, April 2015.

[22] X. Zhuge, T. Savelyev, A. Yarovoy, L. Ligthart, and B. Levitas, “Comparison of Different Migration Techniques for UWB Short-Range Imaging,” *Proceedings of the 6th European Radar Conference*, pp. 184–187, September 2009.

[23] Rogers Corporation, “Complete Product Listing.”

[24] K. R. Carter and J. W. Mink, “Microstrip Antenna Technology,” *IEEE Trans. Antennas Propag.*, vol. 29, no. 1, pp. 2–24, 1981.

[25] D.K.Srivastava, B.R.vishwvakarma, R.C.Saraswat, and J.P.Saini, "Investigation of Effect of Substrate Thickness and Permittivity of Rectangular Microstrip Antenna for Bandwidth Enhancement," *Int. Conf. on Information and Communication Tech. in Electrical Sciences*, pp. 970–973, 2007.

[26] D. M. Pozar, *Microwave Engineering*, ch. 4. Microwave Network Analysis, pp. 203–210. John Wiley and Sons, 2011.

[27] Rogers Corporation, "RT/duroid 5870 /5880." `http://www.rogerscorp.com/documents/606/acs/RT-duroid-5870-5880-Data-Sheet.pdf`, accessed 09-01-2018.

[28] J. R. Costa, C. R. Medeiros, and C. A. Fernandes, "Performance of a Crossed Exponentially Tapered Slot Antenna for UWB Systems," *IEEE Trans. Antennas Propag.*, vol. 57, no. 5, pp. 1345–1352, 2009.

[29] A. Moreira-Gonzalez, F. Papay, and J. Zins, "Calvarial thickness and its relation to cranial bone harvest," *Plast. Reconstr. Surg.*, vol. 117, no. 6, pp. 1964–1971, 2006.

[30] Mathworks, "Spline - cubic spline data interpolation." `https://www.mathworks.com/help/matlab/ref/spline.html`, accessed 06-02-2018.

[31] Prospector, "Polyurethane (PUR)." `https://plastics.ulprospector.com/generics/45/c/t/polyurethane-pur-properties-processing`, accessed 10-02-2018.

[32] Sigma Aldrich, "Triton X-100 for molecular biology." `https://www.sigmaaldrich.com/catalog/product/sigma/t8787?lang=pt&region=PT`, accessed 22-02-2018.

[33] N. Joachimowicz, C. Conessa, T. Henriksson, and B. Duchêne, "Breast phantoms for microwave imaging," *IEEE Antennas Wirel. Propag. Lett.*, vol. 13, pp. 1333–1336, 2014.

[34] Araldite Professional Adhesives, "Araldite standard." `http://www.go-araldite.com/products/epoxy-adhesives/araldite-standard-2-x-15ml-tube`, accessed 22-02-2018.

[35] M. A. Elahi, A. Shahzad, M. Glavin, E. Jones, and M. O'Halloran, "Hybrid artifact removal for confocal microwave breast imaging," *IEEE Antennas Wirel. Propag. Lett.*, vol. 13, pp. 149–152, 2014.

Appendix A

Palm Tree Vivaldi Antenna Masks

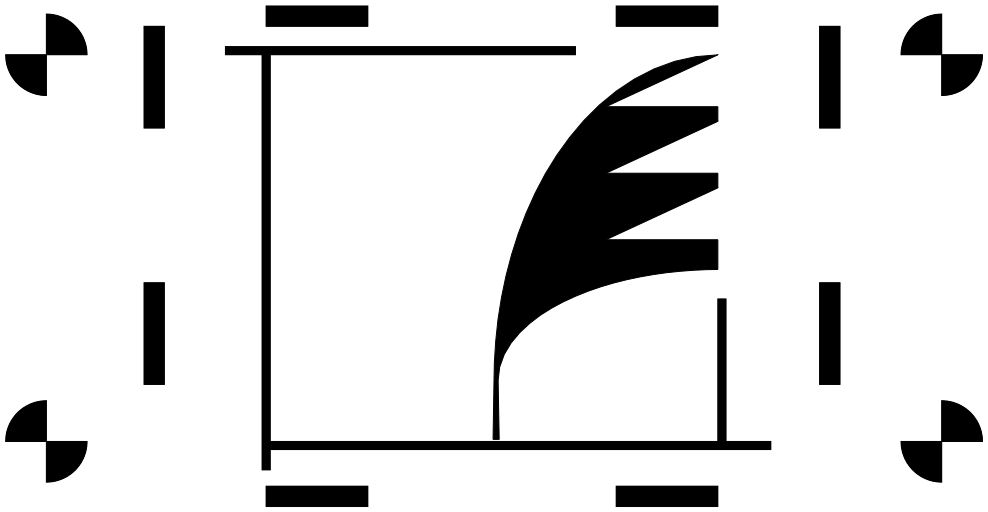

Figure A.1: Palm Tree Vivaldi antenna front layer mask.

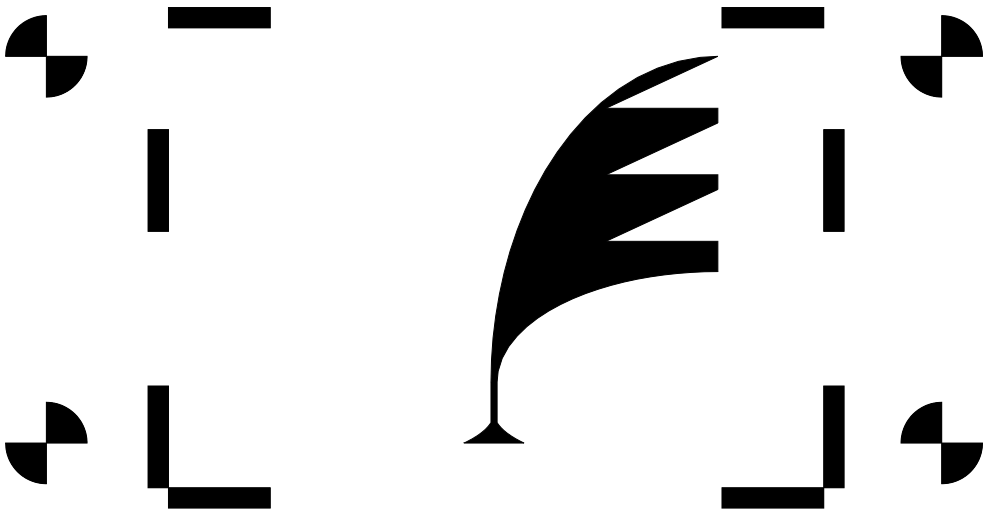

Figure A.2: Palm Tree Vivaldi antenna back layer mask.

Appendix B

Human Head Skull Model Permittivity Measurement

The human head phantom has three components. The real size human skull model (figure B.1), made of polyurethane (PUR), the homogeneous liquid mixture and a small plastic tube filled with tap water. While tap water permittivity is known, PUR permittivies vary depending on the test method [31], from 2.69 to 6.14. It is crucial to know the human skull model permittivity in order to accurately estimate the propagation time inside this medium. The permittivity of a material may be determined by designing

Figure B.1: Real size human skull model, made of PUR.

a transmission set-up between two antennas at a certain distance, with a piece of that material, with known thickness, obstructing the transmission link, as seen in figure B.2. This shall introduce a phase delay when compared to the unobstructed transmission link, therefore allowing to obtain its permittivity. This assumption is expressed by equations B.1 and B.2, for the unobstructed and obstructed links, respectively,

$$\phi_1 = k_0(d_1 + d_2 + d_3) + \phi_0 \tag{B.1}$$

$$\phi_2 = k_0(d_1 + nd_2 + d_3) + \phi_0 \tag{B.2}$$

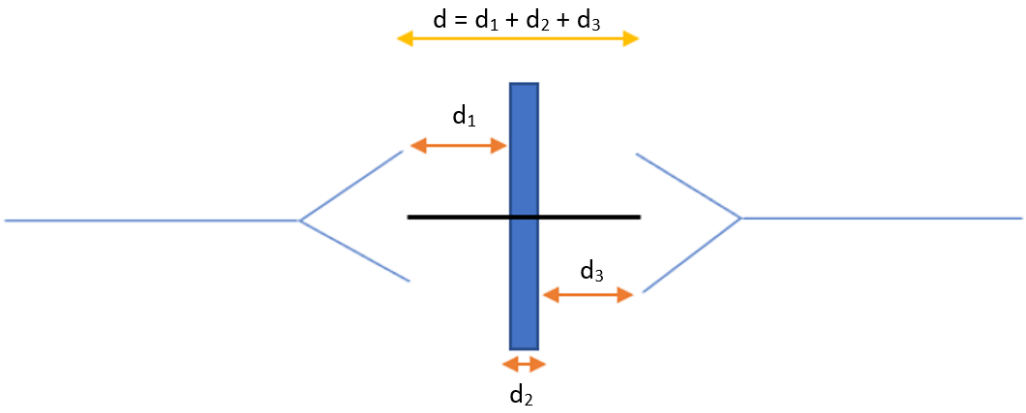

Figure B.2: Transmission set-up for permittivity measurement.

and, by subtracting the obstructed link phase with the unobstructed, it is possible to write expression B.6,

$$\Delta\phi = \phi_2 - \phi_1 = k_0(n-1)d_2 \tag{B.3}$$

and, given relation B.4

$$\epsilon_r = n^2 \tag{B.4}$$

and B.5

$$k_0 = \frac{2\pi}{\lambda} \tag{B.5}$$

it is possible to write equation B.4,

$$\epsilon_r = (1 + \frac{\lambda\Delta\phi}{2\pi d_2})^2 \tag{B.6}$$

with $\Delta\phi$ in radians. Measuring the phase difference in degrees, expression B.7 computes the permittivity.

$$\epsilon_r = (1 + \frac{\lambda\Delta\phi}{360 d_2})^2 \tag{B.7}$$

The set-up from figure B.2 was implemented, using two half-wavelength dipoles operating in the 8-12 GHz frequency band, in transmission mode. The S parameters were measured with the transmission link unobstructed and then with the skull model between them, as seen in figure B.3. Since the skull model thickness varies depending on where the measurement is performed, three positions were evaluated, with thickness 4.94 mm, 6.56 mm and 5.20 mm. The phase delay was measured at the S_{12} transmission maximum peak, at $f = 11.44$ GHz. Applying expression B.7 to the measured phase delays seen in figures B.4, B.5 and B.6, it is possible to compute the permittivities. The obtained values are $\epsilon_r = 2.8167$, 2.6312 and 2.8025. These values prove to be a good estimate of this PUR's permittivity, and are within the intervals present in [31].

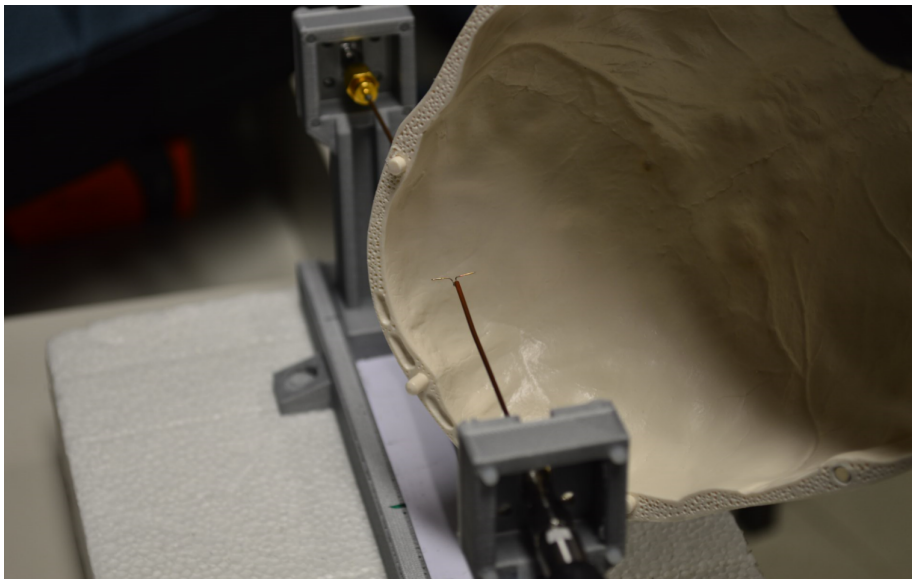

Figure B.3: PUR permittivity measurement, using two dipoles in transmission mode.

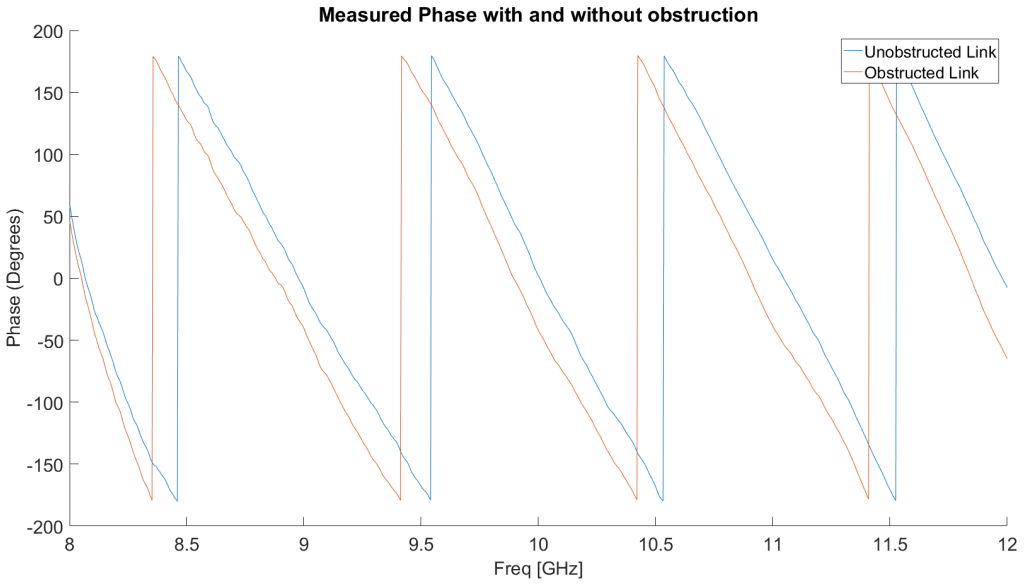

Figure B.4: Phase delay for skull model thickness of 4.94 mm.

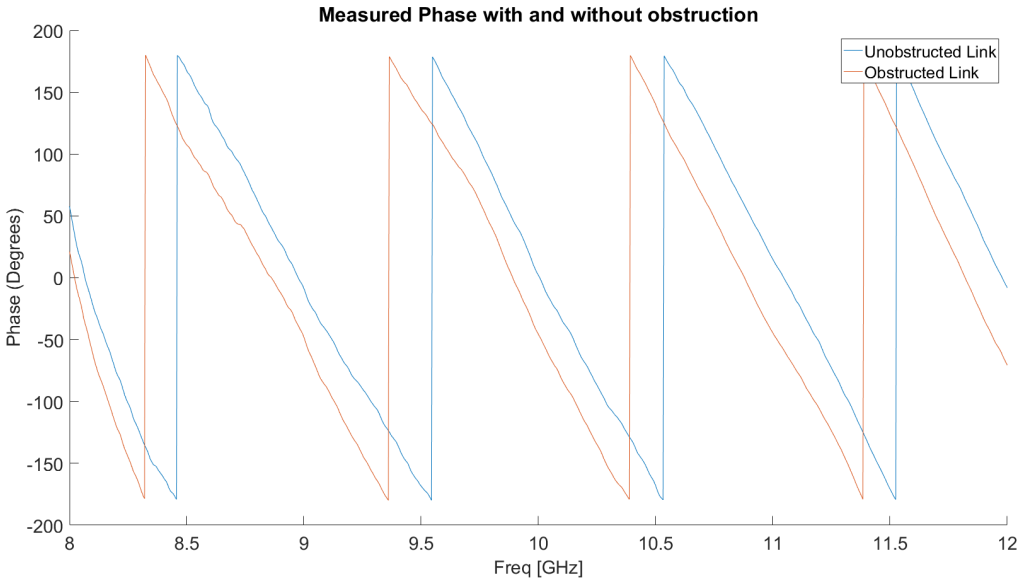

Figure B.5: Phase delay for skull model thickness of 6.56 mm.

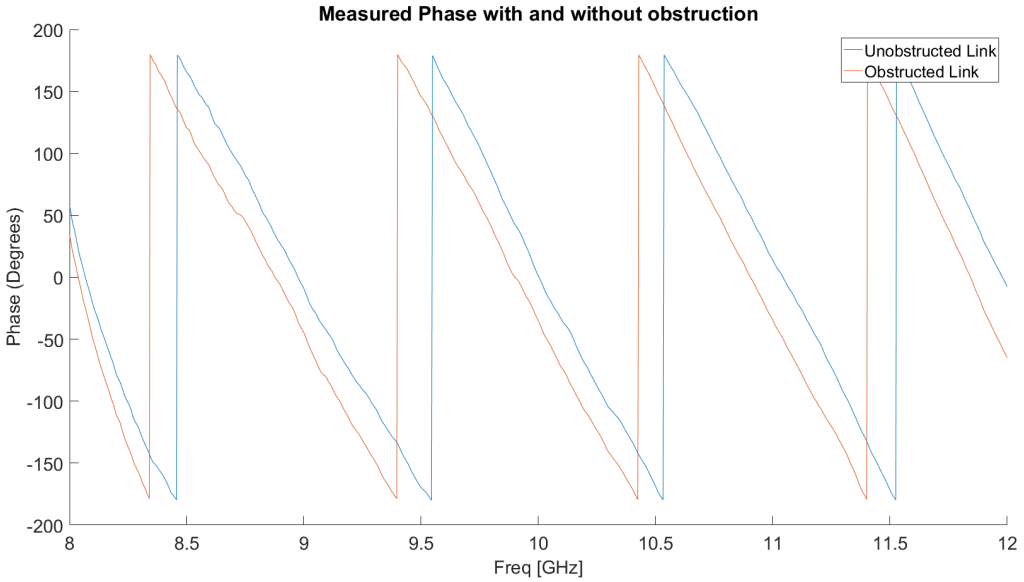

Figure B.6: Phase delay for skull model thickness of 5.20 mm.

Appendix C

Human Head Liquid Phantom Permittivity Measurement

In order to determine the liquid phantom permittivity, a different strategy was used when comparing to the one used in Appendix B. Based on the work of [33], the liquid phantom was prepared according to the guidelines in order to obtain a permittivity close to $\epsilon_r = 49$. In order to determine the actual permittivity of the phantom, since mistakes typically occur when measuring liquids using glass beakers, a small resonating cavity setup in transmission mode was used, as seen in figure C.1, and the S parameters were measured. Having the measured S parameters, a simulation model, designed in CST

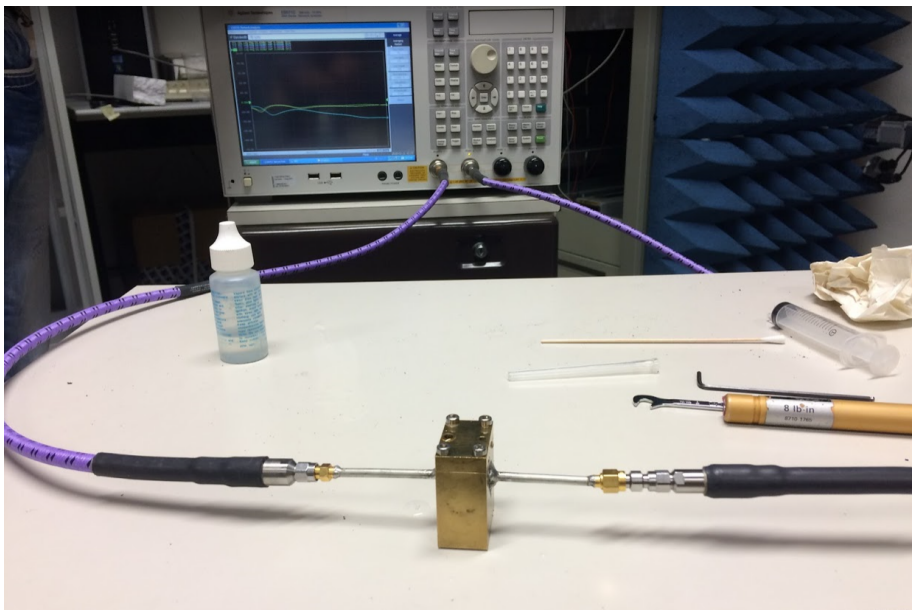

Figure C.1: Resonating cavity setup in transmission mode.

Studio Suite was used, as seen in figure C.2. By using the CST Studio Suite macro which allows the design of a Cole-Cole Material, given the high frequency permittivity, ϵ_∞, the static permittivity, ϵ_s, time constant, τ, relaxation constant, α and the desired frequency range. By filling the designed cavity with this material, the S parameters of this setup can be obtained. In order to obtain the liquid phantom

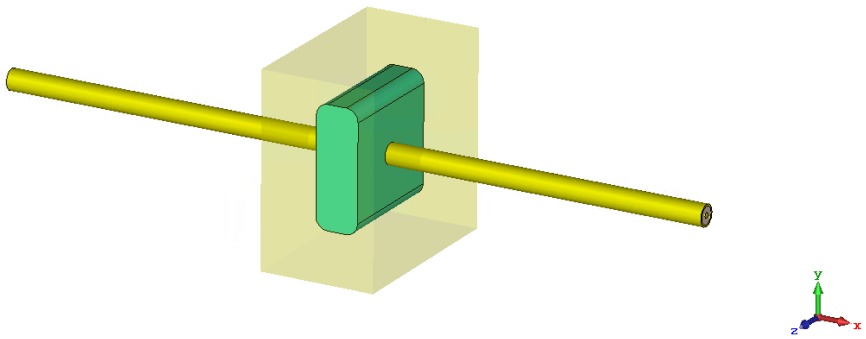

Figure C.2: Resonating cavity simulation model, as seen in CST Studio Suite.

Table C.1: Cole-Cole Material parameters defined in CST Studio Suite.

Cole-Cole Material Parameters	
ϵ_∞	15
ϵ_s	48
τ	20 ps
α	0

measured permittivity, a best-fit model is implemented, using Matlab. The unwrapped phase of the measured S_{12} parameter must accurately match the simulated one. The magnitude of the measured S_{12} parameter must follow the same behaviour as the simulated one. The S_{11} parameter unwrapped phase and magnitude must also follow the same behaviour as the simulated ones. However, its crucial that the measured S_{12} parameter unwrapped phase accurately matches the simulations. The designed Cole Material parameters are defined in Table C.1. The simulated and measured S parameters, using the designed Cole-Cole Material with the aforementioned values, are presented in figures C.3, C.4, C.5 and C.6. By accurately matching the S_{12} parameter unwrapped phase simulation and measurements, and obtaining the same behaviours for the S_{12} paramter magnitude, S_{11} parameter unwrapped phase and S_{11} parameter magnitude, the liquid phantom permittivity was obtained on CST Studio Suite, returning $\epsilon_r = 45.45$, for the designed PTVA central frequency of operation, $f = 2.3$ GHz as seen in figure C.7.

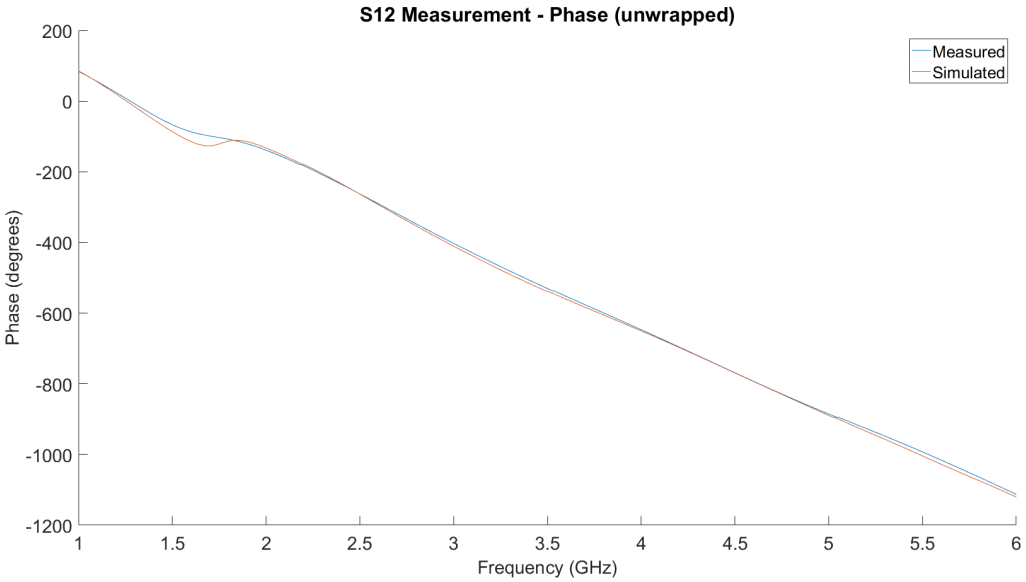

Figure C.3: Best-fit model for the S_{12} parameter unwrapped phase.

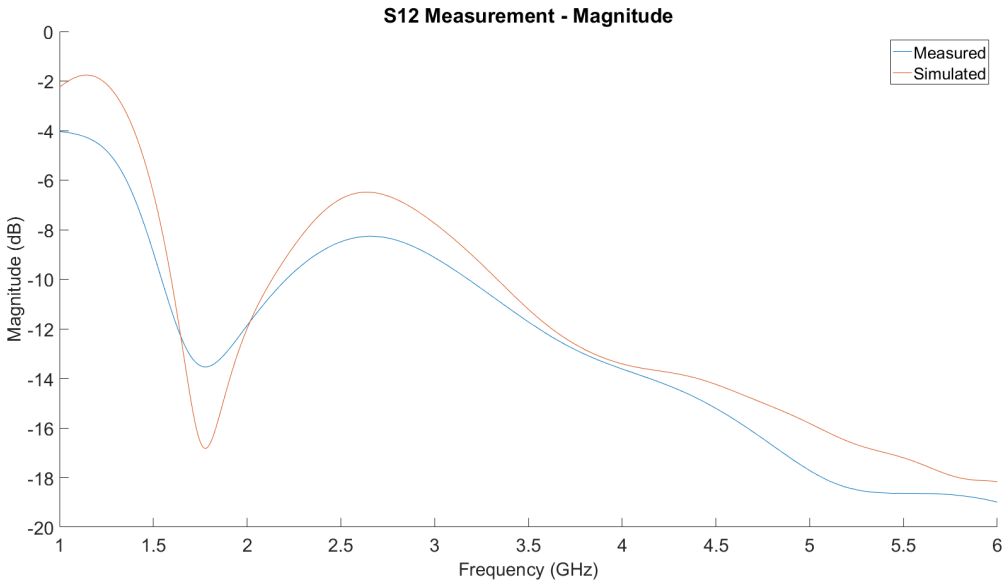

Figure C.4: Best-fit model for the S_{12} parameter magitude.

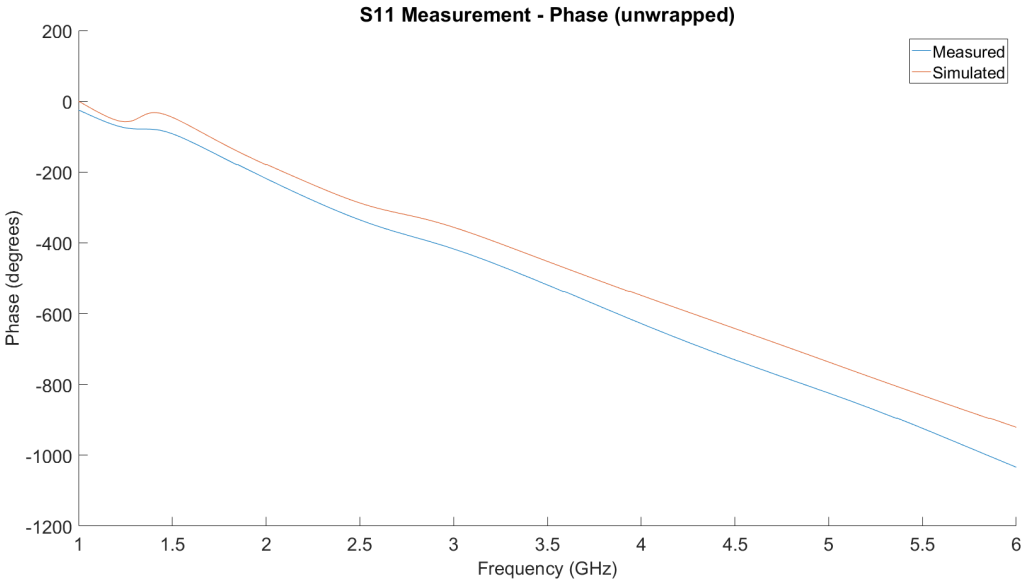

Figure C.5: Best-fit model for the S_{11} parameter unwrapped phase.

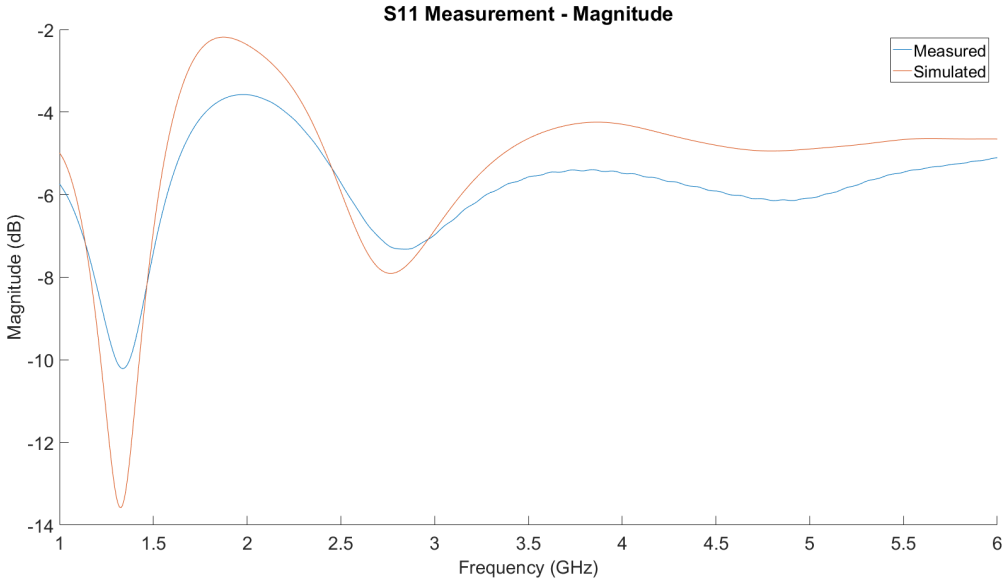

Figure C.6: Best-fit model for the S_{11} parameter magitude.

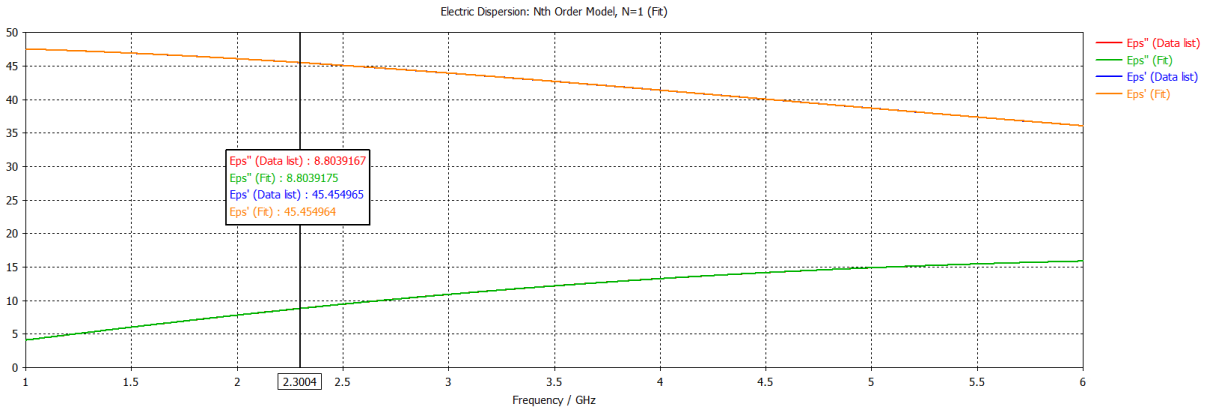

Figure C.7: Simulated permittivity for the designed Cole-Cole material.